

**No.: egosphere-2023-2913**

**Title: Measurement Report: Elevated excess-NH<sub>3</sub> can promote the redox reaction to produce HONO: Insights from the COVID-19 pandemic**

**Reviewer #1:**

**General Comments:**

In this study, the authors analyzed the chemical composition changes during the pandemic in ten urban and rural sites, and compared the HONO concentration level before and during the emission control period. The authors found that the HONO decline was relatively insignificant compared to its precursors and a detailed calculation shows that the enhanced production rate of aqueous phase reaction partially offset the effect of lower precursors. By comparing the atmospheric acids and bases concentrations, the authors suggested that the enhanced level of NH<sub>3</sub> and elevated aerosol pH due to less acidic components in the atmosphere was the reason for the higher HONO production rate. It can be one of the possible reasons, while there are several important issues that the authors did not have enough discussion or provide clear explanation. Some analysis and explanations are too simplified to give the assessment of the quality of this study.

Thank you for your careful reading of our paper and valuable comments and

suggestions. We believe that we have adequately addressed your comments. To facilitate your review, we used yellow highlights for your comments, green highlights for Reviewer #2, and red color indicating our own corrections in the manuscript.

**Major issues:**

1. The direct emission HONO was estimated based on the vehicle emission factors and NO<sub>x</sub> concentration level, which should reflect a general situation of normal human activities. However, during the pandemic, the emission factors could change very significantly if only necessary activities were allowed to be carried out. The authors did not mention emission profile change before and during the pandemic, which could lead to the overestimation of the effect of other pathways.

**Response:** Thanks for your comments. We determined whether it is necessary to calculate vehicle emissions, and a supplementary HONO emission factor table from vehicle emissions was added to support the selection of factors in the revised version:

“HONO can be released directly into the atmosphere through vehicle exhaust (Burling et al., 2010; Veres et al., 2010). The lifetime of HONO in the atmosphere is relatively short, so vehicle emissions significantly contribute to urban atmospheric HONO (Chen et al., 2023; Liu et al., 2021a). Considering that there has been a significant reduction in vehicle emissions in urban areas during DC. Additionally, the R-PY site is far from roads. Thus, vehicle emissions may not be the primary source of HONO for the U-ZK site during DC and R-PY sites during entire periods. To further

validate the above conclusions, the conditional bivariate probability function diagrams of NO<sub>2</sub> at U-ZK and R-PY sites during PC and DC are depicted in Figure S2. NO<sub>2</sub> predominantly originated from long-distance transport at the U-ZK site during DC and the R-PY site during both PC and DC. Consequently, vehicle emissions are only calculated for the U-ZK site during the PC.

Here we use the HONO/NO<sub>x</sub> ratio to estimate HONO concentration, which is generally considered to be the vehicle emission factor (Kramer et al., 2020; Hao et al., 2020; Yu et al., 2022) for HONO. The calculation formula is as follows:

$$[\text{HONO}_{\text{emi}}] = 0.8\% \times [\text{NO}_x] \quad (1)$$

where [HONO<sub>emi</sub>] and [NO<sub>x</sub>] represent the HONO concentration emitted by vehicles and the observed NO<sub>x</sub> concentration, respectively. Regarding previous studies (Table S3), 0.8% was selected as the vehicle emission factor, considering differences in vehicle type, fuel composition, and other factors (Kramer et al., 2020; Hao et al., 2020; Huang et al., 2017).”

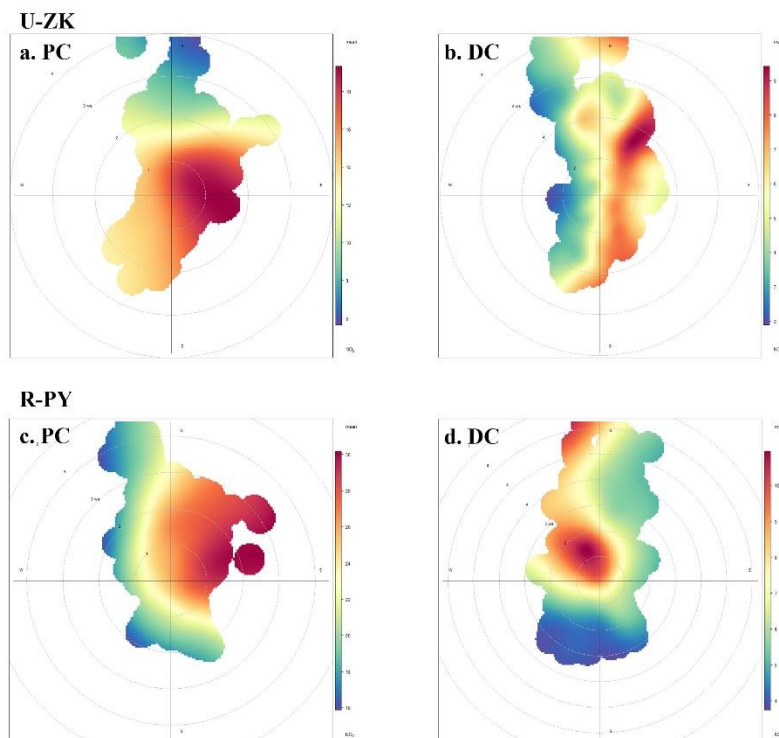


Figure S2. Result of conditional bivariate probability function plots: NO<sub>2</sub> at U-ZK and R-PY sites before (PC) and during (DC) the COVID-19 outbreak. The color scale bar represents NO<sub>2</sub> concentration.

Table S3. Summary of vehicle emission factors.

Observation site	Period	Emission factor (%)	Reference
Beijing	2020	0.79	(Meng et al., 2020)
Hong Kong	2015	0.4–1.8	(Yun et al., 2017)
Hong Kong	2011	0.5–1.6	(Xu et al., 2015)
Kiesberg Tunnel	2001	0.8	(Kleffmann et al., 2003)
Kiesberg Tunnel	1997	0.3–0.8	(Kurtenbach and Wiesen, 2001)
Guangzhou	2019	1.31	(Li et al., 2021b)

2. Supplement Line 107: it is very challenging to pick a representative OH concentration to represent the general situation. The authors also suggested in the

introduction that OH radical concentration could change during emission control as part of atmospheric oxidizing capacity changes. While the authors did not mention such an approach in their HONO production calculation. In addition to other reaction pathways, another possibility is the change of reaction rates, like OH concentration levels and higher temperature (the authors only mentioned H and K temperature dependence but did not mention  $k_1$  temperature dependence, which could be important). The authors should fully discuss the possibilities of the changes in reaction rate and possible sinks.

**Response:** Thank you for your valuable comments.

Firstly, we have modified the method for determining •OH concentration in the revised manuscript:

“•OH concentration was simulated according to the empirical model (Hu et al., 2022; Wang et al., 2025):

$$[\text{OH}] = 4.1 \times 10^9 \times \frac{J(\text{O}^1\text{D}) \times J(\text{NO}_2) \times (140 \times [\text{NO}_2] + 1) + [\text{HONO}] \times J(\text{HONO})}{0.41 \times [\text{NO}_2]^2 + 1.7 \times [\text{NO}_2] + 1 + [\text{NO}] \times k_{\text{NO}+\text{OH}} + [\text{HONO}] \times k_{\text{NO}+\text{OH}}} \quad (12)$$

where,  $J(\text{O}^1\text{D})$ ,  $J(\text{NO}_2)$ , and  $J(\text{HONO})$  are the photolysis rates calculated using the TUV model (v5.2; available at <http://cprm.acom.ucar.edu/Models/TUV/>). The calculated •OH concentration varied from  $0.1 \times 10^6$  to  $4 \times 10^6$  molecule/cm<sup>3</sup> at U-ZK and  $0.1 \times 10^6$  to  $5 \times 10^6$  molecule/cm<sup>3</sup> at R-PY, which was comparable to the levels in other cities of North China (Li et al., 2018; Fuchs et al., 2017; Yang et al., 2017). Since there is no photolysis at night, the •OH concentration was assumed to be  $0.8 \times 10^6$  molecule/cm<sup>3</sup> (Wang et al., 2022).”

Secondly, the sources of HONO were recalculated to better investigate the changes

in HONO between PC and DC periods:

## Text S4 Sources of HONO

### 4.1 Direct emission

HONO can be released directly into the atmosphere through vehicle exhaust (Burling et al., 2010; Veres et al., 2010). The lifetime of HONO in the atmosphere is relatively short, so vehicle emissions significantly contribute to urban atmospheric HONO (Chen et al., 2023; Liu et al., 2021a). Considering that there has been a significant reduction in vehicle emissions in urban areas during DC. Additionally, the R-PY site is far from roads. Thus, vehicle emissions may not be the primary source of HONO for the U-ZK site during DC and R-PY sites during entire periods. To further validate the above conclusions, the conditional bivariate probability function diagrams of NO<sub>2</sub> at U-ZK and R-PY sites during PC and DC are depicted in Figure S2. NO<sub>2</sub> predominantly originated from long-distance transport at the U-ZK site during DC and the R-PY site during both PC and DC. Consequently, vehicle emissions are only calculated for the U-ZK site during the PC.

Here we use the HONO/NO<sub>x</sub> ratio to estimate HONO concentration, which is generally considered to be the vehicle emission factor (Kramer et al., 2020; Hao et al., 2020; Yu et al., 2022) for HONO. The calculation formula is as follows:

$$[\text{HONO}_{\text{emi}}] = 0.8\% \times [\text{NO}_x] \quad (1)$$

where [HONO<sub>emi</sub>] and [NO<sub>x</sub>] represent the HONO concentration emitted by vehicles

and the observed  $\text{NO}_x$  concentration, respectively. Regarding previous studies (Table S3), 0.8% was selected as the vehicle emission factor, considering differences in vehicle type, fuel composition, and other factors (Kramer et al., 2020; Hao et al., 2020; Huang et al., 2017).

#### 4.2 Homogeneous reaction of NO and $\bullet\text{OH}$

The reaction between NO and  $\bullet\text{OH}$  is the primary gas-phase reaction source of HONO at high NO concentrations, and the production rate contribution ( $P_{\text{OH}+\text{NO}}$ ) for this reaction can be calculated as:

$$P_{\text{OH}+\text{NO}} = k_{\text{OH}+\text{NO}}[\text{OH}][\text{NO}] \quad (2)$$

where  $k_{\text{OH}+\text{NO}}$  ( $7.2 \times 10^{-12} \text{ cm}^3 \text{ molecule}^{-1} \text{ s}^{-1}$ ) is the rate constant for the reactions at 298K (Li et al., 2012).  $\bullet\text{OH}$  concentration was simulated according to the empirical model (Hu et al., 2022; Wang et al., 2025):

$$[\text{OH}] = 4.1 \times 10^9 \times \frac{J(\text{O}^1\text{D}) \times J(\text{NO}_2) \times (140 \times [\text{NO}_2] + 1) + [\text{HONO}] \times J(\text{HONO})}{0.41 \times [\text{NO}_2]^2 + 1.7 \times [\text{NO}_2] + 1 + [\text{NO}] \times k_{\text{NO}+\text{OH}} + [\text{HONO}] \times k_{\text{NO}+\text{OH}}} \quad (3)$$

where,  $J(\text{O}^1\text{D})$ ,  $J(\text{NO}_2)$ , and  $J(\text{HONO})$  are the photolysis rates calculated using the TUV model (v5.2; available at <http://cprm.acom.ucar.edu/Models/TUV/>). The cloud optical depth value for the TUV model was adjusted so that the predicted UVB radiation intensity matched the observations (Lyu et al., 2019; Wang et al., 2022b). The calculated  $\bullet\text{OH}$  concentration varied from  $0.1 \times 10^6$  to  $4 \times 10^6 \text{ molecule/cm}^3$  at U-ZK and  $0.1 \times 10^6$  to  $5 \times 10^6 \text{ molecule/cm}^3$  at R-PY, which was comparable to the levels in other cities of North China (Li et al., 2018; Fuchs et al., 2017; Yang et al., 2017). Since there is no

photolysis at night, the  $\bullet\text{OH}$  concentration was assumed to be  $0.8 \times 10^6$  molecule/cm<sup>3</sup> (Wang et al., 2022).

### 4.3 Heterogeneous conversion of NO<sub>2</sub> to HONO

#### 4.3.1 Heterogeneous dark reactions

The heterogeneous conversion of NO<sub>2</sub> to HONO on the ground ( $P_{\text{ground}}$ ) and on the aerosol surface ( $P_{\text{aerosol}}$ ) was calculated based on parameters obtained from experiments or observations.

$$P_{\text{ground}} = \frac{1}{8} \gamma_1 \times [\text{NO}_2] \times C_{\text{NO}_2} \times \frac{S_g}{V} \quad (4)$$

$$P_{\text{aerosol}} = \frac{1}{4} \gamma_2 \times [\text{NO}_2] \times C_{\text{NO}_2} \times \frac{S_a}{V} \quad (5)$$

$$\frac{S_g}{V} = \frac{1}{\text{MLH}} \quad (6)$$

$$C_{\text{NO}_2} = \sqrt{\frac{8RT}{\pi M}} \quad (7)$$

where  $C_{\text{NO}_2}$  is the average molecular velocity of NO<sub>2</sub> molecule (m s<sup>-1</sup>); R is the ideal gas constant; T is the temperature (K); M is the molecular weight of NO<sub>2</sub> (kg mol<sup>-1</sup>); MLH is the height of the mixed layer, which is determined to be 50 m due to HONO formation on the ground level and its short lifetime (Liu et al., 2020b);  $S_a/V$  is the surface area to volume ratio of aerosol, estimated by Su et al. (Su et al., 2008).

#### 4.3.2 Heterogeneous photo-enhanced reactions

The heterogeneous photo-enhanced reactions of NO<sub>2</sub> on the surface of the ground



( $P_{\text{ground+hv}}$ ) and the surface of the aerosol ( $P_{\text{aerosol+hv}}$ ) were calculated following (Zhang et al., 2020a):

$$P_{\text{ground+hv}} = \frac{1}{8} \times C_{\text{NO}_2} \times \frac{1}{\text{MLH}} \times \gamma_1 \times \frac{J_{\text{NO}_2}}{J_{\text{NO}_2,\text{noon}}} \times [\text{NO}_2] \quad (8)$$

$$P_{\text{aerosol+hv}} = \frac{1}{4} \times C_{\text{NO}_2} \times \frac{S_a}{V} \times \gamma_2 \times \frac{J_{\text{NO}_2}}{J_{\text{NO}_2,\text{noon}}} \times [\text{NO}_2] \quad (9)$$

where  $J_{\text{NO}_2}$  and  $J_{\text{NO}_2,\text{noon}}$  are the photolysis rate of  $\text{NO}_2$  and the photolysis rate of  $\text{NO}_2$  at noon during the day, respectively.

$\gamma_1$  and  $\gamma_2$  are the absorption coefficient of  $\text{NO}_2$  on the ground and aerosol surface, respectively, which is assumed to be  $4 \times 10^{-6}$  (Yu et al., 2022; Zhang et al., 2021; Zhang et al., 2020a). Moreover, we discuss the uncertainties based on the recommended values of  $2 \times 10^{-6}$ – $1 \times 10^{-5}$  as upper and lower bounds (Chen et al., 2023; VandenBoer et al., 2013; Wong et al., 2011). Results show (Figure S3) that the uncertainties for  $P_{\text{ground}}$ ,  $P_{\text{aerosol}}$ ,  $P_{\text{ground+hv}}$ , and  $P_{\text{aerosol+hv}}$  are  $-50\%$  to  $150\%$ ,  $-50\%$  to  $151\%$ ,  $-20\%$  to  $120\%$ , and  $-50\%$  to  $121\%$  at the U-ZK, respectively. At the R-PY, the uncertainties for  $P_{\text{ground}}$ ,  $P_{\text{aerosol}}$ ,  $P_{\text{ground+hv}}$ , and  $P_{\text{aerosol+hv}}$  are  $-50\%$  to  $150\%$ ,  $-50\%$  to  $151\%$ ,  $-20\%$  to  $120\%$ , and  $-50\%$  to  $121\%$ , respectively.

#### 4.4 Nitrate photolysis

The nitrate photolysis ( $P_{\text{nitrate}}$ ) was calculated based on the measured nitrate concentration ( $\text{NO}_3^-$ ) from  $\text{PM}_{2.5}$  and nitrate photolysis rate ( $J_{\text{nitrate} \rightarrow \text{HONO}}$ ):

$$P_{\text{nitrate}} = J_{\text{nitrate} \rightarrow \text{HONO}} \times [\text{NO}_3^-] \quad (10)$$

where the  $J_{\text{nitrate} \rightarrow \text{HONO}}$  was simulated by normalizing UV values, when the Zenit Angle is  $0^\circ$ ,  $J_{\text{nitrate} \rightarrow \text{HONO}}$  varied within the range of  $1.22 \times 10^{-5}$  to  $4.84 \times 10^{-4} \text{ s}^{-1}$ , with an average value of  $8.24 \times 10^{-5} \text{ s}^{-1}$  (Bao et al., 2018).”

Unfortunately, for MLH,  $S_a/V$ , and the relationship between  $k_1$  and temperature, as there were no observational data or scientifically established estimation methods, this study did not consider their variations. This omission may lead to differences in conclusions and warrants further investigation in future research.

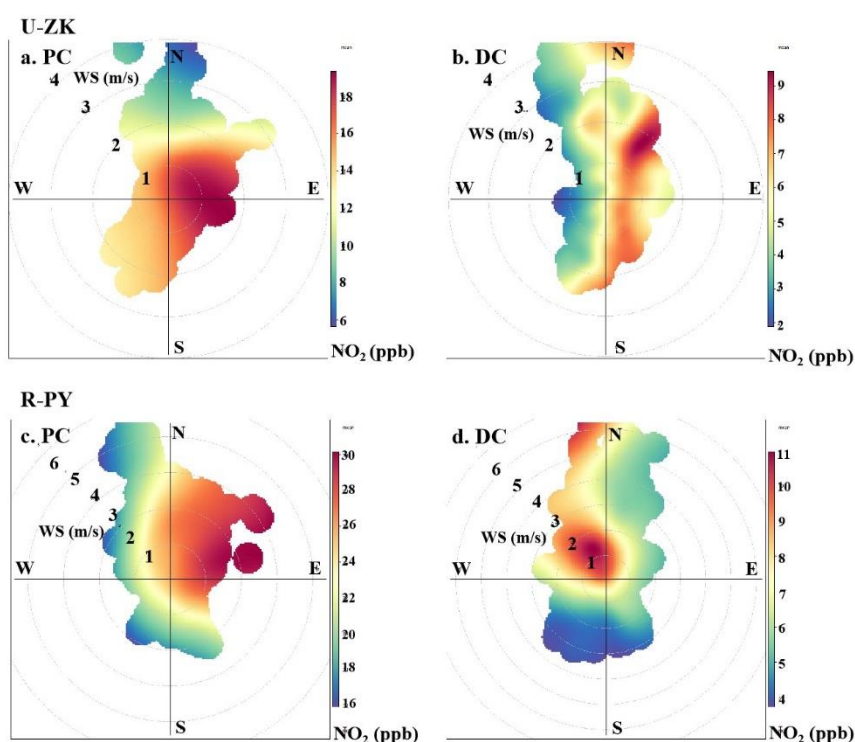


Figure S2. Result of conditional bivariate probability function plots:  $\text{NO}_2$  at U-ZK and R-PY sites before (PC) and during (DC) the COVID-19 outbreak. The color scale bar represents  $\text{NO}_2$  concentration.

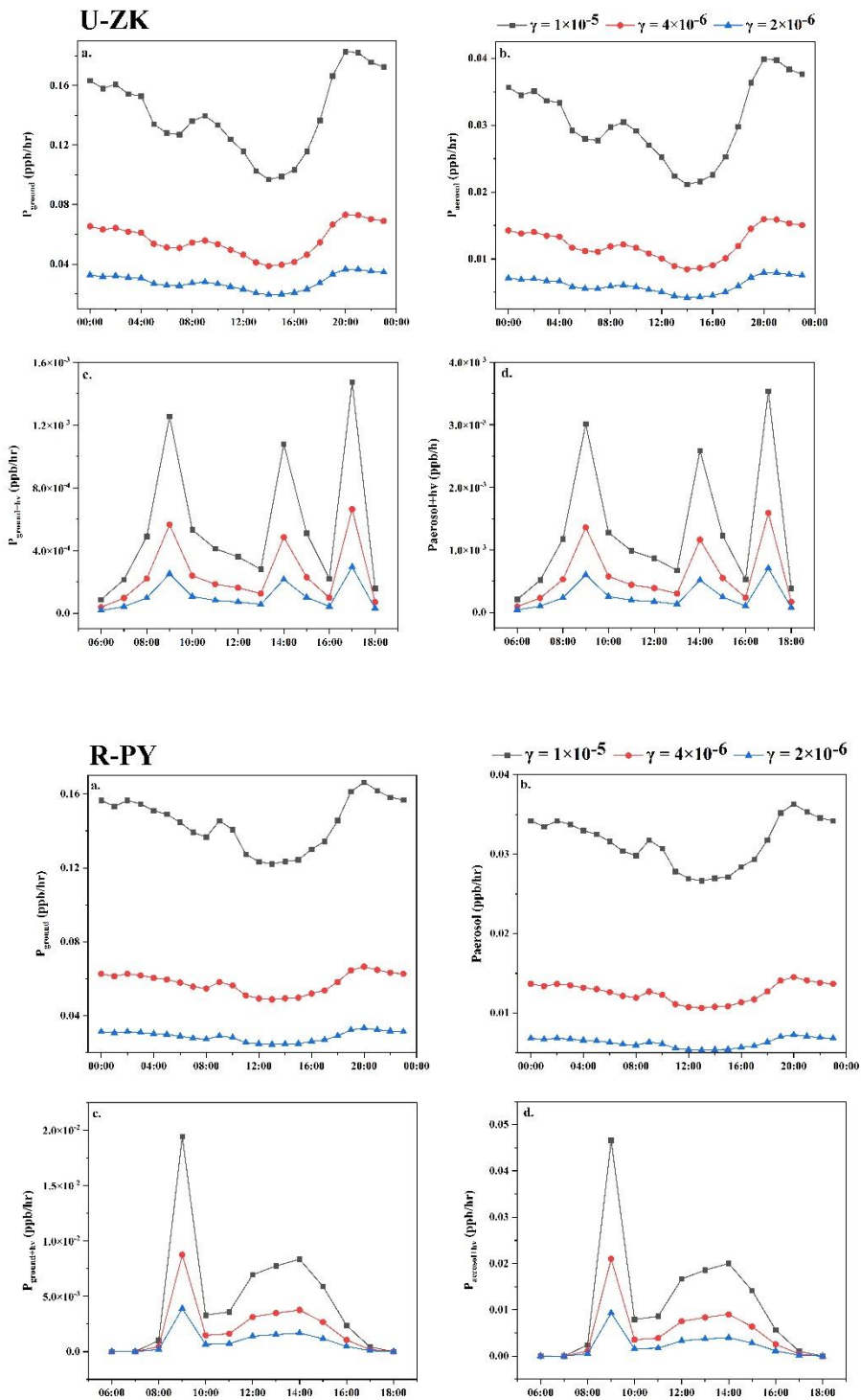


Figure S3. HONO production rate using different uptake rates of  $\text{NO}_2$  at the U-ZK and R-PY sites before (PC) and during (DC) the COVID-19 outbreak. (a)  $P_{\text{ground}}$ , (b)  $P_{\text{aerosol}}$ , (c)  $P_{\text{ground+hv}}$ , and (d)  $P_{\text{aerosol+hv}}$

Table S3. Summary of vehicle emission factors.

Observation site	Period	Emission factor (%)	Reference
Beijing	2020	0.79	(Meng et al., 2020)
Hong Kong	2015	0.4–1.8	(Yun et al., 2017)
Hong Kong	2011	0.5–1.6	(Xu et al., 2015)
Kiesberg Tunnel	2001	0.8	(Kleffmann et al., 2003)
Kiesberg Tunnel	1997	0.3–0.8	(Kurtenbach and Wiesen, 2001)
Guangzhou	2019	1.31	(Li et al., 2021b)

3. It is also questionable about the contribution of NH<sub>3</sub> concentration changes to the total pH changes. Temperature, relative humidity, and other salts could also contribute to pH changes. It was not mentioned how the sensitivity tests of Line 264-275 were done and the interpretation of the results was also unclear. The authors did not give a complete pH comparison like NH<sub>x</sub> levels, only provided two sites in Figure 4. The authors mentioned the increase of pH 0.4 and 0.1 for U-ZK and R-PY sites respectively. However, based on the NH<sub>3</sub> levels shown in Table 1 and the relationship mentioned in Song et al. (2019):  $\partial\text{pH}/\partial[\text{NH}_3(\text{g})] \approx 0.4/[\text{NH}_3(\text{g})]$ , the NH<sub>3</sub> concentration changes was only responsible for 0.13-unit pH change in U-ZK (less than half). The pH changes of most sites, if only considering NH<sub>3</sub> levels changes in Table 1, can be calculated to be around 0.1 with the exception of R-SQ where NH<sub>3</sub> concentration nearly doubled.

**Response:** Sorry for the misunderstanding. The formula in Song's study only considers the effect of NH<sub>3</sub> on the pH value of particulate matter and does not take into account other substances such as TH<sub>2</sub>SO<sub>4</sub>, TNO<sub>3</sub>, T, etc., which have a greater impact on pH value. Therefore, when the NH<sub>3</sub> value in this study is brought into the formula, there is

a different conclusion obtained. To explore the dominant factors that determine the high pH during the DC, we have added a detailed description of the sensitivity tests of pH to input data:

“To explore the dominant factors that determine the local particle pH level and result in the high pH during the DC, sensitivity tests of pH to chemical species (i.e.,  $\text{TNH}_x$ ,  $\text{TH}_2\text{SO}_4$ ,  $\text{TNO}_3$ ,  $\text{TCl}$ ,  $\text{TNa}$ ,  $\text{K}^+$ ,  $\text{Ca}^{2+}$ , and  $\text{Mg}^{2+}$ ) and meteorological parameters (i.e.,  $T$  and  $\text{RH}$ ) were performed. A given range for a variable (i.e.,  $\text{TNH}_x$ ) with corresponding average values of other parameters (i.e.,  $\text{TH}_2\text{SO}_4$ ,  $\text{TNO}_3$ ,  $\text{TCl}$ ,  $\text{TNa}$ ,  $\text{K}^+$ ,  $\text{Ca}^{2+}$ ,  $\text{Mg}^{2+}$ ,  $T$ , and  $\text{RH}$ ) was input into the model and simulated to compare its effects on pH. As shown in Fig. S7, pH increases with the cation concentrations (i.e.,  $\text{TNH}_x$ ,  $\text{Na}^+$ ,  $\text{K}^+$ ,  $\text{Ca}^{2+}$ , and  $\text{Mg}^{2+}$ ) increasing as well as the anion concentrations (i.e.,  $\text{TH}_2\text{SO}_4$ ,  $\text{TNO}_3$ , and  $\text{Cl}^-$ ),  $T$  and  $\text{RH}$  decreasing. According to the average values of input data during PC (Blue line in Fig. S7) and DC (Red line in Fig. S7) at U-ZK and R-PY sites respectively, the changes in pH ( $\Delta\text{pH}$  in Fig. 5) indicate that the decrease in  $\text{TNH}_x$  concentration and the increase in  $T$  in DC led to a decrease in pH values ( $\Delta\text{pH}$ : 0.09 at U-ZK and 0.08 at R-PY sites) compared to PC. However, this effect was outweighed by the decrease in  $\text{TH}_2\text{SO}_4$  ( $\Delta\text{pH}$ : 0.07 and 0.8 at U-ZK and R-PY sites, respectively) and  $\text{TNO}_3$  ( $\Delta\text{pH}$ : 0.05 and 0.4 at U-ZK and R-PY sites, respectively) concentrations as well as the increase in  $\text{K}^+$  ( $\Delta\text{pH}$ :

0.03 at U-ZK and 0.2 at R-PY site) and  $Mg^{2+}$  ( $\Delta pH$ : 0.01 at U-ZK and 0.04 at R-PY site) concentrations in the DC, and resulting in an overall increase in pH values in the DC. Furthermore, the relationship between particle pH with the concentrations of Required- $NH_x$ , and Excess- $NH_x$ , which considers all chemical components, is investigated to examine the dominant factor on the increasing pH in DC. As shown in Fig. 6, the higher Excess- $NH_x$  concentrations in the DC led to higher increases in pH values ( $\Delta pH$ : 1 at U-ZK and 0.5 at R-PY site) than those in PC ( $\Delta pH$ : 0.3 at U-ZK and 0.2 at R-PY site), thus Excess- $NH_x$  concentrations may be the key factor in promoting the pH values.”

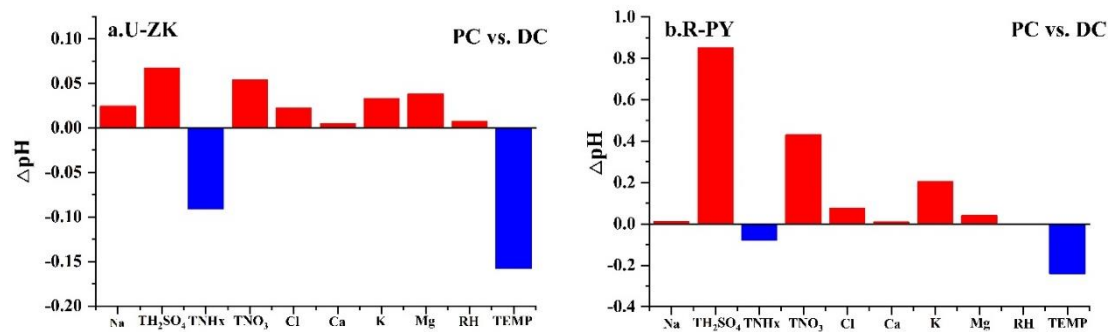


Figure 5. Changes of pH ( $\Delta pH$ ) through the sensitivity tests (Figure S5 and S6) by changing parameters between PC and DC at the a. U-ZK and b. R-PY sites.

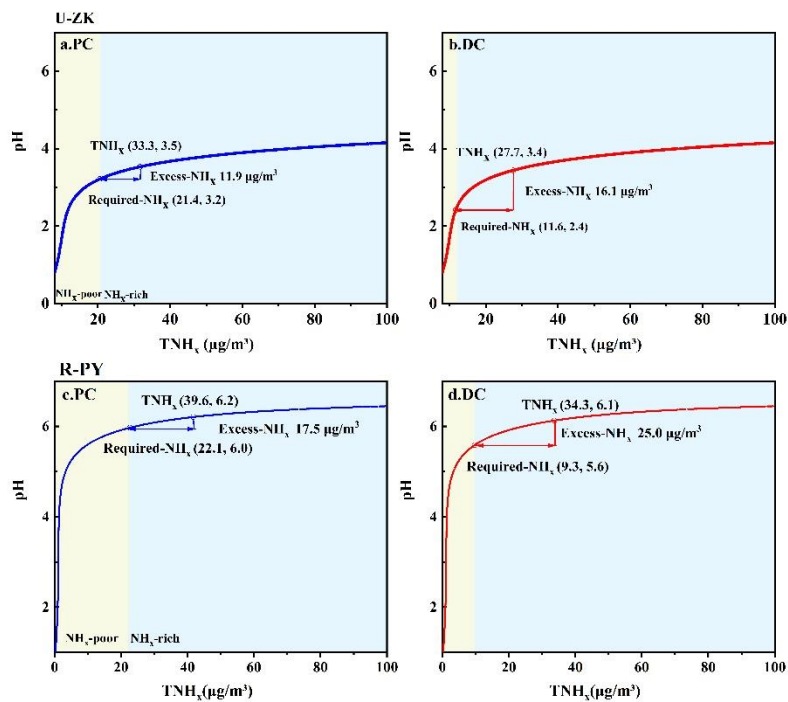


Figure 6. Particle pH corresponds to increasing TNH<sub>x</sub> at U-ZK and R-PY sites to examine the effects of major indicators of NH<sub>3</sub> (i.e., TNH<sub>x</sub>, Required-NH<sub>x</sub>, and Excess-NH<sub>x</sub>) on aerosol acidity. Particle pH was calculated by using a wide range of TNH<sub>x</sub> (25–130 μg/m<sup>3</sup>) and average values of other parameters in PC and DC of U-ZK and R-PY sites. The concentrations of TNH<sub>x</sub>, Required-NH<sub>x</sub>, and Excess-NH<sub>x</sub> with corresponding pH values are marked by a hollow box, hollow circle, and arrow respectively. The yellow and blue background colors correspond to the NH<sub>x</sub>-poor and NH<sub>x</sub>-rich, respectively.

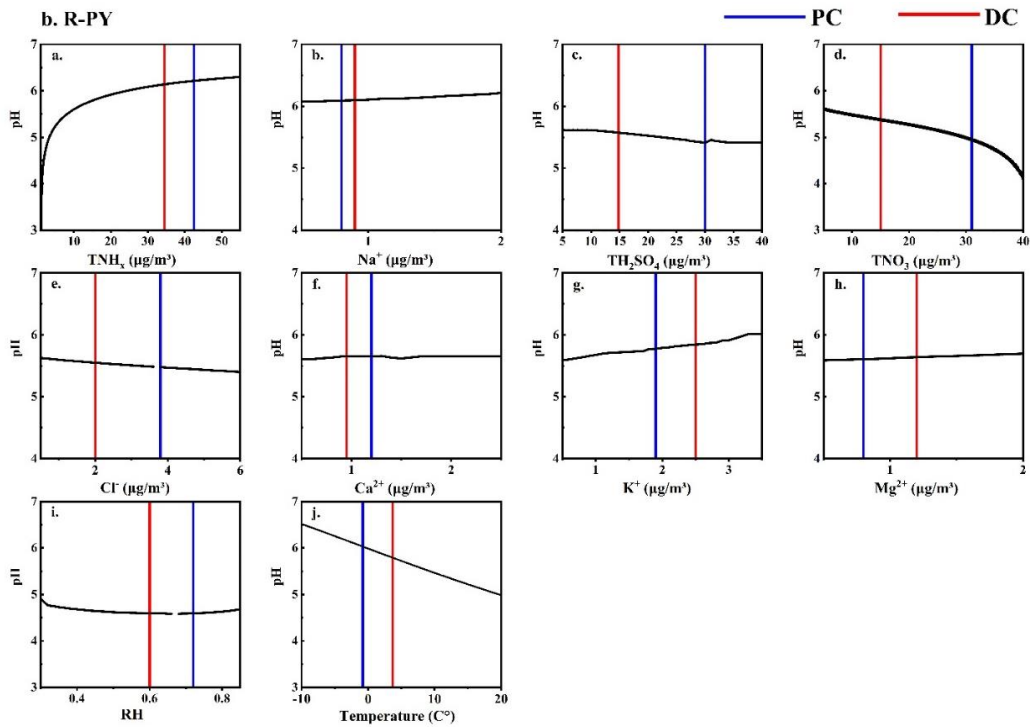
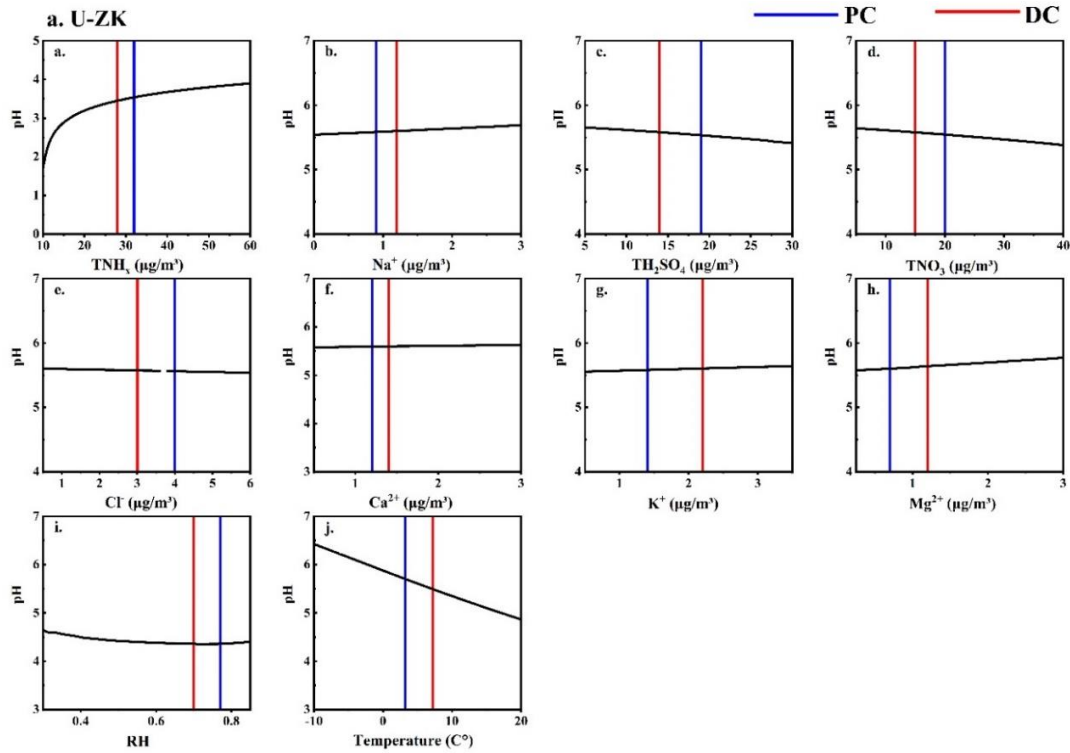
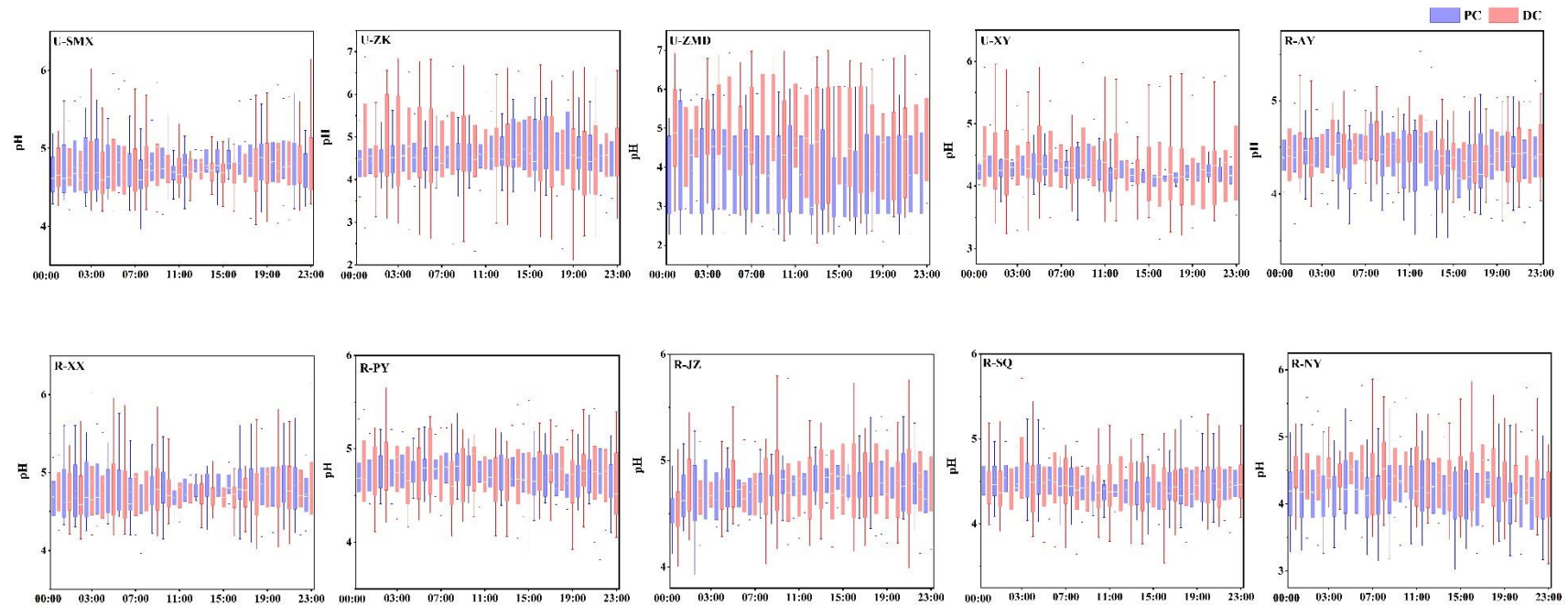


Figure S7. Sensitivity tests of pH to each factor. The vertical bar represents the mean values before (PC) and during (DC) the COVID-19 outbreak. A given range for a variable (i.e.,  $\text{TNH}_x$ ) with corresponding average values of other parameters (i.e.,  $\text{TH}_2\text{SO}_4$ ,  $\text{TNO}_3$ ,  $\text{TCl}$ ,  $\text{TNa}$ ,  $\text{K}^+$ ,  $\text{Ca}^{2+}$ ,  $\text{Mg}^{2+}$ ,  $\text{T}$ , and  $\text{RH}$ ) was simulated to compare its effects on pH.



Additionally, we have added a complete pH comparison of ten sites:

“Diurnal patterns of particle pH in PC and DC at ten sites are summarized in Fig. 4 with their average values listed in Table S9.  $PM_{2.5}$  shows consistent moderate acidity, with mean values in the range of 4.2–5.1, which were close to the values in previous studies (Table S9). Compared to the PC, the particle pH at ten sites increased obviously in the DC, with the highest increase of 0.5 (U-ZK) and 0.3 (R-PY) at urban and rural sites, respectively, which were the subject of in-depth discussion in the following text.”



1

2 Figure 4. Diurnal patterns of pH at ten sites before (PC) and during (DC) the COVID-19 outbreak. In each box, the top, middle, and bottom

3 lines represent the 75, 50, and 25 percentiles of statistical data, respectively; the upper and lower whiskers represent the 90 and 10 percentiles of

4 statistical data, respectively

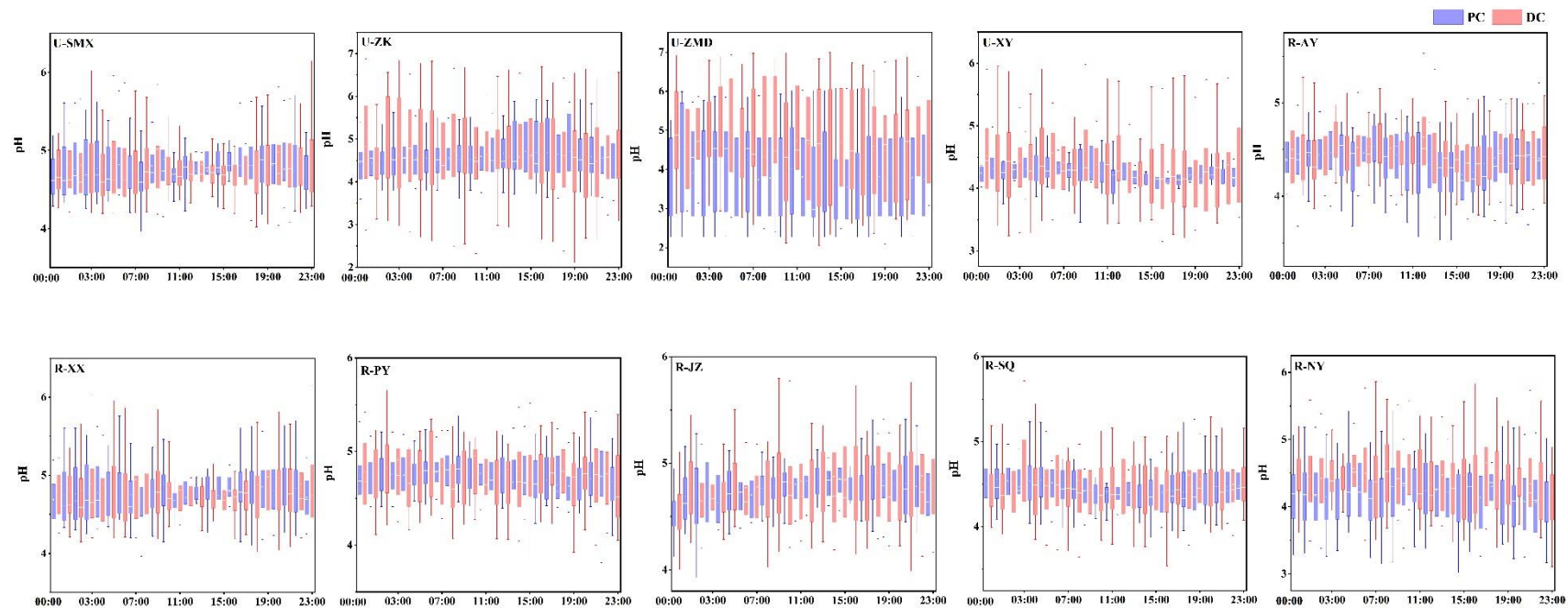
Table S9. Comparison of the particle pH values in this study (PC/DC) and other sites (mean or mean  $\pm$  standard).

	Sites	Periods	pH	References
Urban	Sanmenxia	Jan–Feb 2020	4.6 $\pm$ 0.5/4.8 $\pm$ 0.9	This study
	Zhoukou	Jan–Feb 2020	4.6 $\pm$ 0.6/5.1 $\pm$ 0.4	
	Zhumadian	Jan–Feb 2020	4.6 $\pm$ 0.3/4.8 $\pm$ 1.2	
	Xinyang	Jan–Feb 2020	4.2 $\pm$ 0.3/4.6 $\pm$ 1.3	
Rural	Anyang	Jan–Feb 2020	4.5 $\pm$ 0.4/4.6 $\pm$ 0.8	
	Xinxiang	Jan–Feb 2020	4.8 $\pm$ 0.5/4.9 $\pm$ 0.9	
	Puyang	Jan–Feb 2020	4.8 $\pm$ 0.3/5.1 $\pm$ 0.9	
	Jiaozuo	Jan–Feb 2020	4.9 $\pm$ 0.5/5.1 $\pm$ 0.8	
	Shangqiu	Jan–Feb 2020	4.5 $\pm$ 0.3/4.7 $\pm$ 0.8	
	Nanyang	Jan–Feb 2020	4.2 $\pm$ 0.5/4.4 $\pm$ 0.7	
Urban	Beijing	Jan–Feb 2015	4.5	
	Beijing	Dec 2016	4.3 $\pm$ 0.4	(Liu et al., 2017)
	Beijing	Feb 2017	4.5 $\pm$ 0.7	(Ding et al., 2019)
	Tianjin	Dec–Jun 2015	4.9 $\pm$ 1.4	(Shi et al., 2017)
	Tianjin	Aug 2015	3.4 $\pm$ 0.5	(Shi et al., 2019)
	Hohhot	Winter	5.7	(Wang et al., 2019)
	Mt. Tai	Summer	2.9 $\pm$ 0.5	(Liu et al., 2021b)
	Taoyuan	Nov 2017–Jan 2018	5.1 $\pm$ 1.0	(Duan et al., 2021)
	Zhengzhou	Jan 2018	4.5	(Wang et al., 2020)
	Anyang	Jan 2018	4.8	(Wang et al., 2020)
Mountain	Mt. Tai	Summer	3.6 $\pm$ 0.7	(Liu et al., 2021b)
Rural	Shanglan	Nov 2017–Jan 2018	5.5 $\pm$ 1.1	(Duan et al., 2021)

4. Figure 4, the maximum and minimum values provided little information of the whole pH variations. A box and whisker plot are more useful to identify the general trends and variations. And there were frequent situations of maximum pH higher than 7, which could not be explained by higher NH<sub>3</sub> concentrations. Instead, it could be from the strong influence of dust components. If that situation happened frequently enough (hard to judge now based on the information given), it could be the dust components that are actually responsible for the high pH.

**Response:** Thank you for your suggestions. We redrew Figure 4 as a box diagram and replaced

it in the revised version. After examining the raw data, we found that the pH data higher than 7 mainly concentrated in clean air with low pollutant concentrations. Additionally, some data had RH levels below 30%, which could lead to significant errors in the model. Thus, ISORROPIA-II was rerun only using data with  $RH \geq 30\%$  in the revised version.



1

2 Figure 4. Diurnal patterns of pH at ten sites before (PC) and during (DC) the COVID-19 outbreak. In each box, the top, middle, and bottom  
 3 lines represent the 75, 50, and 25 percentiles of statistical data, respectively; the upper and lower whiskers represent the 90 and 10 percentiles of  
 4 statistical data, respectively.

5. It should also be mentioned that the approach of the authors used to estimate  $AWC_{org}$  is sensitive to the parameters chosen, such as OM/OC ratio, density, and kappa parameter. Normally, the term  $AWC_{org}$  is small enough so that its influence is limited, while it is possible the uncertainty associated with the parameters chosen became big enough when inorganic salts become depleted and the relative contribution of OM got enhanced.

**Response:** Thank you for your comment. We supplemented the selection criteria for calculating parameters in the revised manuscript:

“ $AWC_{org}$  is the particle water associated with the organic matters predicted using the following method:

$$AWC_{org} = \frac{m_s}{\rho_s} \frac{k_{org}}{\left(\frac{1}{RH} - 1\right)} \quad (2.2)$$

where  $m_s$  is the mass concentration of organic matter ( $OM = OC \times f$ ). The  $f$  is the conversion factor of OC, which is dependent on the extent of OM oxidation and secondary organic aerosol formation (Chow et al., 2015). Studies on the ratio of OM/OC in fourteen cities in China suggested that the mean value of  $f$  was  $1.59 \pm 0.18$  during the winter season in Northern China (Xing et al., 2013), and thus we adopted 1.6 as the  $f$  in this study.  $k_{org}$  is the organic hygroscopicity parameter and depends on organic functionality, water solubility, molecular weight, and oxidation level. Han et al. (2022) have reported that the  $k_{org}$  generally increased with O: C ratios, with a range of 0–0.3 for 23 organics, including carboxylic acids, amino acids, sugars, and alcohols. Gunthe

et al, (2011) estimated a  $k_{org} = 0.06 \pm 0.01$  for the effective average hygroscopicity of the non-refractory organic particulate matter in the aerosols in Beijing. Our previous study has estimated that the uncertainties of  $k_{org}$  value (0.06) for pH in the range of 0–0.3 only lead to –1–3% errors, which can be neglected (Wang et al., 2023a). Therefore, the value of 0.06 was selected in this paper.  $\rho_s$  is the organic density, which was chosen to be 1.35 g/cm<sup>3</sup> following previous studies (Table S2).”

**Table S2.** The value of  $\rho_s$  in other studies.

Observation site	Period	$\rho_s$ (g/cm <sup>3</sup> )	Reference
Beijing	Dec 2016	1.4	(Liu et al., 2017)
Tianjin	Dec-Jun 2015	1.3	(Shi et al., 2017)
Xi’an	Nov-Dec 2012	1.4	(Guo et al., 2017)
Hohhot	Winter 2015	1.35	(Wang et al., 2019)
Northeastern USA	Feb-Mar 2015	1.4	(Guo et al., 2016)
Crete, Greece	Aug-Nov 2012	1.35	(Bougiatioti et al., 2016)
Alabama, USA	Jun-Jul 2013	1.4	(Guo et al., 2015)
Georgia, USA	Aug-Oct 2016	1.4	(Nah et al., 2018)

**Minor issues:**

6. The definition of TNH<sub>x</sub> is different in Line113 and Line 228.

**Response:** Thank you for your careful reading of our paper. The formula is used uniformly in the new version:

$$\text{TNH}_x = 17 \times \left( \frac{[\text{NH}_4^+]}{18} + \frac{[\text{NH}_3]}{17} \right)$$

7. Line 42, the study cited is the result based on a field campaign.

**Response:** Thank you for your comment. We added more references: “Nitrous acid (HONO) is a critical precursor of hydroxyl radical (OH), contributing to more than 60%

of OH production (Alicke, 2003; Platt et al., 1980; Kleffmann et al., 2005).”

8. Figure 2, the max and min as error bars provide little information about the general trends, and there are negative values.

**Response:** Thank you for your comments. We redrew Figure 2 as a box diagram and the negative values were removed after quality control.



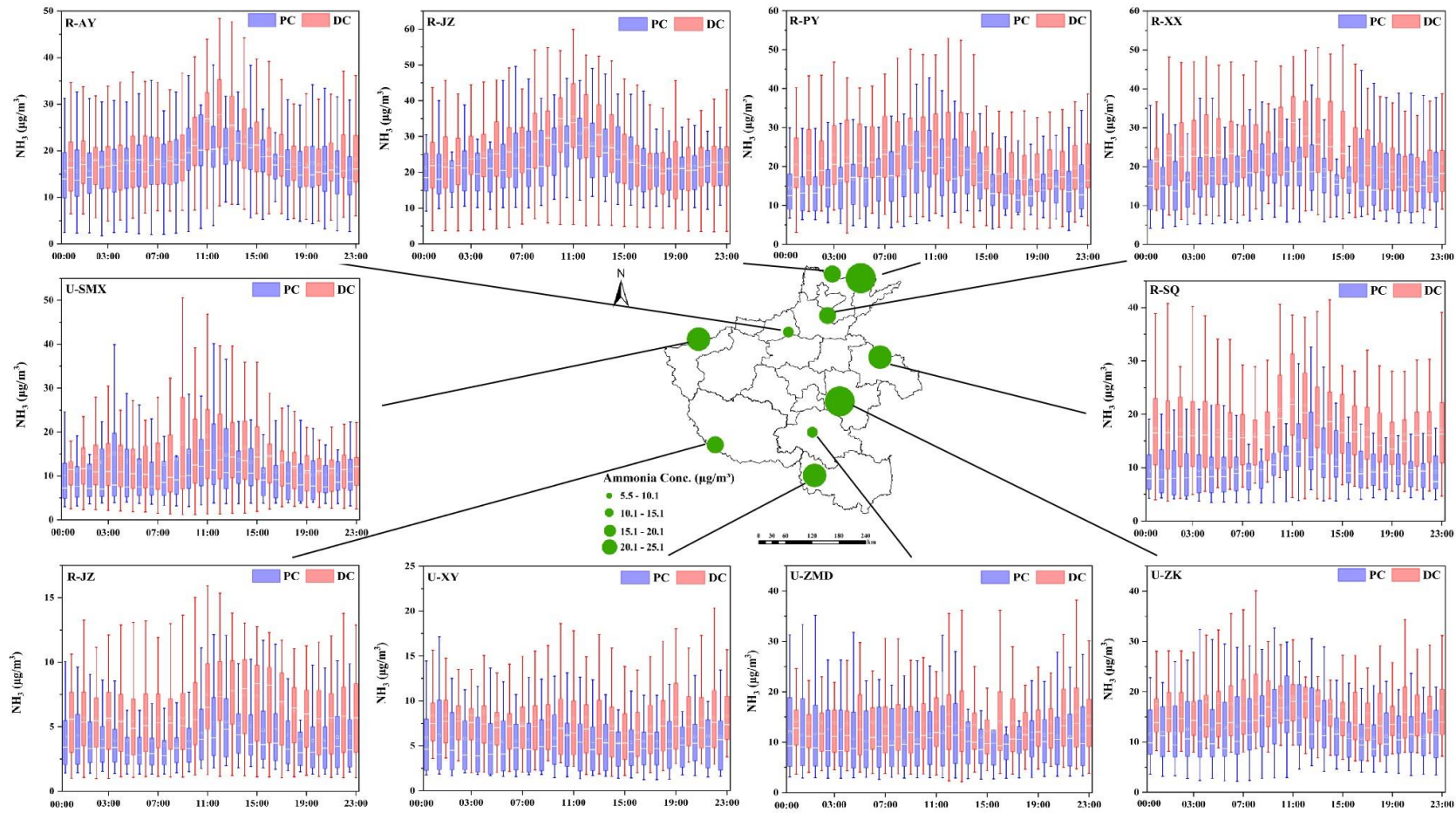


Figure 2. Daily variation of  $\text{NH}_3$  concentration at ten sites before (PC) and during (DC) the COVID-19 outbreak. The green dots represent the location of ten sites and their size represents the concentration of  $\text{NH}_3$ ; In each box, the top, middle, and bottom lines represent the 75, 50, and 25 percentiles of statistical data, respectively; the upper and lower whiskers represent the 90 and 10 percentiles of statistical data, respectively.

9. Line 215, it is hard to judge if agricultural activity got weakened or not. The  $\text{NH}_3$  concentration change could be due to less farm activity like less frequent animal feces cleaning, relatively higher temperature or a different regional transportation pattern.

**Response:** Thank you for your valuable suggestions. We have removed the speculation:

1 **Manuscript**

2 **Measurement Report: Elevated excess-NH<sub>3</sub> can**  
3 **promote the redox reaction to produce HONO:**  
4 **Insights from the COVID-19 pandemic**

5 Xinyuan Zhang<sup>1,2</sup>, Lingling Wang<sup>3</sup>, Nan Wang<sup>3</sup>, Shuangliang Ma<sup>3</sup>, Shenbo  
6 Wang<sup>2,4</sup>\*, Ruiqin Zhang<sup>2,4\*\*</sup>, Dong Zhang<sup>1,2</sup>, Mingkai Wang<sup>2,4</sup>, Hongyu  
7 Zhang<sup>1,2</sup>.

8  
9 <sup>1</sup> College of Chemistry, Zhengzhou University, Zhengzhou, 450000, China

10 <sup>2</sup> Research Institute of Environmental Sciences, Zhengzhou University, Zhengzhou  
11 450000, China

12 <sup>3</sup> Henan Provincial Ecological Environment Monitoring and Safety Center, Zhengzhou,  
13 450000, China

14 <sup>4</sup> School of Ecology and Environment, Zhengzhou University, Zhengzhou, 450000,  
15 China

16

17 **Correspondence:** Shenbo Wang (shbwang@zzu.edu.cn) and Ruiqin Zhang  
18 (rqzhang@zzu.edu.cn)

19

20 **Abstract**

21 **HONO plays a crucial role as a precursor to OH radicals in the tropospheric atmosphere.**

22 **The incongruity between HONO concentration and NO<sub>x</sub> emissions during the COVID-**

23 **19 pandemic remains puzzling.** Here, we show evidence from field observations of ten

24 sites in China that there was a noticeable increase in NH<sub>3</sub> concentrations during the

25 COVID-19 pandemic. In addition to the meteorological conditions, the significant

26 decrease in sulfate and nitrate concentrations enhanced the portioning of NH<sub>4</sub><sup>+</sup> to NH<sub>3</sub>.

27 Such conditions enable enhanced particle pH values, which in turn accelerate the redox

28 reactions between NO<sub>2</sub> and SO<sub>2</sub> to form HONO. This mechanism partly explains the

29 lower reduction of HONO concentration than that of NO<sub>2</sub> concentration during the

30 pandemic and highlights the importance of coordinating the control of SO<sub>2</sub>, NO<sub>x</sub>, and

31 NH<sub>3</sub> emissions.

32 **Keywords:** Ammonia, HONO, Gas-particle portioning, Acidity, COVID-19 pandemic

33

## 34 **1. Introduction**

35 Nitrous acid (HONO) is a critical precursor of hydroxyl radical (OH), contributing  
36 to more than 60% of OH production (Alicke, 2003; Platt et al., 1980; Kleffmann et al.,  
37 2005). The OH can react with carbon monoxide, nitrogen oxides (NO<sub>x</sub>), sulfur dioxide  
38 (SO<sub>2</sub>), and volatile organic compounds to produce secondary pollutants such as ozone  
39 (O<sub>3</sub>) and PM<sub>2.5</sub> (particulate matter with an aerodynamic diameter less than or equal to  
40 2.5 μm), thereby affecting air quality, human health, and global climate change (Li et  
41 al., 2021a; Wang et al., 2023b; Lu et al., 2018)

42 High concentrations of HONO are present in urban daytime atmospheres, and  
43 exploring its sources has become a hot and challenging topic in the field of atmospheric  
44 chemistry (Jiang et al., 2022; Xu et al., 2019). Various sources of atmospheric HONO  
45 have been identified, including combustion processes (e.g., vehicle emissions) (Kramer  
46 et al., 2020; Liao et al., 2021; Li et al., 2021b), direct emissions from soil (Su and Zhang,  
47 2011; Oswald et al., 2013; Meusel et al., 2018), homogeneous reactions between NO  
48 and OH radicals (Pagsberg et al., 1997; Atkinson et al., 2004), heterogeneous reactions  
49 of NO<sub>2</sub> on aerosols and ground surfaces (Zhang et al., 2020a; McFall et al., 2018; Liu  
50 et al., 2014, 2020a), and photolysis of nitrate (Spataro and Ianniello, 2014; Scharko et  
51 al., 2014; Romer et al., 2018; Ye et al., 2017; Shi et al., 2021). During the pandemic  
52 control periods, there was a substantial reduction in vehicle traffic flow and industrial  
53 emissions, leading to a decrease of more than 60% in NO<sub>x</sub> emissions in eastern China  
54 (Huang et al., 2021a). It was initially expected that the concentration of HONO would  
55 also decrease proportionally. However, Liu et al. (2020b) observed that the decrease in

56 HONO concentration during the pandemic period was only 31%, which was  
57 significantly lower than the reductions in NO (62%) and NO<sub>2</sub> (36%). Furthermore, the  
58 observed concentrations of HONO during the COVID-19 pandemic in 2020 were  
59 higher than those during the corresponding period in 2021 in Beijing (Luo et al., 2023).  
60 These findings suggest the existence of a considerable unknown source of HONO  
61 during the COVID-19 pandemic period.

62 Ammonia (NH<sub>3</sub>) is a primary alkaline gas in the atmosphere, capable of influencing  
63 the pH level of particulate matter and plays a crucial role in the atmospheric nitrogen  
64 cycle (Gu et al., 2022; Xu et al., 2020; Gong et al., 2011). Several studies have indicated  
65 that NH<sub>3</sub> can promote the formation of HONO by promoting the hydrolysis of NO<sub>2</sub> (Xu  
66 et al., 2019) or the redox reaction of NO<sub>2</sub> with SO<sub>2</sub> (Liu et al., 2023). Moreover,  
67 previous studies have reported that NH<sub>3</sub> concentrations in the atmosphere, particularly  
68 in rural areas, significantly increased during the pandemic (Xu et al., 2022; Cui, 2023;  
69 Zhang et al., 2020b). Consequently, the rise in NH<sub>3</sub> may contribute to the enhanced  
70 formation of HONO (Huang et al., 2021a). Unfortunately, there is currently a lack of  
71 research on the relationship between enhanced NH<sub>3</sub> and HONO during the COVID-19  
72 pandemic period.

73 To address this, online observational data on the chemical composition of PM<sub>2.5</sub>,  
74 gaseous pollutants, and meteorological conditions at ten sites in China before and  
75 during the COVID-19 pandemic period were analyzed to investigate the variation in  
76 NH<sub>3</sub> concentrations and particle pH, and explore the promoting effect of increased pH  
77 values on HONO formation.

## 78 **2. Materials and methods**

### 79 **2.1 Observation sites**

80 Online measurements were conducted at four urban and six rural sites in Henan  
81 Province, China from January 1 to February 29, 2020, including Sanmenxia (U-SMX),  
82 Zhoukou (U-ZK), Zhumadian (U-ZMD), and Xinyang (U-XY), as well as rural  
83 locations including Anyang (R-AY), Xinxiang (R-XX), Jiaozuo (R-JZ), Shangqiu (R-  
84 SQ), Nanyang (R-NY), and Puyang (R-PY). Descriptions and the spatial distribution  
85 of these ten sites can be found in Table S1 and Fig. S1.

### 86 **2.2 Measurements**

87 The aerosol and gas monitor (MARGA, Metrohm, Switzerland) was used to analyze  
88 the hourly water-soluble ions ( $\text{Na}^+$ ,  $\text{NH}_4^+$ ,  $\text{K}^+$ ,  $\text{Mg}^{2+}$ ,  $\text{Ca}^{2+}$ ,  $\text{Cl}^-$ ,  $\text{NO}_3^-$ , and  $\text{SO}_4^{2-}$ ) in  $\text{PM}_{2.5}$ ,  
89 as well as gaseous species ( $\text{NH}_3$ ,  $\text{HNO}_3$ ,  $\text{HCl}$ , and  $\text{HONO}$ ) at ten sampling sites. The  
90 MARGA instrument is widely used (Chen et al., 2017; Stieger et al., 2019; Twigg et al.,  
91 2022). A detailed description of the instrument and QA/QC can be found in Text S1. In  
92 brief, the atmospheric sample passes through a  $\text{PM}_{2.5}$  cut-off head, and both particles  
93 and gases enter a wet rotating dissolution device for diffusion. Subsequently, the  
94 particles in the sample undergo hygroscopic growth and condensation in an aerosol  
95 supersaturated vapor generator, followed by collection and ion chromatographic  
96 analysis. The gases in the sample are oxidized by  $\text{H}_2\text{O}_2$  in the dissolution device,  
97 absorbed into a liquid solvent, and then entered the gas sample collection chamber for

98 ion chromatographic quantification. The range of minimum detection limits for water-  
99 soluble ions was between 0.002  $\mu\text{g}/\text{m}^3$  ( $\text{Cl}^-$ ) to 0.081  $\mu\text{g}/\text{m}^3$  ( $\text{NH}_4^+$ ). Uncertainties of 20%  
100 are assumed for the detection of  $\text{NH}_3$  and  $\text{NH}_4^+$ , while uncertainties of 10% are assumed  
101 for other components (Wang et al., 2020, 2022a). **In addition, a detailed description of**  
102 **HONO measurement using this system can be found in Text S2.** Overall, the limit of  
103 detection for HONO was 4 pptv and the uncertainty was estimated to be  $\pm 20\%$ .

104 The data for  $\text{NO}_2$  and  $\text{SO}_2$  were obtained from a series of instruments provided by  
105 Thermo Fisher Scientific (USA). The hourly concentrations of organic carbon (OC) in  
106  $\text{PM}_{2.5}$  were analyzed using a carbon analyzer (Model 4, Sunset Laboratory., USA).  
107 Detailed descriptions of the  $\text{NO}_2$ ,  $\text{SO}_2$ , and carbon analyzers can be found in Text S3.  
108 The smart weather stations (LUFFTWS500, Sutron, Germany) were utilized for  
109 synchronized observation of meteorological parameters including pressure,  
110 temperature (T), and relative humidity (RH).

## 111 **2.3 Data analysis.**

### 112 **2.3.1 pH prediction.**

113 The thermodynamic model ISORROPIA-II was used to estimate the pH value of the  
114 particles (Fountoukis, 2007) by inputting RH, T,  $\text{K}^+$ ,  $\text{Ca}^{2+}$ ,  $\text{Mg}^{2+}$ , total ammonia  
115 ( $\text{TNH}_x = 17 \times (\frac{[\text{NH}_4^+]}{18} + \frac{[\text{NH}_3]}{17})$ ), total sulfuric acid ( $\text{TH}_2\text{SO}_4$ ,  $\text{SO}_4^{2-}$ ), total sodium  
116 ( $\text{TNa}$ ,  $\text{Na}^+$ ), total chlorine ( $\text{TCl}$ ,  $\text{Cl}^-$ ), and total nitrate ( $\text{TNO}_3 = \text{NO}_3^- + \text{HNO}_3$ ). The  
117 model has two calculation modes: the forward mode and reverse mode, and the aerosol



118 dissolution systems can be set to simulate a metastable state (aqueous phase) or stable  
 119 state (aqueous and solid phase). Studies have shown that the forward mode is less  
 120 affected by instrument measurement errors than the reverse mode (Ding et al., 2019;  
 121 Song et al., 2018). Additionally, the minimum average RH of about 55% was recorded  
 122 during the sampling period at the ten sites. Thus, ISORROPIA-II was run in the forward  
 123 model for the aerosol system in the metastable condition and only used data with RH  $\geq$   
 124 30% for simulation accuracy (Ding et al., 2019; Song et al., 2018). The ISORROPIA  
 125 model calculated the particle hydrate ion concentration per volume of air ( $H_{\text{air}}^+$ ) and  
 126 aerosol water associated with inorganic matter ( $AWC_{\text{inorg}}$ ). The pH value was calculated  
 127 using the following equation (Bougiatioti et al., 2016):

$$128 \quad \text{pH} = -\log_{10} H_{\text{aq}}^+ = -\log_{10} \frac{1000H_{\text{air}}^+}{AWC_{\text{inorg}} + AWC_{\text{org}}} \quad (2.1)$$

129 where the modeled concentrations for  $AWC_{\text{inorg}}$  and  $H_{\text{air}}^+$  are  $\mu\text{g}/\text{m}^3$ , and  $AWC_{\text{org}}$  is the  
 130 particle water associated with the organic matters predicted using the following method:

$$131 \quad AWC_{\text{org}} = \frac{m_s}{\rho_s} \frac{k_{\text{org}}}{\left(\frac{1}{\text{RH}} - 1\right)} \quad (2.2)$$

132 where  $m_s$  is the mass concentration of organic matter ( $\text{OM} = \text{OC} \times f$ ). The  $f$  is the  
 133 conversion factor of OC, which is dependent on the extent of OM oxidation and  
 134 secondary organic aerosol formation (Chow et al., 2015). Studies on the ratio of  
 135 OM/OC in fourteen cities in China suggested that the mean value of  $f$  was  $1.59 \pm 0.18$   
 136 during the winter season in Northern China (Xing et al., 2013), and thus we adopted 1.6  
 137 as the  $f$  in this study.  $k_{\text{org}}$  is the organic hygroscopicity parameter and depends on organic  
 138 functionality, water solubility, molecular weight, and oxidation level. Han et al. (2022)

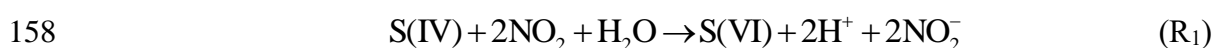
139 have reported that the  $k_{org}$  generally increased with O: C ratios, with a range of 0–0.3  
140 for 23 organics, including carboxylic acids, amino acids, sugars, and alcohols. Gunthe  
141 et al, (2011) estimated a  $k_{org} = 0.06 \pm 0.01$  for the effective average hygroscopicity of  
142 the non-refractory organic particulate matter in the aerosols in Beijing. Our previous  
143 study has estimated that the uncertainties of  $k_{org}$  value (0.06) for pH in the range of 0–  
144 0.3 only lead to –1–3% errors, which can be neglected (Wang et al., 2023a). Therefore,  
145 the value of 0.06 was selected in this paper.  $\rho_s$  is the organic density, which was chosen  
146 to be 1.35 g/cm<sup>3</sup> following previous studies (Table S2).

### 147 **2.3.2 The sources of HONO**

148 The sources of HONO include direct emission ( $P_{emi}$ ), the homogeneous reaction of  
149 NO and •OH ( $P_{OH+NO}$ ), the heterogeneous reaction of NO<sub>2</sub> on the ground ( $P_{ground}$ ) and  
150 aerosol ( $P_{aerosol}$ ), the photo-enhanced heterogeneous reaction of NO<sub>2</sub> on the ground  
151 ( $P_{ground+hv}$ ) and aerosol ( $P_{aerosol+hv}$ ), and nitrate photolysis ( $P_{nitrate}$ ). The detailed  
152 calculation method is described in the Supplementary Material (Text S4, Table S3, Figs.  
153 S2 and S3)

### 154 **2.3.3 Redox reaction of NO<sub>2</sub> with SO<sub>2</sub>.**

155 The redox reaction of NO<sub>2</sub> with SO<sub>2</sub> (R<sub>1</sub>) is considered a crucial potential source of  
156 high concentrations of HONO in Northern China (Cheng et al., 2019; Wang et al.,  
157 2016b):



159 the rate expression for reaction (R<sub>1</sub>) was estimated to:

$$160 \quad d[S(VI)] / dt = k_1[NO_2][S(VI)], \quad (2.3)$$

161 the rate constant  $k_1$  value is pH dependent, e.g., for pH, 5,  $k_1 = (1.4 \times 10^5 + 1.24 \times 10^7)/2$   
162  $M^{-1} s^{-1}$ . For  $k_1$  values under other pH conditions and other related information, please  
163 refer to Text S5, Table S4, and Table S5.

## 164 **3. Results and discussion**

### 165 **3.1 Variations of NH<sub>3</sub>, NH<sub>4</sub><sup>+</sup> and TNH<sub>x</sub>.**

166 The temporal variations of NH<sub>3</sub>, NH<sub>4</sub><sup>+</sup>, and TNH<sub>x</sub> at 10 sampling sites in the pre-  
167 COVID-19 pandemic period (PC, January 1 to 23, 2020) and during the COVID-19  
168 pandemic period (DC, January 24 to February 29, 2020) are presented in Fig. 1, with  
169 their average concentration listed in Table 1. In general, rural sites exhibited higher  
170 concentrations of NH<sub>3</sub>, NH<sub>4</sub><sup>+</sup>, and TNH<sub>x</sub> compared to urban sites, except for the R-NY  
171 site. This finding is consistent with previous studies conducted in Zhengzhou (Wang et  
172 al., 2020), Shanghai (Chang et al., 2019), and Quzhou (Feng et al., 2022a), owing to  
173 the intense agricultural ammonia emissions. The highest concentrations of NH<sub>3</sub> and  
174 TNH<sub>x</sub> were recorded at site R-JZ, with average values of  $25.3 \pm 11.5$  and  $40.8 \pm 20.1$   
175  $\mu\text{g}/\text{m}^3$ , respectively. Site R-AY had the highest NH<sub>4</sub><sup>+</sup> concentration, measuring  $19.3 \pm$   
176  $12.9 \mu\text{g}/\text{m}^3$ . Note that the current study area exhibited higher NH<sub>3</sub> levels compared to  
177 other regions (Table S6), which probably was attributed to the highest NH<sub>3</sub> emissions  
178 of Henan Province in China, primarily from nitrogen fertilizer application and livestock  
179 farming (Wang et al., 2018; Ma, 2020).

180 Compared to the PC, NH<sub>3</sub> concentrations increased in the DC at all sites. Notably,  
181 rural sites experienced more significant increases in NH<sub>3</sub> concentrations than urban  
182 sites, which was similar to the trend in Shanghai (Xu et al., 2022). The largest increases  
183 in NH<sub>3</sub> concentrations were observed at R-SQ (71%, 7.3 µg/m<sup>3</sup>) and U-ZK (37%, 4.8  
184 µg/m<sup>3</sup>) for rural and urban sites, respectively. In contrast, the concentrations of NH<sub>4</sub><sup>+</sup>  
185 and TNH<sub>x</sub> decreased in the DC with the largest reduction at rural site R-PY (51%, 12.9  
186 µg/m<sup>3</sup>) and urban site U-ZMD (48%, 9.3 µg/m<sup>3</sup>). Regarding TNH<sub>x</sub>, rural sites exhibited  
187 larger reductions, with site R-SQ experiencing the largest decrease of 37% (4.7 µg/m<sup>3</sup>).

188 Figure 2 illustrates the spatial distribution and the diurnal variation of NH<sub>3</sub>  
189 concentrations at the ten sites before and during the pandemic. NH<sub>3</sub> concentrations in  
190 most sites exhibited an unimodal trend in PC that NH<sub>3</sub> concentrations gradually  
191 increased after sunrise, reaching a peak around noon (11:00–12:00), and then decreased  
192 to a valley around 16:00–17:00. This diurnal pattern is similar to NH<sub>3</sub> variations  
193 observed in urban areas of Houston, USA, as a result of the natural emissions from  
194 vegetation and soil during photosynthesis (Gong et al., 2011). However, other studies  
195 have recorded a significant NH<sub>3</sub> peak during the early morning of 8:00–10:00 (Ellis et  
196 al., 2011; Meng et al., 2018; Gu et al., 2022), suggesting the influence of vehicle  
197 emissions (Gong et al., 2011; Gu et al., 2022), residual NH<sub>3</sub> mixing, soil or plant  
198 emissions (Ellis et al., 2011), and dew volatilization (Wentworth et al., 2016; Huang et  
199 al., 2021b). Therefore, the NH<sub>3</sub> in urban and rural areas of this study was probably less  
200 affected by NH<sub>3</sub> emissions from vehicles, different from the recent studies in megacities  
201 of China (e.g., Beijing and Shanghai) (Gu et al., 2022; Wu et al., 2023; Zhang et al.,

202 2020b). In addition to the transport from agricultural emissions, urban NH<sub>3</sub> in this  
203 region might also originate from other non-agricultural sources, such as wastewater  
204 treatment, coal combustion, household waste, urban green spaces, and human  
205 excrement (Chang et al., 2019).

206 During the COVID-19 pandemic, the diurnal variation of NH<sub>3</sub> in both urban and rural  
207 sites still maintained a unimodal distribution. The peak values in urban sites remained  
208 consistent with PC levels, further demonstrating that the influence of vehicles on NH<sub>3</sub>  
209 in urban areas was limited. Notably, the peak time of NH<sub>3</sub> in rural sites shifted 1–2 hours  
210 earlier compared to the trend in PC. Ammonia in rural areas primarily originates from  
211 nitrogen fertilizer application, livestock, and poultry breeding (Feng et al., 2022b;  
212 Meng et al., 2018), which are significantly influenced by T and RH (Liu et al., 2023).  
213 Table S7 and Fig. S4 reveal that there was an increased T and a decreased RH at rural  
214 sites in the DC than the PC, which could accelerate the evaporation of NH<sub>3</sub> and thus  
215 potentially lead to earlier peak NH<sub>3</sub> concentrations.

### 216 **3.2 Gas-to-particle conversion of NH<sub>3</sub>**

217 **The increased NH<sub>3</sub> accompanying decreased NH<sub>4</sub><sup>+</sup> in the DC suggests that the gas-**  
218 **particle partition of NH<sub>3</sub>/ NH<sub>4</sub><sup>+</sup> may determine the elevated NH<sub>3</sub> concentrations.**

219 Meteorological parameters, including RH and T, play a crucial role in the gas-particle  
220 partitioning of NH<sub>3</sub> (Liu et al., 2023; Xu et al., 2020). Therefore, the higher T and lower  
221 RH in the DC (Table S7 and Fig. S4) favored the conversion of NH<sub>4</sub><sup>+</sup> to NH<sub>3</sub>, resulting  
222 in a decrease in  $\epsilon(\text{NH}_4^+)$  ( $[\text{NH}_4^+]/([\text{NH}_3] + [\text{NH}_4^+])$ ) compared to those in the PC (Table

223 S7).

224 NH<sub>3</sub> primarily enters particles to neutralize acidic ions (Wang et al., 2020; Xu et al.,  
225 2020; Liu et al., 2017; Ye et al., 2011; Wells, 1998). Accordingly, the concentrations of  
226 required ammonia (Required-NH<sub>x</sub>) and excess ammonia (Excess-NH<sub>x</sub>) were calculated  
227 based on the acidic substances as follows (Wang et al., 2020):

$$\begin{aligned} \text{Required-NH}_x = & 17 \times \left( \frac{[\text{SO}_4^{2-}]}{48} + \frac{[\text{NO}_3^-]}{63} + \frac{[\text{Cl}^-]}{35.5} + \frac{[\text{HNO}_3]}{64} + \frac{[\text{HCl}]}{36.5} \right) \\ & - 17 \times \left( \frac{[\text{Na}^+]}{23} + \frac{[\text{K}^+]}{39} + \frac{[\text{Ca}^{2+}]}{20} + \frac{[\text{Mg}^{2+}]}{12} \right) \end{aligned} \quad (3.1)$$

$$\text{Excess-NH}_x = \text{TNH}_x - \text{Required-NH}_x \quad (3.2)$$

230 where [W] represents the concentration of the substance (μg/m<sup>3</sup>). The significant linear  
231 fitting (R<sup>2</sup> is greater than 0.96, and the slope is close to 1) in Fig. S5 demonstrates that  
232 the anions and cations at each site were close to the equilibrium state. Therefore, the  
233 organic acids in PM<sub>2.5</sub> may have less effect on NH<sub>3</sub> and NH<sub>4</sub><sup>+</sup> and were not considered  
234 in Formula 3.1.

235 As shown in Fig. 3 and Table S8, compared to those in the PC, the concentration of  
236 Required-NH<sub>x</sub> in the DC significantly decreased (ranging from 37% at site R-JZ to 58%  
237 at site R-PY), while the concentration of Excess-NH<sub>x</sub> increased (ranging from 9% at  
238 site R-AY to 78% at site R-SQ). The reduction in the concentrations of sulfate and  
239 nitrate (Fig. S6) was responsible for the decrease in the concentration of Required-NH<sub>x</sub>.  
240 To sum up, in addition to meteorological conditions, the substantial reduction in  
241 anthropogenic emissions of SO<sub>2</sub>, NO<sub>x</sub>, and other pollutants in the DC had led to a  
242 decrease in acidic substances (e.g., sulfate and nitrate) in particles, in turn, resulting in  
243 more gas-phase NH<sub>3</sub> concentration remaining in the atmosphere.

### 244 3.3 Particle pH before and during COVID-19

245 Diurnal patterns of particle pH in PC and DC at ten sites are summarized in Fig. 4  
246 with their average values listed in Table S9.  $PM_{2.5}$  shows consistent moderate acidity,  
247 with mean values in the range of 4.2–5.1, which were close to the values in previous  
248 studies (Table S9). Compared to the PC, the particle pH at ten sites increased obviously  
249 in the DC, with the highest increase of 0.5 (U-ZK) and 0.3 (R-PY) at urban and rural  
250 sites, respectively, which were the subject of in-depth discussion in the following text.

251 To explore the dominant factors that determine the local particle pH level and result  
252 in the high pH during the DC, sensitivity tests of pH to chemical species (i.e.,  $TNH_x$ ,  
253  $TH_2SO_4$ ,  $TNO_3$ , TCl, TNa,  $K^+$ ,  $Ca^{2+}$ , and  $Mg^{2+}$ ) and meteorological parameters (i.e., T  
254 and RH) were performed. A given range for a variable (i.e.,  $TNH_x$ ) with corresponding  
255 average values of other parameters (i.e.,  $TH_2SO_4$ ,  $TNO_3$ , TCl, TNa,  $K^+$ ,  $Ca^{2+}$ ,  $Mg^{2+}$ , T,  
256 and RH) was input into the model and simulated to compare its effects on pH. As shown  
257 in Fig. S7, pH increases with the cation concentrations (i.e.,  $TNH_x$ ,  $Na^+$ ,  $K^+$ ,  $Ca^{2+}$ , and  
258  $Mg^{2+}$ ) increasing as well as the anion concentrations (i.e.,  $TH_2SO_4$ ,  $TNO_3$ , and Cl<sup>-</sup>), T  
259 and RH decreasing. According to the average values of input data during PC (Blue line  
260 in Fig. S7) and DC (Red line in Fig. S7) at U-ZK and R-PY sites respectively, the  
261 changes in pH ( $\Delta pH$  in Fig. 5) indicate that the decrease in  $TNH_x$  concentration and the  
262 increase in T in DC led to a decrease in pH values ( $\Delta pH$ : 0.09 at U-ZK and 0.08 at R-  
263 PY sites) compared to PC. However, this effect was outweighed by the decrease in  
264  $TH_2SO_4$  ( $\Delta pH$ : 0.07 and 0.8 at U-ZK and R-PY sites, respectively) and  $TNO_3$  ( $\Delta pH$ :  
265 0.05 and 0.4 at U-ZK and R-PY sites, respectively) concentrations as well as the

266 increase in  $K^+$  ( $\Delta\text{pH}$ : 0.03 at U-ZK and 0.2 at R-PY site) and  $Mg^{2+}$  ( $\Delta\text{pH}$ : 0.01 at U-ZK  
267 and 0.04 at R-PY site) concentrations in the DC, and resulting in an overall increase in  
268 pH values in the DC. Furthermore, the relationship between particle pH with the  
269 concentrations of Required- $\text{NH}_x$ , and Excess- $\text{NH}_x$ , which considers all chemical  
270 components, is investigated to examine the dominant factor on the increasing pH in DC.  
271 As shown in Fig. 6, the higher Excess- $\text{NH}_x$  concentrations in the DC led to higher  
272 increases in pH values ( $\Delta\text{pH}$ : 1 at U-ZK and 0.5 at R-PY site) than those in PC ( $\Delta\text{pH}$ :  
273 0.3 at U-ZK and 0.2 at R-PY site), thus Excess- $\text{NH}_x$  concentrations may be the key  
274 factor in promoting the pH values.

### 275 **3.4 The influence of pH on HONO.**

276 The observed HONO concentrations decreased by 18% and 54% at U-ZK (0.8 ppb)  
277 and R-PY (0.9 ppb) sites in the DC, respectively, compared to those (1.0 and 2.2 ppb)  
278 in the PC. Moreover, all the known HONO production sources rates including  $P_{\text{emi}}$ ,  $P_{\text{OH}}$   
279  $+ \text{NO}$ ,  $P_{\text{ground}}$ ,  $P_{\text{ground+hv}}$ ,  $P_{\text{aerosol}}$ ,  $P_{\text{aerosol+hv}}$ , and  $P_{\text{nitrate}}$  (Fig. 7) show a decreasing trend from  
280 PC to DC, with the total reductions of 42% and 80% for U-ZK and R-PY, respectively.  
281 At the U-ZK,  $P_{\text{ground+hv}}$  decreased the most (84%), while at the R-PY,  $P_{\text{nitrate}}$  had the  
282 largest decrease about 85%, which was speculated to be related to the decrease of  $\text{NO}_x$   
283 and  $\text{NO}_3^-$  concentration in DC. Note that the reduction rates in the overall known source  
284 and almost individual sources were greater than the reduction rates in HONO  
285 concentrations (Figs. 7 and 8), thus we hypothesized that there should be other sources  
286 capable of promoting HONO production. Soil emission has been demonstrated to be a



287 major source of HONO, which is affected by temperature to some extent (Liu et al.,  
288 2020b, 2020c). However, there was no significant positive correlation with temperature  
289 in Fig. S8, and temperatures did not exceed 10°C during the study periods, suggesting  
290 that soil emission may not be a major contributor to HONO. Note that there were  
291 positive correlations between HONO with SO<sub>2</sub>, Excess-NH<sub>x</sub>, SO<sub>4</sub><sup>2-</sup>, and pH (Fig. S8)  
292 indicating that the R<sub>1</sub> reaction might form an amount of HONO and contribute to less  
293 reduction in the observed HONO concentrations.

294 Considering that R<sub>1</sub> mainly reacts in the liquid phase, the calculated reaction rates of  
295 R<sub>1</sub> under the conditions of RH > 60% in the PC and DC periods are illustrated in Figs.  
296 8 and S9. Despite the decrease in NO<sub>2</sub> and SO<sub>2</sub> concentrations in the DC, the increase  
297 in particle pH, increasing HSO<sub>3</sub><sup>-</sup> concentration in the aqueous phase, promoted the R<sub>1</sub>  
298 reaction rates by 58% and 59% at U-ZK and R-PY (Figure 8), respectively.  
299 Consequently, the enhanced R<sub>1</sub> reaction might prevent a large decrease in HONO (18%  
300 at U-ZK and 53% at R-PY) under the conditions of a significant reduction in vehicle  
301 emissions and a decline of 66% and 69% in NO<sub>2</sub> concentrations at U-ZK and R-PY,  
302 respectively.

### 303 3.5 Uncertainty

304 According to sensitivity tests of pH (Fig. S7) and R<sub>1</sub> (Fig. S10), pH increases with  
305 the concentrations of cations (TNH<sub>x</sub>, TNa, K<sup>+</sup>, Ca<sup>2+</sup>, and Mg<sup>2+</sup>) and OC increasing as  
306 well as anions (TH<sub>2</sub>SO<sub>4</sub>, TNO<sub>3</sub>, and Cl<sup>-</sup>) concentrations, T, and RH decreasing. R<sub>1</sub>  
307 reaction rate increases with the concentrations of AWC, NO<sub>2</sub>, SO<sub>2</sub>, pH, and pressure,

308 while increasing as well as T decreasing. Therefore, two extreme scenarios (i.e., the  
309 maximum and minimum rate scenarios) were evaluated to estimate the uncertainty of  
310 pH, and  $R_1$  based on the measurement uncertainties at the U-ZK and R-PY sites. Figure  
311 S11 suggests that the two extreme scenarios can be led to -10-7% and -71-125%  
312 uncertainties at the U-ZK site and -10-7% and -78-123% uncertainties at the R-PY  
313 site for pH and  $R_1$ , respectively.

#### 314 **4. Conclusions**

315 Elevated  $\text{NH}_3$  concentration was observed during the COVID-19 pandemic at both  
316 urban and rural sites in China. In addition to the rise in T and decrease in RH during the  
317 COVID-19 pandemic, which favored the conversion of  $\text{NH}_4^+$  to  $\text{NH}_3$ , the significant  
318 decrease in sulfate and nitrate concentrations led to the decline in Required- $\text{NH}_x$  and  
319 was beneficial to the particle-phase  $\text{NH}_4^+$  partitioning to gas-phase  $\text{NH}_3$ . Furthermore,  
320 under the environmental conditions of increased  $\text{NH}_3$  concentration and decreased  
321 acidic substance concentration, the pH values increased by 0.5 and 0.3 at U-ZK and R-  
322 PY increased during the pandemic, respectively. Consequently, the high pH values  
323 accelerated the formation rate of HONO through the oxidation-reduction reaction of  
324  $\text{NO}_2$  with  $\text{SO}_2$  (an increase of 58% at U-ZK and 59% at R-PY, respectively), partially  
325 compensating for the decrease in HONO concentration caused by the decline in vehicle  
326 emissions,  $\text{NO}_2$  and  $\text{NO}_3^-$  concentrations during the COVID-19 pandemic.

## 327 **5. Implications**

328 HONO plays a crucial role as a precursor to OH radicals in the tropospheric  
329 atmosphere (Xue, 2022). There have been significant observations of high HONO  
330 concentrations in urban areas during the daytime, leading to a growing interest in  
331 understanding its sources in atmospheric chemistry (Jiang et al., 2022; Xu et al., 2019).  
332 The heterogeneous reaction mechanism of NO<sub>2</sub> on aerosol surfaces is currently the  
333 focus of research on HONO sources, particularly in regions with elevated levels of  
334 atmospheric particulate matter, where it could potentially become a major contributor  
335 to HONO production (Zhang et al., 2022; Liao et al., 2021). One of the pathways for  
336 heterogeneous reactions on aerosol surfaces is the redox reaction of NO<sub>2</sub> with SO<sub>2</sub>.  
337 However, the significance of this reaction in HONO production in the real atmosphere  
338 is often overlooked, as it relies on the high pH of aerosols (Ge et al., 2019). In recent  
339 years, there has been increasing attention on the enhancing effect of NH<sub>3</sub> on the redox  
340 reaction, with laboratory experiments demonstrating its ability to generate substantial  
341 amounts of HONO (Ge et al., 2019). This study highlights the importance of this  
342 reaction based on actual atmospheric observations. Furthermore, numerous studies  
343 have indicated that if control over NH<sub>3</sub> emissions continues to relax while SO<sub>2</sub> and NO<sub>2</sub>  
344 emissions decrease, the particle pH in future China is expected to rise steadily (Xie et  
345 al., 2020; Song et al., 2019; Wang et al., 2020). **Consequently, the redox reaction of**  
346 **NO<sub>2</sub> with SO<sub>2</sub> could become a significant source of HONO in China.** Therefore, it is  
347 crucial to coordinate the control of SO<sub>2</sub>, NO<sub>x</sub>, and NH<sub>3</sub> emissions to avoid a rapid  
348 increase in the particle pH.

349

350 **Data availability:** All the data presented in this article can be accessed through  
351 <https://zenodo.org/records/10273539>. (Zhang, 2023).

352

353 **Author contributions.** XZ Data Curation, Writing - Original Draft, Visualization.  
354 LW, NW, SM, and DZ Investigation, Visualization, Data Curation. DZ, HZ, and MW  
355 Investigation. SW Conceptualization, Data Curation, Supervision. RZ Data Curation,  
356 Funding acquisition. All people are involved in the discussion of the results.

357

358 **Competing interest.** The authors declare no competing financial interest.

359

360 **Acknowledgments.** This work was supported by the China Postdoctoral Science  
361 Foundation (2023M733220), the Zhengzhou PM<sub>2.5</sub> and O<sub>3</sub> Collaborative Control and  
362 Monitoring Project (20220347A), and the National Key Research and Development  
363 Program of China (No. 2017YFC0212403).

364 **References**

- 365 Alicke, B.: OH formation by HONO photolysis during the BERLIOZ experiment, J.  
366 Geophys. Res.; 108, 8247, <https://doi.org/10.1029/2001JD000579>, 2003.
- 367 Atkinson, R., Baulch, D.L., Cox, R.A., Crowley, J.N., Hampson, R.F., Hynes, R.G.,  
368 Jenkin, M.E., and Rossi, M. J., Troe, J.: Evaluated kinetic and photochemical data  
369 for atmospheric chemistry: volume I - gas phase reactions of O<sub>x</sub>, HO<sub>x</sub>, NO<sub>x</sub> and  
370 SO<sub>x</sub> species., Atmos. Chem. Phys., 4,1461–1738, [https://doi.org/10.5194/acp-4-](https://doi.org/10.5194/acp-4-1461-2004)  
371 [1461-2004](https://doi.org/10.5194/acp-4-1461-2004), 2004.
- 372 Bougiatioti, A., Nikolaou, P., Stavroulas, I., Kouvarakis, G., Weber, R., Nenes, A.,  
373 Kanakidou, M., and Mihalopoulos, N.: Particle water and pH in the eastern  
374 Mediterranean: source variability and implications for nutrient availability, Atmos.  
375 Chem. Phys., 16, 4579–4591, <https://doi.org/10.5194/acp-16-4579-2016>, 2016.
- 376 Chang, Y., Zou, Z., Zhang, Y., Deng, C., Hu, J., Shi, Z., Dore, A. J., and Collett, J. L.,  
377 Jr.: Assessing contributions of agricultural and nonagricultural emissions to  
378 atmospheric ammonia in a Chinese megacity. Environ. Sci. Technol. 53, 1822–  
379 1833., <https://doi.org/10.1021/acs.est.8b05984>, 2019.
- 380 Chen, X., Walker, J. T., and Geron, C.: Chromatography related performance of the  
381 monitor for aerosols and gases in ambient air (MARGA): laboratory and field-  
382 based evaluation. Atmos. Meas. Tech. 10, 3893–3908.  
383 <https://doi.org/10.5194/amt-10-3893-2017>, 2017.
- 384 Cheng, Y., Zheng, G., Wei, C., Mu, Q., Zheng, B., Wang, Z., Gao, M., Z., Q., He, K.,  
385 Carmichael, G., Pöschl, U., and Su, and H.: Reactive nitrogen chemistry in aerosol

386 water as a source of sulfate during haze events in China, *Sci. Adv.* 2, e1601530.,  
387 <https://doi.org/10.1126/sciadv.1601530>, 2019.

388 Chow, J. C., Lowenthal, D. H., Chen, L. W. A., Wang, X., and Watson, J. G.: Mass  
389 reconstruction methods for PM<sub>2.5</sub>: a review, *Air Qual. Atmos. Health.*, 8, 243 – 263,  
390 <https://doi.org/10.1007/s11869-015-0338-3>, 2015.

391 Cui, L.: Impact of COVID-19 restrictions on the concentration and source  
392 apportionment of atmospheric ammonia (NH<sub>3</sub>) across India, *Sci. Total Environ.*,  
393 881, <https://doi.org/10.1016/j.scitotenv.2023.163443>, 2023.

394 Ding, J., Zhao, P., Su, J., Dong, Q., Du, X., and Zhang, Y.: Aerosol pH and its driving  
395 factors in Beijing, *Atmos. Chem. Phys.* 19, 7939–7954.,  
396 <https://doi.org/10.5194/acp-19-7939-2019>, 2019.

397 Ellis, R. A., Murphy, J. G., Markovic, M. Z., VandenBoer, T. C., Makar, P. A., Brook,  
398 J., and Mihele, C.: The influence of gas-particle partitioning and surface-  
399 atmosphere exchange on ammonia during BAQS-Met, *Atmos. Chem. Phys.* 11,  
400 133–145., <https://doi.org/10.5194/acp-11-133-2011>, 2011.

401 Feng, S., Xu, W., Cheng, M., Ma, Y., Wu, L., Kang, J., Wang, K., Tang, A., Collett, J.  
402 L., Fang, Y., Goulding, K., Liu, X., and Zhang, F.: Overlooked nonagricultural and  
403 wintertime agricultural NH<sub>3</sub> emissions in Quzhou county, north China plain:  
404 evidence from <sup>15</sup>N-Stable Isotopes. *Environ. Sci. Technol. Lett.* 9, 127–133,  
405 <https://doi.org/10.1021/acs.estlett.1c00935>, 2022a.

406 Feng, T., Zhao, S., Liu, L., Long, X., Gao, C., and Wu, N.: Nitrous acid emission from  
407 soil bacteria and related environmental effect over the North China Plain, *Chemos.*,  
408 287, <https://doi.org/10.1016/j.chemosphere.2021.132034>, 2022b.

409 Fountoukis, C., Nenes, A.: ISORROPIA II: a computationally efficient thermodynamic

410 equilibrium model for  $K^+$ - $Ca^{2+}$ - $Mg^{2+}$ - $NH_4^+$ - $Na^+$ - $SO_4^{2-}$ - $NO_3^-$ - $Cl^-$ - $H_2O$  aerosols.  
411 Atmos. Chem. Phys. 7, 4639–4659, <https://doi.org/10.5194/acp-7-4639-2007>,  
412 2007.

413 Ge, S., Wang, G., Zhang, S., Li, D., and Zhang, H.: Abundant  $NH_3$  in China enhances  
414 atmospheric HONO production by promoting the heterogeneous reaction of  $SO_2$   
415 with  $NO_2$ . Environ. Sci. Technol. 53, 14339–14347,  
416 <https://doi.org/10.1021/acs.est.9b04196>, 2019.

417 Gong, L., Lewicki, R., Griffin, R. J., Flynn, J. H., Lefer, B. L., and Tittel, F. K.:  
418 Atmospheric ammonia measurements in Houston, TX using an external-cavity  
419 quantum cascade laser-based sensor, Atmos. Chem. Phys. 11, 9721–9733,  
420 <https://doi.org/10.5194/acp-11-9721-2011>, 2011.

421 Gu, M., Pan, Y., Walters, W. W., Sun, Q., Song, L., Wang, Y., Xue, Y., and Fang, Y.:  
422 vehicular emissions enhanced ammonia concentrations in winter mornings: insights  
423 from diurnal nitrogen isotopic signatures. Environ. Sci. Technol. 56, 1578–1585,  
424 <https://doi.org/10.1021/acs.est.1c05884>, 2022.

425 Gunthe, S. S., Rose, D., Su, H., Garland, R. M., Achtert, P., Nowak, A., Wiedensohler,  
426 A., Kuwata, M., Takegawa, N., Kondo, Y., Hu, M., Shao, M., Zhu, T., Andreae, M.  
427 O., and Pöschl, U.: Cloud condensation nuclei (CCN) from fresh and aged air  
428 pollution in the megacity region of Beijing, Atmos. Chem. Phys., 11, 11023 –  
429 11039, <https://doi.org/10.5194/acp-11-11023-2011>, 2011.

430 Han, S., Hong, J., Luo, Q., Xu, H., Tan, H., Wang, Q., Tao, J., Zhou, Y., Peng, L., He,  
431 Y., Shi, J., Ma, N., Cheng, Y., and Su, H.: Hygroscopicity of organic compounds  
432 as a function of organic functionality, water solubility, molecular weight, and

433 oxidation level, *Atmos. Chem. Phys.*, 22, 3985–4004, <https://doi.org/10.5194/acp->  
434 [22-3985-2022](https://doi.org/10.5194/acp-22-3985-2022), 2022.

435 Huang, X., Ding, A., Gao, J., Zheng, B., Zhou, D., Qi, X., Tang, R., Wang, J., Ren, C.,  
436 Nie, W., Chi, X., Xu, Z., Chen, L., Li, Y., Che, F., Pang, N., Wang, H., Tong, D.,  
437 Qin, W., Cheng, W., Liu, W., Fu, Q., Liu, B., Chai, F., Davis, S. J., Zhang, Q., and  
438 He, K.: Enhanced secondary pollution offset reduction of primary emissions  
439 during COVID-19 lockdown in China, *Natl Sci Rev*, 8, nwaal37,  
440 <https://doi.org/10.1093/nsr/nwaa137>, 2021a.

441 Huang, X., Zhang, J., Zhang, W., Tang, G., and Wang, Y.: Atmospheric ammonia and  
442 its effect on PM<sub>2.5</sub> pollution in urban Chengdu, Sichuan Basin, China. *Environ.*  
443 *Pollut.* 291, 118–195. <https://doi.org/10.1016/j.envpol.2021.118195>, 2021b.

444 Jiang, Y., Xue, L., Shen, H., Dong, C., Xiao, Z., and Wang, W.: Dominant processes of  
445 HONO derived from multiple field observations in contrasting environments.  
446 *Environ. Sci. Technol. Lett.* 9, 258–264,  
447 <https://doi.org/10.1021/acs.estlett.2c00004>, 2022.

448 Kleffmann, J., Gavriiloaiei, T., Hofzumahaus, A., Holland, F., Koppmann, R., Rupp, L.,  
449 Schlosser, E., Siese, M., and Wahner, A.: Daytime formation of nitrous acid: A  
450 major source of OH radicals in a forest, *Geophys. Res. Lett.*, 32,  
451 <https://doi.org/10.1029/2005gl022524>, 2005.

452 Kramer, L. J., Crilley, L. R., Adams, T. J., Ball, S. M., Pope, F. D., and Bloss, W. J.:  
453 Nitrous acid (HONO) emissions under real-world driving conditions from vehicles  
454 in a UK road tunnel, *Atmos. Chem. Phys.* 20, 5231–5248,



455 <https://doi.org/10.5194/acp-20-5231-2020>, 2020.

456 Li, J., An, X., Cui, M., Sun, Z., Wang, C., and Li, Y.: Simulation study on regional  
457 atmospheric oxidation capacity and precursor sensitivity, *Atmos. Environ.* 263,  
458 118657, <https://doi.org/10.1016/j.atmosenv.2021.118657>, 2021a.

459 Li, S., Song, W., Zhan, H., Zhang, Y., Zhang, X., Li, W., Tong, S., Pei, C., Wang, Y.,  
460 Chen, Y., Huang, Z., Zhang, R., Zhu, M., Fang, H., Wu, Z., Wang, J., Luo, S., Fu,  
461 X., Xiao, S., Huang, X., Zeng, J., Zhang, H., Chen, D., Gligorovski, S., Ge, M.,  
462 George, C., and Wang, X.: Contribution of vehicle emission and NO<sub>2</sub> surface  
463 conversion to nitrous acid (HONO) in urban environments: implications from tests  
464 in a tunnel. *Environ. Sci. Technol.*, 55, 15616–15624,  
465 <https://doi.org/10.1021/acs.est.1c00405>, 2021.

466 Liao, S., Zhang, J., Yu, F., Zhu, M., Liu, J., Ou, J., Dong, H., Sha, Q., Zhong, Z., Xie,  
467 Y., Luo, H., Zhang, L., and Zheng, J.: High gaseous nitrous acid (HONO)  
468 emissions from light-duty diesel vehicles. *Environ. Sci. Technol.* 55, 200–208,  
469 <https://doi.org/10.1021/acs.est.0c05599>, 2021.

470 Liu, J., Deng, H., Lakey, P. S. J., Jiang, H., Mekic, M., Wang, X., Shiraiwa, M., and  
471 Gligorovski, S.: Unexpectedly high indoor HONO concentrations associated with  
472 photochemical NO<sub>2</sub> transformation on glass windows. *Environ. Sci. Technol.* 54,  
473 15680–15688, <https://doi.org/10.1021/acs.est.0c05624>, 2020a.

474 Liu, M., Song, Y., Zhou, T., Xu, Z., Yan, C., Zheng, M., Wu, Z., Hu, M., Wu, Y., and  
475 Zhu, T.: Fine particle pH during severe haze episodes in northern China. *Geophys.*  
476 *Res. Lett.* 44, 5213–5221, <https://doi.org/10.1002/2017gl073210>, 2017.

477 Liu, P., Chen, H., Song, Y., Xue, C., Ye, C., Zhao, X., Zhang, C., Liu, J., and Mu, Y.:  
478 Atmospheric ammonia in the rural North China Plain during wintertime: variations,  
479 sources, and implications for HONO heterogeneous formation. *Sci. Total. Environ.*  
480 861, 160768, <https://doi.org/10.1016/j.scitotenv.2022.160768>, 2023.

481 Liu, Y., Ni, S., Jiang, T., Xing, S., Zhang, Y., Bao, X., Feng, Z., Fan, X., Zhang, L., and  
482 Feng, H.: Influence of Chinese New Year overlapping COVID-19 lockdown on  
483 HONO sources in Shijiazhuang, *Sci. Total Environ.*, 745, 141025,  
484 <https://doi.org/10.1016/j.scitotenv.2020.141025>, 2020b.

485 Liu, Y., Zhang, Y., Lian, C., Yan, C., Feng, Z., Zheng, F., Fan, X., Chen, Y., Wang, W.,  
486 Chu, B., Wang, Y., Cai, J., Du, W., Daellenbach, K. R., Kangasluoma, J., Bianchi,  
487 F., Kujansuu, J., Petäjä, T., Wang, X., Hu, B., Wang, Y., Ge, M., He, H., and  
488 Kulmala, M.: The promotion effect of nitrous acid on aerosol formation in  
489 wintertime in Beijing: The possible contribution of traffic-related emissions,  
490 *Atmos. Chem. Phys*, 20, 13023–13040, [https://doi.org/10.5194/acp-20-13023-](https://doi.org/10.5194/acp-20-13023-2020)  
491 [2020](https://doi.org/10.5194/acp-20-13023-2020), 2020c.

492 Liu, Z., Wang, Y., Costabile, F., Amoroso, A., Zhao, C., Huey, L. G., Stickel, R., Liao,  
493 J., and Zhu, T.: Evidence of aerosols as a media for rapid daytime HONO  
494 production over China, *Environ. Sci. Technol.*, 48, 13023–13040,  
495 <https://doi.org/10.1021/es504163z>, 2014.

496 Lu, K., Guo, S., Tan, Z., Wang, H., Shang, D., Liu, Y., Li, X., Wu, Z., Hu, M., and  
497 Zhang, Y.: Exploring atmospheric free-radical chemistry in China: the self-  
498 cleansing capacity and the formation of secondary air pollution, *Natl. Sci. Rev.*, 6,

499 [579-594, https://doi.org/10.1093/nsr/nwy073](https://doi.org/10.1093/nsr/nwy073), 2018.

500 Luo, L., Bai, X., Lv, Y., Liu, S., Guo, Z., Liu, W., Hao, Y., Sun, Y., Hao, J., Zhang, K.,  
501 Zhao, H., Lin, S., Zhao, S., Xiao, Y., Yang, J., and Tian, H.: Exploring the driving  
502 factors of haze events in Beijing during Chinese New Year holidays in 2020 and  
503 2021 under the influence of COVID-19 pandemic, *Sci. Total Environ.*, 859,  
504 160172, <https://doi.org/10.1016/j.scitotenv.2022.160172>, 2023.

505 Ma, S.: High-resolution assessment of ammonia emissions in China: Inventories,  
506 driving forces and mitigation, *Atmos. Environ.*, 229,  
507 <https://doi.org/10.1016/j.atmosenv.2020.117458>, 2020.

508 McFall, A. S., Edwards, K. C., and Anastasio, C.: Nitrate photochemistry at the air-ice  
509 interface and in other ice reservoirs, *Environ. Sci. Technol.*, 52, 5710–5717,  
510 <https://doi.org/10.1021/acs.est.8b00095>, 2018.

511 Meng, Z., Xu, X., Lin, W., Ge, B., Xie, Y., Song, B., Jia, S., Zhang, R., Peng, W., Wang,  
512 Y., Cheng, H., Yang, W., and Zhao, H.: Role of ambient ammonia in particulate  
513 ammonium formation at a rural site in the North China Plain, *Atmos. Chem. Phys.*,  
514 18, 167–184, <https://doi.org/10.5194/acp-18-167-2018>, 2018.

515 Meusel, H., Tamm, A., Kuhn, U., Wu, D., Leifke, A. L., Fiedler, S., Ruckteschler, N.,  
516 Yordanova, P., Lang-Yona, N., Pöhlker, M., Lelieveld, J., Hoffmann, T., Pöschl,  
517 U., Su, H., Weber, B., and Cheng, Y.: Emission of nitrous acid from soil and  
518 biological soil crusts represents an important source of HONO in the remote  
519 atmosphere in Cyprus, *Atmos. Chem. Phys.*, 18, 799 – 813,  
520 <https://doi.org/10.5194/acp-18-799-2018>, 2018.

521 Oswald, R., Behrendt, T., Ermel, M., Wu, D., Su, H., Cheng, Y., Breuninger, C.,  
522 Moravek, A., Mougín, E., Delon, C., Loubet, B., Pommerening-Roser, A., Sorgel,

523 M., Poschl, U., and Hoffmann, T., Andreae, M.O., Meixner, F.X., Trebs, I.: HONO  
524 emissions from soil bacteria as a major source of atmospheric reactive nitrogen.,  
525 Science. 341, 1233–1235, <https://www.science.org/doi/10.1126/science.1242266>,  
526 2013.

527 Pagsberg, P., Bjergbakke, E., Ratajczak, E., Sillesen, A.: Kinetics of the gas phase  
528 reaction  $\text{OH} + \text{NO} (+\text{M}) \rightarrow \text{HONO} (+\text{M})$  and the determination of the UV  
529 absorption cross sections of HONO., Chem. Phys. Lett. 272, 383–390,  
530 [https://doi.org/10.1016/s0009-2614\(97\)00576-9](https://doi.org/10.1016/s0009-2614(97)00576-9), 1997.

531 Platt, U., Perner, D., Harris, G. W., Winer, A. M., and Pitts, J. N.: Observations of  
532 nitrous acid in an urban atmosphere by differential optical absorption, Nature, 285,  
533 312–314, <https://doi.org/10.1038/285312a0>, 1980.

534 Romer, P. S., Wooldridge, P. J., Crouse, J. D., Kim, M. J., Wennberg, P. O., Dibb, J.  
535 E., Scheuer, E., Blake, D. R., Meinardi, S., Brosius, A. L., Thames, A. B., Miller,  
536 D. O., Brune, W. H., Hall, S. R., Ryerson, T. B., and Cohen, R. C.: Constraints on  
537 aerosol nitrate photolysis as a potential source of HONO and  $\text{NO}_x$ . Environ. Sci.  
538 Technol. 52, 13738–13746, <https://doi.org/10.1021/acs.est.8b03861>, 2018.

539 Scharko, N. K., Berke, A. E., and Raff, J. D.: Release of nitrous acid and nitrogen  
540 dioxide from nitrate photolysis in acidic aqueous solutions, Environ. Sci. Technol.,  
541 48, 11991–12001, <https://doi.org/10.1021/es503088x>, 2014.

542 Shi, Q., Tao, Y., Krechmer, J. E., Heald, C. L., Murphy, J. G., Kroll, J. H., and Ye, Q.:  
543 Laboratory investigation of renoxification from the photolysis of inorganic  
544 particulate nitrate, Environ. Sci. Technol., 55, 854–861,

545 <https://doi.org/10.1021/acs.est.0c06049>, 2021.

546 Song, S., Gao, M., Xu, W., Shao, J., Shi, G., Wang, S., Wang, Y., Sun, Y., and McElroy,  
547 M. B.: Fine-particle pH for Beijing winter haze as inferred from different  
548 thermodynamic equilibrium models, *Atmos. Chem. Phys.*, 18, 7423–7438,  
549 <https://doi.org/10.5194/acp-18-7423-2018>, 2018.

550 Song, S., Nenes, A., Gao, M., Zhang, Y., Liu, P., Shao, J., Ye, D., Xu, W., Lei, L., Sun,  
551 Y., Liu, B., Wang, S., and McElroy, M. B.: Thermodynamic modeling suggests  
552 declines in water uptake and acidity of inorganic aerosols in Beijing winter haze  
553 events during 2014/2015–2018/2019. *Environ. Sci. Technol. Lett.* 6, 752–760,  
554 <https://doi.org/10.1021/acs.estlett.9b00621>, 2019.

555 Spataro, F., and Ianniello, A.: Sources of atmospheric nitrous acid: state of the science,  
556 current research needs, and future prospects, *J. Air. Waste. Manag. Assoc.*, 64,  
557 1232–1250, <https://doi.org/10.1080/10962247.2014.952846>, 2014.

558 Stieger, B., Spindler, G., van Pinxteren, D., Grüner, A., Wallasch, M., and Herrmann,  
559 H.: Development of an online-coupled MARGA upgrade for the 2 h interval  
560 quantification of low-molecular-weight organic acids in the gas and particle phases,  
561 *Atmos. Meas. Tech.* 12, 281–298, <https://doi.org/10.5194/amt-12-281-2019>, 2019.

562 Su, H., Cheng, Y., Oswald, R., Behrendt, T., Trebs, I., Meixner, F.X., Andreae, M.O.,  
563 Cheng, P., and Zhang, Y., Poschl, U.: Soil nitrite as a source of atmospheric HONO  
564 and OH radicals., *Science*. 333, 1616–1618,  
565 <https://doi.org/10.1126/science.1207687>, 2011.

566 Twigg, M. M., Berkhout, A. J. C., Cowan, N., Crunaire, S., Dammers, E., Ebert, V.,

567 Gaudion, V., Haaima, M., Häni, C., John, L., Jones, M. R., Kamps, B., Kentisbeer,  
568 J., Kupper, T., Leeson, S. R., Leuenberger, D., Lüttschwager, N. O. B., Makkonen,  
569 U., Martin, N. A., Missler, D., Mounsor, D., Neftel, A., Nelson, C., Nemitz, E.,  
570 Oudwater, R., Pascale, C., Petit, J.-E., Pogany, A., Redon, N., Sintermann, J.,  
571 Stephens, A., Sutton, M. A., Tang, Y. S., Zijlmans, R., Braban, C. F., and  
572 Niederhauser, B.: Intercomparison of in situ measurements of ambient NH<sub>3</sub>:  
573 instrument performance and application under field conditions, *Atmos. Meas.*  
574 *Tech.* 15, 6755–6787, <https://doi.org/10.5194/amt-15-6755-2022>, 2022.

575 Wang, C., Yin, S., Bai, L., Zhang, X., Gu, X., Zhang, H., Lu, Q., and Zhang, R.: High-  
576 resolution ammonia emission inventories with comprehensive analysis and  
577 evaluation in Henan, China, 2006–2016, *Atmos. Environ.* 193, 11–23,  
578 <https://doi.org/10.1016/j.atmosenv.2018.08.063>, 2018.

579 Wang, S., Wang, L., Li, Y., Wang, C., Wang, W., Yin, S., and Zhang, R.: Effect of  
580 ammonia on fine-particle pH in agricultural regions of China: comparison between  
581 urban and rural sites, *Atmos. Chem. Phys.*, 20, 2719–2734,  
582 <https://doi.org/10.5194/acp-20-2719-2020>, 2020.

583 Wang, S., Wang, L., Fan, X., Wang, N., Ma, S., and Zhang, R.: Formation pathway of  
584 secondary inorganic aerosol and its influencing factors in Northern China:  
585 Comparison between urban and rural sites, *Sci. Total Environ.*, 840,  
586 <https://doi.org/10.1016/j.scitotenv.2022.156404>, 2022.

587 Wang, S., Fan, X., Xu, Y., Zhang, R., and Ren, B.: Insight into the non-linear responses  
588 of particulate sulfate to reduced SO<sub>2</sub> concentration: A perspective from the

589 aqueous-phase reactions in a megacity in Northern China, *Atmos. Res.*, 290,  
590 <https://doi.org/10.1016/j.atmosres.2023.106796>, 2023a.

591 Wang, W., Wang, S., Xu, J., Zhou, R., Shi, C., and Zhou, B.: Gas-phase ammonia and  
592 PM<sub>2.5</sub> ammonium in a busy traffic area of Nanjing, China, *Environ. Sci. Pollut.*  
593 *Res. Int.*, 23, 1691–1702, <https://doi.org/10.1007/s11356-015-5397-3>, 2016.

594 Wang, Y., Jin, X., Liu, Z., Wang, G., Tang, G., Lu, K., Hu, B., Wang, S., Li, G., An, X.,  
595 Wang, C., Hu, Q., He, L., Zhang, F., and Zhang, Y.: Progress in quantitative  
596 research on the relationship between atmospheric oxidation and air quality, *J.*  
597 *Environ. Sci.*, 123, 350–366, <https://doi.org/10.1016/j.jes.2022.06.029>, 2023b.

598 Wells, M., Choulaton, T. W., and Bower, K. N.: A modelling study of the interaction  
599 of ammonia with cloud., *Atmos. Environ.*, 32, 359–363,  
600 [https://doi.org/10.1016/s1352-2310\(97\)00199-4](https://doi.org/10.1016/s1352-2310(97)00199-4), 1998.

601 Wentworth, G. R., Murphy, J. G., Benedict, K. B., Bangs, E. J., and Collett Jr, J. L.: The  
602 role of dew as a night-time reservoir and morning source for atmospheric ammonia,  
603 *Atmos. Chem. Phys.* 16, 7435–7449, <https://doi.org/10.5194/acp-16-7435-2016>,  
604 2016.

605 Wu, C., Lv, S., Wang, F., Liu, X., Li, J., Liu, L., Zhang, S., Du, W., Liu, S., Zhang, F.,  
606 Li, J., Meng, J., and Wang, G.: Ammonia in urban atmosphere can be substantially  
607 reduced by vehicle emission control: A case study in Shanghai, China, *J. Environ.*  
608 *Sci.*, 126, 754–760, <https://doi.org/10.1016/j.jes.2022.04.043>, 2023.

609 Xie, Y., Wang, G., Wang, X., Chen, J., Chen, Y., Tang, G., Wang, L., Ge, S., Xue, G.,  
610 Wang, Y., and Gao, J.: Nitrate-dominated PM<sub>2.5</sub> and elevation of particle pH

611 observed in urban Beijing during the winter of 2017. *Atmos. Chem. Phys.* 20,  
612 5019–5033, <https://doi.org/10.5194/acp-20-5019-2020>, 2020.

613 Xing, L., Fu, T. M., Cao, J. J., Lee, S. C., Wang, G. H., Ho, K. F., Cheng, M. C., You,  
614 C. F., and Wang, T. J.: Seasonal and spatial variability of the OM/OC mass ratios  
615 and high regional correlation between oxalic acid and zinc in Chinese urban  
616 organic aerosols, *Atmos. Chem. Phys.*, 13, 4307–4318,  
617 <https://doi.org/10.5194/acp-13-4307-2013>, 2013.

618 Xu, J., Chen, J., Zhao, N., Wang, G., Yu, G., Li, H., Huo, J., Lin, Y., Fu, Q., Guo, H.,  
619 Deng, C., Lee, S.-H., Chen, J., and Huang, K.: Importance of gas-particle  
620 partitioning of ammonia in haze formation in the rural agricultural environment,  
621 *Atmos. Chem. Phys.* 20, 7259–7269, <https://doi.org/10.5194/acp-20-7259-2020>,  
622 2020.

623 Xu, W., Kuang, Y., Zhao, C., Tao, J., Zhao, G., Bian, Y., Yang, W., Yu, Y., Shen, C.,  
624 Liang, L., Zhang, G., Lin, W., and Xu, X.: NH<sub>3</sub>-promoted hydrolysis of NO<sub>2</sub>  
625 induces explosive growth in HONO, *Atmos. Chem. Phys.* 19, 10557–10570,  
626 <https://doi.org/10.5194/acp-19-10557-2019>, 2019.

627 Xu, W., Zhao, Y., Wen, Z., Chang, Y., Pan, Y., Sun, Y., Ma, X., Sha, Z., Li, Z., Kang, J.,  
628 Liu, L., Tang, A., Wang, K., Zhang, Y., Guo, Y., Zhang, L., Sheng, L., Zhang, X.,  
629 Gu, B., Song, Y., Van Damme, M., Clarisse, L., Coheur, P. F., Collett, J. L., Jr.,  
630 Goulding, K., Zhang, F., He, K., and Liu, X.: Increasing importance of ammonia  
631 emission abatement in PM<sub>2.5</sub> pollution control. *Sci. Bull.* 67, 1745–1749,  
632 <https://doi.org/10.1016/j.scib.2022.07.021>, 2022.



633 Xue, C.: Substantially growing interest in the chemistry of nitrous acid (HONO) in  
634 China: current achievements, problems, and future directions. *Environ. Sci.*  
635 *Technol.* 56, 7375–7377. <https://doi.org/10.1021/acs.est.2c02237>, 2022.

636 Ye, C., Zhang, N., Gao, H., and Zhou, X.: Photolysis of particulate nitrate as a source  
637 of HONO and NO<sub>x</sub>. *Environ. Sci. Technol.* 51, 6849–6856,  
638 <https://doi.org/10.1021/acs.est.7b00387>, 2017.

639 Ye, X., Ma, Z., Zhang, J., Du, H., Chen, J., Chen, H., Yang, X., Gao, W., and Geng, F.:  
640 Important role of ammonia on haze formation in Shanghai, *Environ. Res. Lett.* 6,  
641 024019, <https://doi.org/10.1088/1748-9326/6/2/024019>, 2011.

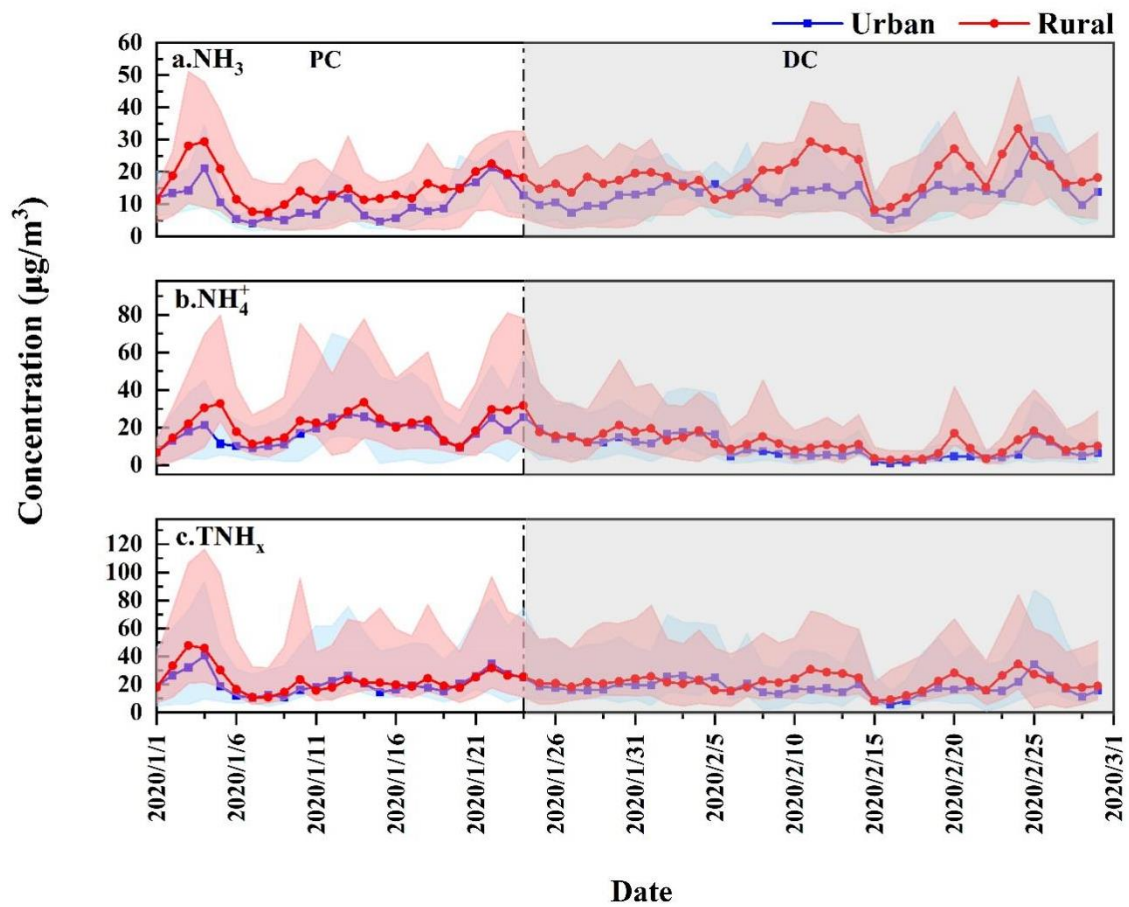
642 Zhang, W., Tong, S., Jia, C., Wang, L., Liu, B., Tang, G., Ji, D., Hu, B., Liu, Z., Li, W.,  
643 Wang, Z., Liu, Y., Wang, Y., and Ge, M.: Different HONO sources for three layers  
644 at the urban area of Beijing. *Environ. Sci. Technol.* 54, 12870–12880,  
645 <https://doi.org/10.1021/acs.est.0c02146>, 2020a.

646 Zhang, W., Tong, S., Jia, C., Ge, M., Ji, D., Zhang, C., Liu, P., Zhao, X., Mu, Y., Hu, B.,  
647 Wang, L., Tang, G., Li, X., Li, W., and Wang, Z.: Effect of different combustion  
648 processes on atmospheric nitrous acid formation mechanisms: a winter  
649 comparative observation in urban, suburban and rural areas of the North China  
650 Plain. *Environ. Sci. Technol.* 56, 4828–4837,  
651 <https://doi.org/10.1021/acs.est.1c07784>, 2022.

652 Zhang, Y., Liu, X., Fang, Y., Liu, D., Tang, A., and Collett, J. L.: Atmospheric ammonia  
653 in Beijing during the COVID-19 outbreak: concentrations, sources, and  
654 implications. *Environ. Sci. Technol. Lett.* 8, 32–38,



656 **Figures:**

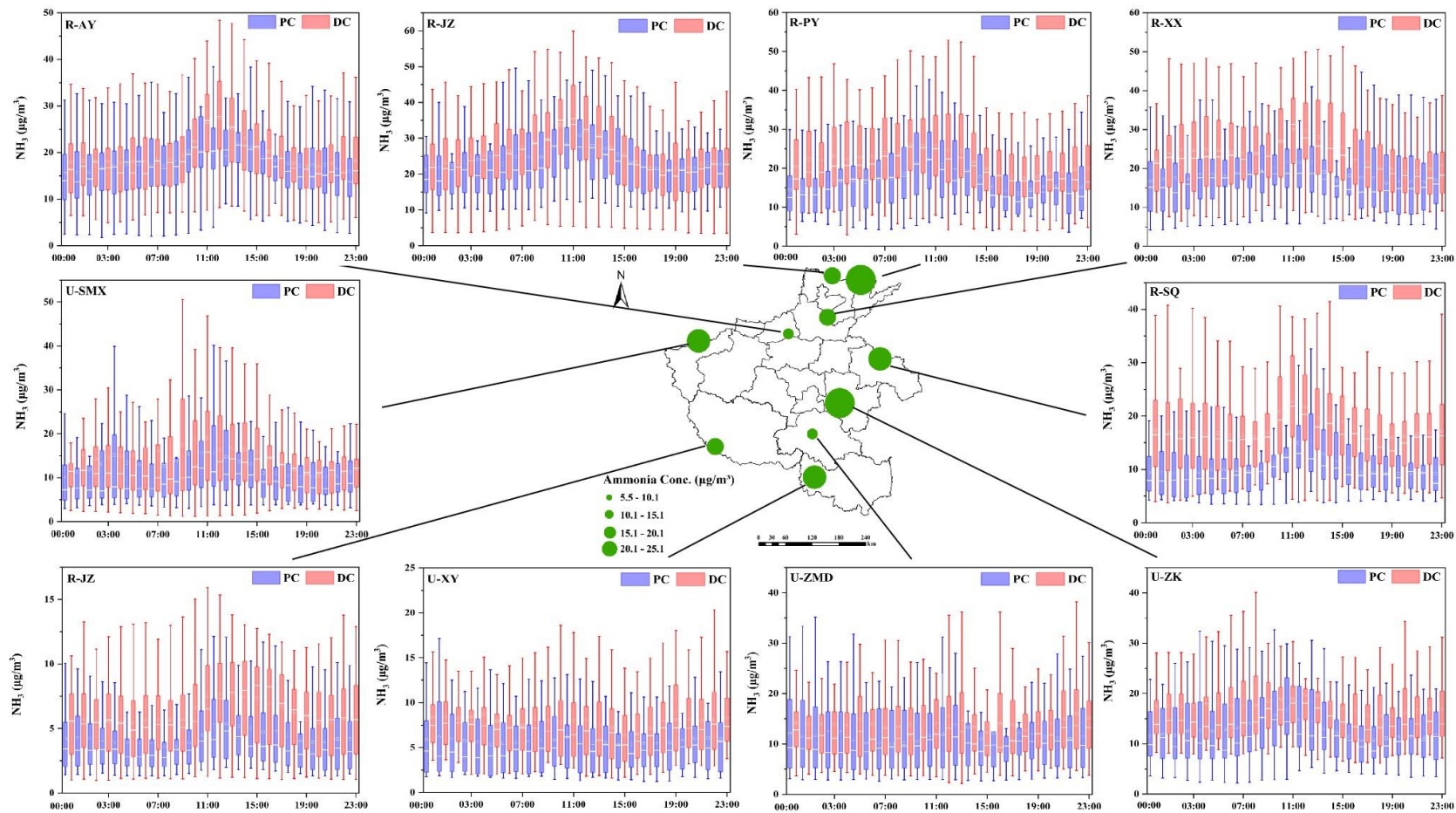


657

658 Figure 1. Temporal variations of a. NH<sub>3</sub>, b. NH<sub>4</sub><sup>+</sup>, and c. TNH<sub>x</sub> at the urban and rural

659 sites before (PC) and during (DC) the COVID-19 outbreak, respectively. The shaded

660 areas of the curve represent the maximum and minimum values.



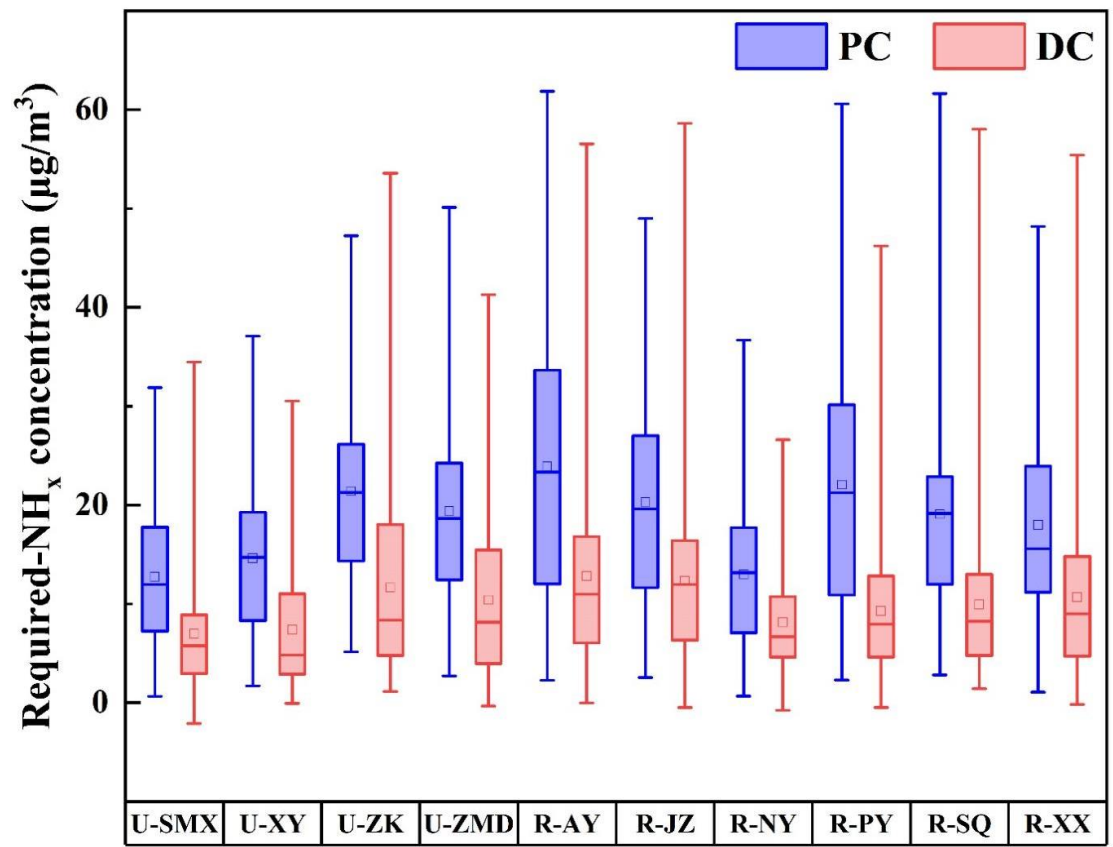
661

662

663

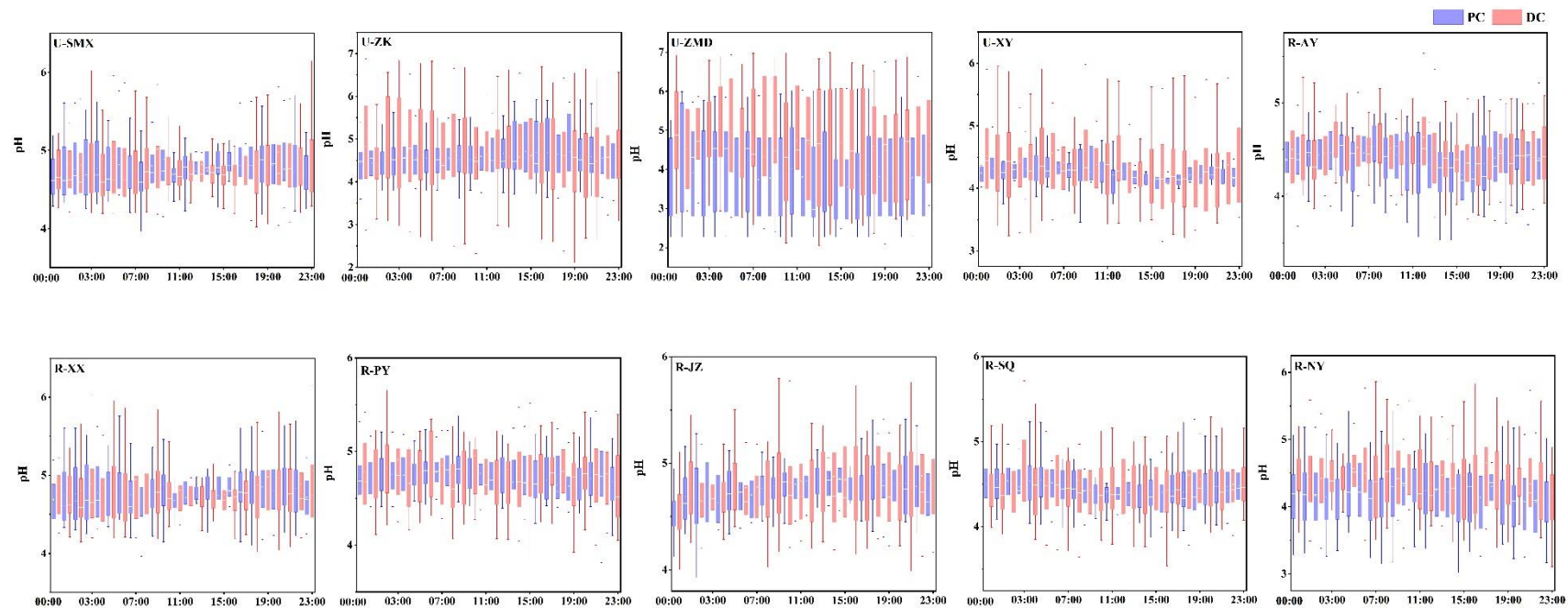
664

Figure 2. Daily variation of  $\text{NH}_3$  concentrations at ten sites before (PC) and during (DC) the COVID-19 outbreak. The green dots represent the location of ten sites and their size represents the concentration of  $\text{NH}_3$ ; In each box, the top, middle, and bottom lines represent the 75, 50, and 25 percentiles of statistical data, respectively; the upper and lower whiskers represent the 90 and 10 percentiles of statistical data, respectively.



665

666 Figure 3. Box diagram of changes in Required-NH<sub>x</sub> at ten sites before (PC) and during  
 667 (DC) the COVID-19 outbreak. In each box, the top, middle, and bottom lines represent  
 668 the 75, 50, and 25 percentiles of statistical data, respectively; the upper and lower  
 669 whiskers represent the 90 and 10 percentiles of statistical data, respectively.



670

671

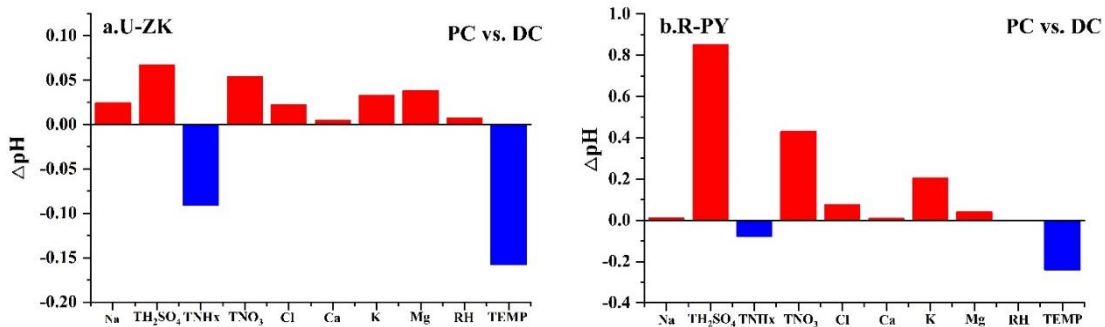
Figure 4. Diurnal patterns of pH at ten sites before (PC) and during (DC) the COVID-19 outbreak. In each box, the top, middle, and bottom

672

lines represent the 75, 50, and 25 percentiles of statistical data, respectively; the upper and lower whiskers represent the 90 and 10 percentiles of

673

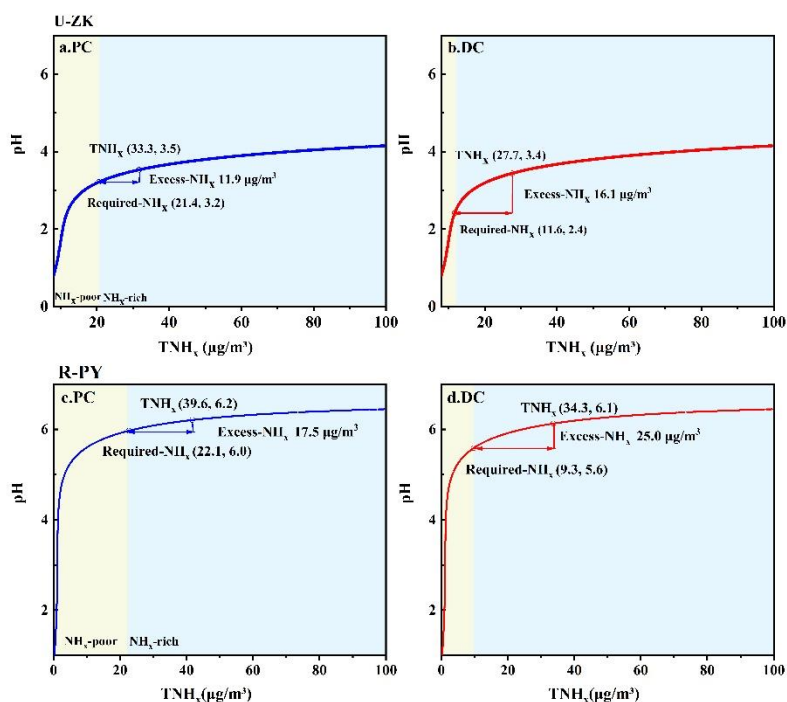
statistical data, respectively.



674

675 Figure 5. Changes of pH ( $\Delta\text{pH}$ ) through the sensitivity tests (Figure S5 and S6) by

676 changing parameters between PC and DC at the a. U-ZK and b. R-PY sites.



677

678 Figure 6. Particle pH corresponds to increasing  $\text{TNH}_x$  at U-ZK and R-PY sites to

679 examine the effects of major indicators of  $\text{NH}_3$  (i.e.,  $\text{TNH}_x$ , Required- $\text{NH}_x$ , and Excess-

680  $\text{NH}_x$ ) on aerosol acidity. Particle pH was calculated by using a wide range of  $\text{TNH}_x$

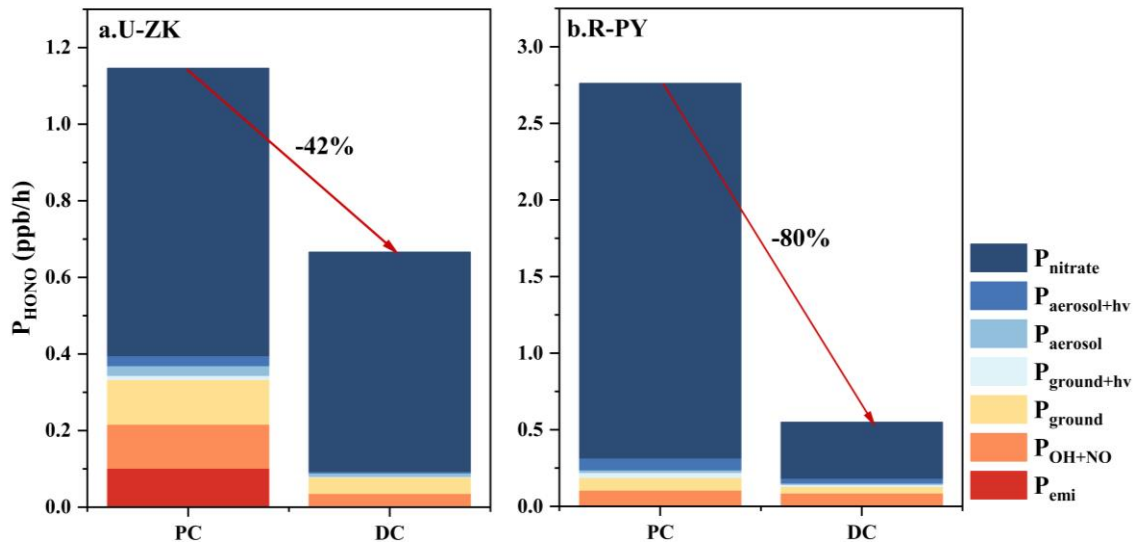
681 ( $25\text{--}130\ \mu\text{g}/\text{m}^3$ ) and average values of other parameters in PC and DC of U-ZK and R-

682 PY sites. The concentrations of  $\text{TNH}_x$ , Required- $\text{NH}_x$ , and Excess- $\text{NH}_x$  with

683 corresponding pH values are marked by a hollow box, hollow circle, and arrow

684 respectively. The yellow and blue background colors correspond to the  $\text{NH}_x$ -poor and

685  $\text{NH}_x$ -rich, respectively.

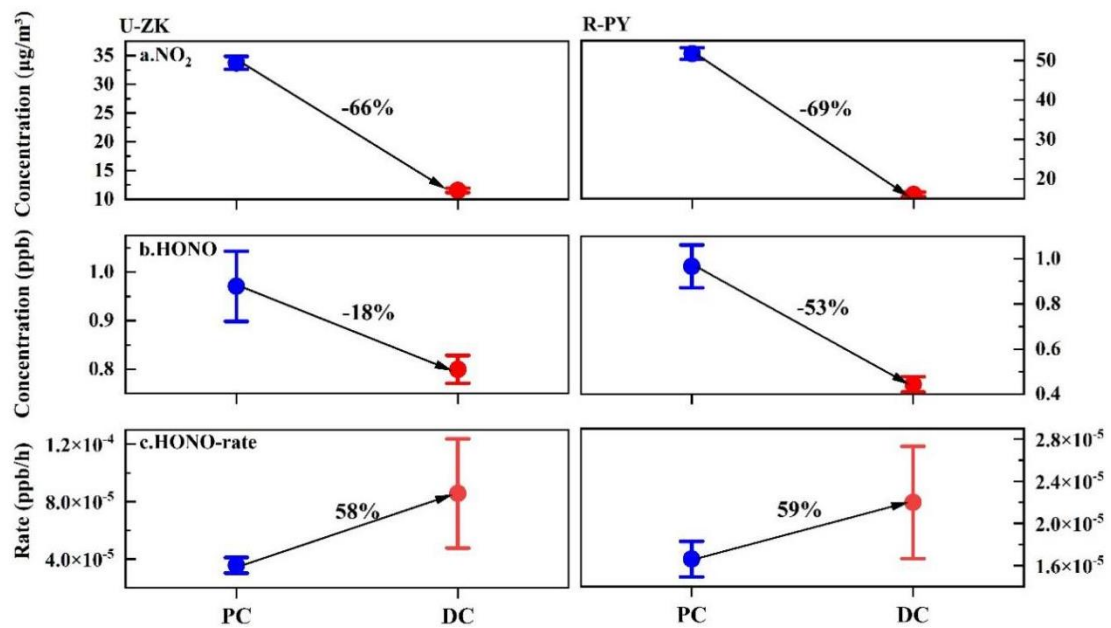


686

687 Figure 7. Comparison of HONO sources at a. U-ZK and b. R-PY sites before (PC) and

688 during (DC) the COVID-19 outbreak. The calculation method can be found in Text S4.

689



690

691 Figure 8. Decline ratios of a.  $\text{NO}_2$ , b. HONO concentration, and c. HONO production

692 rate at U-ZK and R-PY sites before (PC) and during (DC) the COVID-19 outbreak. The

693 center point represents the mean value, and the upper and lower whiskers represent the

694 95% confidence interval of the mean.



695 **Table:**

696 Table 1. Changes in concentrations (mean  $\pm$  standard deviation) of NH<sub>3</sub>, NH<sub>4</sub><sup>+</sup>, and  
 697 TNH<sub>x</sub> at ten sites during entire periods (Average), before (PC), and during (DC) the  
 698 COVID-19 outbreak.

Sites	Substances	Average ( $\mu\text{g}/\text{m}^3$ )	PC ( $\mu\text{g}/\text{m}^3$ )	DC ( $\mu\text{g}/\text{m}^3$ )
U-SMX	NH <sub>3</sub>	13.8 $\pm$ 10.8	12.6 $\pm$ 10.1	14.5 $\pm$ 11.1
	NH <sub>4</sub> <sup>+</sup>	10.9 $\pm$ 7.2	14.2 $\pm$ 7.2	8.8 $\pm$ 6.5
	TNH <sub>x</sub>	22.9 $\pm$ 14.1	24.9 $\pm$ 14.5	21.7 $\pm$ 13.8
U-ZK	NH <sub>3</sub>	15.6 $\pm$ 8.3	12.7 $\pm$ 6.5	17.4 $\pm$ 8.8
	NH <sub>4</sub> <sup>+</sup>	13.6 $\pm$ 9.3	19.1 $\pm$ 8.4	10.3 $\pm$ 8.1
	TNH <sub>x</sub>	28.6 $\pm$ 13.7	30.9 $\pm$ 12.8	27.1 $\pm$ 14.0
U-ZMD	NH <sub>3</sub>	13.1 $\pm$ 8.4	11.6 $\pm$ 8.2	14.0 $\pm$ 8.4
	NH <sub>4</sub> <sup>+</sup>	13.9 $\pm$ 9.8	19.6 $\pm$ 10.3	10.3 $\pm$ 7.5
	TNH <sub>x</sub>	25.7 $\pm$ 14.6	30.3 $\pm$ 15.1	22.8 $\pm$ 13.5
U-XY	NH <sub>3</sub>	7.0 $\pm$ 4.3	5.7 $\pm$ 4.0	7.9 $\pm$ 4.3
	NH <sub>4</sub> <sup>+</sup>	11.0 $\pm$ 7.7	15.4 $\pm$ 7.6	8.3 $\pm$ 6.5
	TNH <sub>x</sub>	17.6 $\pm$ 9.8	20.6 $\pm$ 10.1	15.7 $\pm$ 9.2
R-AY	NH <sub>3</sub>	19.0 $\pm$ 8.4	17.9 $\pm$ 8.3	19.7 $\pm$ 8.4
	NH <sub>4</sub> <sup>+</sup>	19.3 $\pm$ 12.9	26.4 $\pm$ 13.7	15.0 $\pm$ 10.3
	TNH <sub>x</sub>	36.6 $\pm$ 18.2	41.7 $\pm$ 20.4	33.4 $\pm$ 16.0
R-XX	NH <sub>3</sub>	21.7 $\pm$ 10.2	18.1 $\pm$ 9.3	23.8 $\pm$ 10.1
	NH <sub>4</sub> <sup>+</sup>	15.9 $\pm$ 10.4	20.6 $\pm$ 11.0	13.0 $\pm$ 8.8
	TNH <sub>x</sub>	34.9 $\pm$ 17.0	35.1 $\pm$ 18.8	34.8 $\pm$ 15.8
R-PY	NH <sub>3</sub>	19.8 $\pm$ 9.4	16.8 $\pm$ 8.1	21.7 $\pm$ 9.6
	NH <sub>4</sub> <sup>+</sup>	17.4 $\pm$ 11.8	25.3 $\pm$ 12.6	12.4 $\pm$ 8.0
	TNH <sub>x</sub>	35.2 $\pm$ 17.8	39.4 $\pm$ 19.8	32.6 $\pm$ 15.7
R-JZ	NH <sub>3</sub>	25.3 $\pm$ 11.5	24.1 $\pm$ 11.5	25.9 $\pm$ 11.4
	NH <sub>4</sub> <sup>+</sup>	17.3 $\pm$ 11.3	22.7 $\pm$ 11.6	14.2 $\pm$ 9.9
	TNH <sub>x</sub>	40.8 $\pm$ 20.1	42.9 $\pm$ 22.8	33.5 $\pm$ 18.2
R-SQ	NH <sub>3</sub>	15.0 $\pm$ 7.9	10.3 $\pm$ 5.2	17.7 $\pm$ 7.9
	NH <sub>4</sub> <sup>+</sup>	13.4 $\pm$ 8.5	18.9 $\pm$ 8.6	10.3 $\pm$ 6.7
	TNH <sub>x</sub>	26.3 $\pm$ 13.2	25.5 $\pm$ 14.0	26.8 $\pm$ 12.7
R-NY	NH <sub>3</sub>	5.5 $\pm$ 3.1	4.3 $\pm$ 2.7	6.2 $\pm$ 3.2
	NH <sub>4</sub> <sup>+</sup>	10.2 $\pm$ 6.9	13.3 $\pm$ 7.2	8.4 $\pm$ 6.1
	TNH <sub>x</sub>	14.8 $\pm$ 8.5	16.0 $\pm$ 9.5	14.1 $\pm$ 7.8

699

## 1 **Supplement materials:**

### 2 **Text S1 Detailed description of the aerosol and gas monitor.**

3 The aerosol and gas monitor (MARGA, Metrohm, Switzerland) was used to analyze  
4 the hourly water-soluble ions ( $\text{Na}^+$ ,  $\text{NH}_4^+$ ,  $\text{K}^+$ ,  $\text{Mg}^{2+}$ ,  $\text{Ca}^{2+}$ ,  $\text{Cl}^-$ ,  $\text{NO}_3^-$ , and  $\text{SO}_4^{2-}$ ) in  
5  $\text{PM}_{2.5}$ , as well as gaseous species ( $\text{NH}_3$ ,  $\text{HNO}_3$ ,  $\text{HCl}$ , and  $\text{HONO}$ ) at ten sampling sites.  
6 The atmospheric sample passes through a  $\text{PM}_{2.5}$  cut-off head, and both particles and  
7 gases enter a wet rotating dissolution device for diffusion. Subsequently, the particles  
8 in the sample undergo hygroscopic growth and condensation in an aerosol  
9 supersaturated vapor generator, followed by collection and ion chromatographic  
10 analysis. The gases in the sample are oxidized by  $\text{H}_2\text{O}_2$  in the dissolution device,  
11 absorbed into a liquid solvent, and then entered the gas sample collection chamber for  
12 ion chromatographic quantification. During this process, the sample is extracted  
13 through a liquid diffusion filter, where interfering acidic and alkaline gases are removed.  
14 To achieve high collection efficiency, the airflow containing loaded ions then enters an  
15 aerosol supersaturated collector until the particles can be injected into the ion  
16 chromatograph. The ion chromatography system utilizes either suppressor or non-  
17 suppressor conductivity detection methods for ion analysis. Before running the samples,  
18 the ion chromatograph system needs to be calibrated using standard solutions. By  
19 comparing the data obtained from the sample with the data obtained from known  
20 standard solutions, the identification and quantification of sample ions can be

21 performed. The data acquisition system generates chromatograms, and the  
22 chromatography software further converts each peak in the chromatogram into sample  
23 concentrations and outputs the results.

#### 24 **QA/QC**

25 The instrument underwent daily checks and maintenance, which typically involved  
26 ensuring the stability of the internal standard response and maintaining a relative error  
27 within  $\pm 10\%$  between the measured and theoretical concentrations of the internal  
28 standard. The system's data acquisition and transmission were carefully examined,  
29 along with monitoring the instrument's status information and collected data. This  
30 included checking parameters such as sampling flow rate, chromatographic column  
31 pressure, column temperature, conductivity, target compound peak retention time, and  
32 peak width to ensure their normal functioning. Regular replacement of consumables  
33 used by the instrument was carried out at predetermined intervals and frequencies.  
34 Additionally, standard curve measurements and calibration were performed in each  
35 season to guarantee the accuracy of the instrument's data. Calibration curve verification  
36 was performed at least once per quarter. A standard series containing at least 6  
37 calibration points, including zero concentration, was prepared using standard solutions.  
38 The concentration range of the calibration curve was set according to the actual  
39 environmental concentration levels and determined by manual injection. The obtained  
40 calibration curve had a linear correlation coefficient ( $r$ ) of  $\geq 0.995$ . If this requirement  
41 was not met, the rationality of the internal standard solution concentration settings

42 would be checked. When key components such as the quantitative loop,  
43 chromatographic column, or suppressor are replaced, a new calibration curve will be  
44 promptly established. After establishing the new calibration curve, the sample sequence  
45 in the analysis software would be updated. The minimum detection limit was  
46 determined as follows:  $0.002 \mu\text{g}/\text{m}^3$  ( $\text{Cl}^-$ ),  $0.081 \mu\text{g}/\text{m}^3$  ( $\text{NH}_4^+$ ),  $0.02 \mu\text{g}/\text{m}^3$  ( $\text{NO}_3^-$ ),  $0.06$   
47  $\mu\text{g}/\text{m}^3$  ( $\text{SO}_4^{2-}$ ),  $0.002 \mu\text{g}/\text{m}^3$  ( $\text{Na}^+$ ),  $0.08 \mu\text{g}/\text{m}^3$  ( $\text{K}^+$ ),  $0.06 \mu\text{g}/\text{m}^3$  ( $\text{Ca}^{2+}$ ) and  $0.007 \mu\text{g}/\text{m}^3$   
48 ( $\text{Mg}^{2+}$ ). According to the research about the uncertainties in MARGA measurements,  
49 such as a 20% uncertainty for MARGA measurements (Song et al., 2018), an error of  
50 10% for detecting  $\text{SO}_4^{2-}$ ,  $\text{NO}_3^-$ , and  $\text{HNO}_3$ , and 15% for  $\text{NH}_3$  and  $\text{NH}_4^+$  (Rumsey et al.,  
51 2014), we set the uncertainties of 20% for  $\text{NH}_3$  and  $\text{NH}_4^+$ , 10% for other components.  
52 Due to the complex conditions encountered during the actual sampling process,  
53 including variations in calibration slopes, sampling volumes, solvent concentrations,  
54 temperature, atmospheric pressure, and sampling flow rates at different sampling points,  
55 the assumed values mentioned above may not accurately reflect the actual situation.

## 56 **Text S2 HONO measurement**

57 The HONO monitoring method adopted in MARGA is the wet-flow diffusion tube  
58 method (WEDD) in the diffusion tube method (Zellweger, 1999; Takeuchi et al, 2013),  
59 which is a common method for measuring HONO in wet chemistry and has high  
60 absorption efficiency. The device adopts a vertical setting, through the diffusion tube,  
61 the air in the atmosphere is pulled upward from the bottom, and the absorbent liquid is  
62 transported to the top of the diffusion tube through the air pump. When flowing under  
63 the action of gravity, a thin absorbent liquid film will be generated on the inner surface  
64 of the tube by the tension. The absorbent liquid film will absorb HONO, and the  
65 solution at the bottom of the diffusion tube will be sucked out through the air pump.  
66 Then it is sent to the ion chromatography for analysis. The integration time of the  
67 sample mainly depends on the running time of the ion chromatography, which is about  
68 5-30 min (Zellweger, 1999; Takeuchi et al, 2013). Based on the original, some scholars  
69 developed the flow injection-chemiluminescence method and used it together with  
70 WEDD for the measurement of HONO. The detection limit is about  $0.03 \mu\text{g}/\text{m}^3$   
71 (Mikuska et al., 2008; Zhao et al., 2010). In addition, HONO observations measured  
72 with this AIM-IC system agree well with HONO observations measured with the other  
73 systems (VandenBoer et al., 2014). Therefore, it is feasible to measure HONO using  
74 this instrument.

75 **Text S3 Detailed description of the NO<sub>2</sub>, SO<sub>2</sub> and carbon analyzer.**

76 The NO<sub>2</sub> analyzer utilized the chemiluminescence technique to measure the  
77 concentration of NO<sub>2</sub> in the air. This involved converting NO<sub>2</sub> to NO using a  
78 molybdenum converter, and then quantifying the NO concentration. The principle  
79 behind the SO<sub>2</sub> analyzer involved measuring the amount of ultraviolet light emitted  
80 during the decay of high-energy state SO<sub>2</sub>. This emitted light was used to calculate the  
81 concentration of SO<sub>2</sub>.

82 The carbon analyzer principle is primarily based on the NIOSH-5040 method, which  
83 involves analyzing the thermal optical transmittance of quartz filter samples. It employs  
84 a calibrated non-dispersive infrared sensor to detect the evolving carbon. Under  
85 controlled conditions with inert helium gas, carbon formed during a gradually  
86 increasing temperature gradient is referred to as OC, while carbon evolved under a  
87 mixture of 90% helium.

88 **Text S4 Sources of HONO**

89 **4.1 Direct emission**

90 HONO can be released directly into the atmosphere through vehicle exhaust  
91 (Burling et al., 2010; Veres et al., 2010). The lifetime of HONO in the atmosphere is  
92 relatively short, so vehicle emissions significantly contribute to urban atmospheric  
93 HONO (Chen et al., 2023; Liu et al., 2021a). Considering that there has been a

94 significant reduction in vehicle emissions in urban areas during DC. Additionally, the  
95 R-PY site is far from roads. Thus, vehicle emissions may not be the primary source of  
96 HONO for the U-ZK site during DC and R-PY sites during entire periods. To further  
97 validate the above conclusions, the conditional bivariate probability function diagrams  
98 of NO<sub>2</sub> at U-ZK and R-PY sites during PC and DC are depicted in Figure S2. NO<sub>2</sub>  
99 predominantly originated from long-distance transport at the U-ZK site during DC and  
100 the R-PY site during both PC and DC. Consequently, vehicle emissions are only  
101 calculated for the U-ZK site during the PC.

102 Here we use the HONO/NO<sub>x</sub> ratio to estimate HONO concentration, which is  
103 generally considered to be the vehicle emission factor (Kramer et al., 2020; Hao et al.,  
104 2020; Yu et al., 2022) for HONO. The calculation formula is as follows:

$$105 \quad [\text{HONO}_{\text{emi}}] = 0.8\% \times [\text{NO}_x] \quad (1)$$

106 where [HONO<sub>emi</sub>] and [NO<sub>x</sub>] represent the HONO concentration emitted by vehicles  
107 and the observed NO<sub>x</sub> concentration, respectively. Regarding previous studies (Table  
108 S3), 0.8% was selected as the vehicle emission factor, considering differences in vehicle  
109 type, fuel composition, and other factors (Kramer et al., 2020; Hao et al., 2020; Huang  
110 et al., 2017).

#### 111 4.2 Homogeneous reaction of NO and •OH

112 The reaction between NO and •OH is the primary gas-phase reaction source of  
113 HONO at high NO concentrations, and the production rate contribution (P<sub>OH+NO</sub>) for this

114 reaction can be calculated as:

$$115 \quad P_{\text{OH+NO}} = k_{\text{OH+NO}}[\text{OH}][\text{NO}] \quad (2)$$

116 where  $k_{\text{OH+NO}}$  ( $7.2 \times 10^{-12} \text{ cm}^3 \text{ molecule}^{-1} \text{ s}^{-1}$ ) is the rate constant for the reactions at  
117 298K (Li et al., 2012). •OH concentration was simulated according to the empirical  
118 model (Hu et al., 2022; Wang et al., 2025):

$$119 \quad [\text{OH}] = 4.1 \times 10^9 \times \frac{J(\text{O}^1\text{D}) \times J(\text{NO}_2) \times (140 \times [\text{NO}_2] + 1) + [\text{HONO}] \times J(\text{HONO})}{0.41 \times [\text{NO}_2]^2 + 1.7 \times [\text{NO}_2] + 1 + [\text{NO}] \times k_{\text{NO+OH}} + [\text{HONO}] \times k_{\text{NO+OH}}} \quad (3)$$

120 where,  $J(\text{O}^1\text{D})$ ,  $J(\text{NO}_2)$ , and  $J(\text{HONO})$  are the photolysis rates calculated using the  
121 TUV model (v5.2; available at <http://cprm.acom.ucar.edu/Models/TUV/>). The cloud  
122 optical depth value for the TUV model was adjusted so that the predicted UVB radiation  
123 intensity matched the observations (Lyu et al., 2019; Wang et al., 2022b). The calculated  
124 •OH concentration varied from  $0.1 \times 10^6$  to  $4 \times 10^6$  molecule/cm<sup>3</sup> at U-ZK and  $0.1 \times$   
125  $10^6$  to  $5 \times 10^6$  molecule/cm<sup>3</sup> at R-PY, which was comparable to the levels in other cities  
126 of North China (Li et al., 2018; Fuchs et al., 2017; Yang et al., 2017). Since there is no  
127 photolysis at night, the •OH concentration was assumed to be  $0.8 \times 10^6$  molecule/cm<sup>3</sup>  
128 (Wang et al., 2022).

## 129 4.3 Heterogeneous conversion of NO<sub>2</sub> to HONO

### 130 4.3.1 Heterogeneous dark reactions

131 The heterogeneous conversion of NO<sub>2</sub> to HONO on the ground ( $P_{\text{ground}}$ ) and on the  
132 aerosol surface ( $P_{\text{aerosol}}$ ) was calculated based on parameters obtained from experiments  
133 or observations.



134

$$P_{\text{ground}} = \frac{1}{8} \gamma_1 \times [\text{NO}_2] \times C_{\text{NO}_2} \times \frac{S_g}{V} \quad (4)$$

135

$$P_{\text{aerosol}} = \frac{1}{4} \gamma_2 \times [\text{NO}_2] \times C_{\text{NO}_2} \times \frac{S_a}{V} \quad (5)$$

136

$$\frac{S_g}{V} = \frac{1}{\text{MLH}} \quad (6)$$

137

$$C_{\text{NO}_2} = \sqrt{\frac{8RT}{\pi M}} \quad (7)$$

138 where  $C_{\text{NO}_2}$  is the average molecular velocity of  $\text{NO}_2$  molecule ( $\text{m s}^{-1}$ ); R is the ideal139 gas constant; T is the temperature (K); M is the molecular weight of  $\text{NO}_2$  ( $\text{kg mol}^{-1}$ );

140 MLH is the height of the mixed layer, which is determined to be 50 m due to HONO

141 formation on the ground level and its short lifetime (Liu et al., 2020b);  $S_a/V$  is the

142 surface area to volume ratio of aerosol, estimated by Su et al. (Su et al., 2008).

143 

### 4.3.2 Heterogeneous photo-enhanced reactions

144 The heterogeneous photo-enhanced reactions of  $\text{NO}_2$  on the surface of the ground145 ( $P_{\text{ground} + \text{hv}}$ ) and the surface of the aerosol ( $P_{\text{aerosol} + \text{hv}}$ ) were calculated following (Zhang

146 et al., 2020a):

147

$$P_{\text{ground} + \text{hv}} = \frac{1}{8} \times C_{\text{NO}_2} \times \frac{1}{\text{MLH}} \times \gamma_1 \times \frac{J_{\text{NO}_2}}{J_{\text{NO}_2, \text{noon}}} \times [\text{NO}_2] \quad (8)$$

148

$$P_{\text{aerosol} + \text{hv}} = \frac{1}{4} \times C_{\text{NO}_2} \times \frac{S_a}{V} \times \gamma_2 \times \frac{J_{\text{NO}_2}}{J_{\text{NO}_2, \text{noon}}} \times [\text{NO}_2] \quad (9)$$

149 where  $J_{\text{NO}_2}$  and  $J_{\text{NO}_2, \text{noon}}$  are the photolysis rate of  $\text{NO}_2$  and the photolysis rate of  $\text{NO}_2$ 

150 at noon during the day, respectively.

151  $\gamma_1$  and  $\gamma_2$  are the absorption coefficient of  $\text{NO}_2$  on the ground and aerosol surface,

152 respectively, which is assumed to be  $4 \times 10^{-6}$  (Yu et al., 2022; Zhang et al., 2021; Zhang  
153 et al., 2020a). Moreover, we discuss the uncertainties based on the recommended values  
154 of  $2 \times 10^{-6}$ – $1 \times 10^{-5}$  as upper and lower bounds (Chen et al., 2023; VandenBoer et al.,  
155 2013; Wong et al., 2011). Results show (Figure S3) that the uncertainties for  $P_{\text{ground}}$ ,  
156  $P_{\text{aerosol}}$ ,  $P_{\text{ground+hv}}$ , and  $P_{\text{aerosol+hv}}$  are  $-50\%$  to  $150\%$ ,  $-50\%$  to  $151\%$ ,  $-20\%$  to  $120\%$ , and  
157  $-50\%$  to  $121\%$  at the U-ZK, respectively. At the R-PY, the uncertainties for  $P_{\text{ground}}$ ,  
158  $P_{\text{aerosol}}$ ,  $P_{\text{ground+hv}}$ , and  $P_{\text{aerosol+hv}}$  are  $-50\%$  to  $150\%$ ,  $-50\%$  to  $151\%$ ,  $-20\%$  to  $120\%$ , and  
159  $-50\%$  to  $121\%$ , respectively.

#### 160 4.4 Nitrate photolysis

161 The nitrate photolysis ( $P_{\text{nitrate}}$ ) was calculated based on the measured nitrate  
162 concentration ( $\text{NO}_3^-$ ) from  $\text{PM}_{2.5}$  and nitrate photolysis rate ( $J_{\text{nitrate} \rightarrow \text{HONO}}$ ):

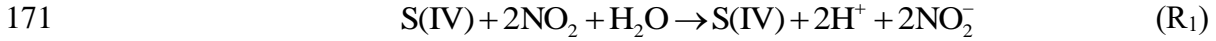
$$163 \quad P_{\text{nitrate}} = J_{\text{nitrate} \rightarrow \text{HONO}} \times [\text{NO}_3^-] \quad (10)$$

164 where the  $J_{\text{nitrate} \rightarrow \text{HONO}}$  was simulated by normalizing UV values, when the Zenit Angle  
165 is  $0^\circ$ ,  $J_{\text{nitrate} \rightarrow \text{HONO}}$  varied within the range of  $1.22 \times 10^{-5}$  to  $4.84 \times 10^{-4} \text{ s}^{-1}$ , with an average  
166 value of  $8.24 \times 10^{-5} \text{ s}^{-1}$  (Bao et al., 2018).

167

#### 168 **Text S5 Estimation of HONO formation rate**

169 The redox reaction of  $\text{NO}_2$  with  $\text{SO}_2$  ( $\text{R}_1$ ) is considered a crucial potential source of  
170 high concentrations of HONO in Northern China (Wang et al., 2016b; Cheng, 2016):



172 The rate expression for the reaction was estimated to:

173 
$$d[\text{S(VI)}]/dt = k_1[\text{NO}_2][\text{S(VI)}], \quad (11)$$

174 where the  $k_1 = (1.4 \times 10^5 + 1.24 \times 10^7)/2 \text{ M}^{-1}\text{s}^{-1}$  for the pH range  $< 5$ ;

175  $k_1 = (23.25 \times (\text{pH} - 5) + 1.4 + 124)/2 \times 10^5 \text{ M}^{-1}\text{s}^{-1}$  for the pH range  $5 < \text{pH} < 5.3$ ;

176  $k_1 = (23.25 \times (\text{pH} - 5) + 1.4 + 12.6 \times (\text{pH} - 5.3) + 124)/2 \times 10^5 \text{ M}^{-1}\text{s}^{-1}$  for the pH range  $5.3 <$

177  $\text{pH} < 5.8$ ;

178  $k_1 = (12.6 \times (\text{pH} - 5.3) + 124 + 20)/2 \times 10^5 \text{ M}^{-1}\text{s}^{-1}$  for the pH range  $5.8 < \text{pH} < 8.7$ ;

179 and  $k_1 = (2 \times 10^6 + 1.67 \times 10^7)/2 \text{ M}^{-1}\text{s}^{-1}$  for the pH range  $\text{pH} > 8.7$ . (Seinfeld et al., 1998)

180 In the above calculation formulas, the concentration of gas in the liquid is determined

181 by Henry's constant ( $H^*$ ). The calculation formula is in Table S4.  $\text{SO}_2$  has a dissociation

182 equilibrium in the solution, producing  $\text{HSO}_3^-$  and  $\text{SO}_3^{2-}$ . The ionization constants (K)

183 are shown in the following Table S5. The  $H^*$  and K are temperature-dependent. The

184 values are given in Tables S4 and S5 under the condition of 298K, converted to the

185 value under the actual temperature using the following calculation formula:

186 
$$H(T) \text{ or } K(T) = H(T_{298\text{K}}) \text{ or } K(T_{298\text{K}}) \exp \left[ -\frac{\Delta H_{298\text{K}}}{R} \left( \frac{1}{T} - \frac{1}{298\text{K}} \right) \right] \quad (12)$$

187 where  $H(T)$ 、 $K(T)$ 、 $H(T_{298\text{K}})$ 、and  $K(T_{298\text{K}})$  represent the  $H^*$  and K at actual

188 temperature and 298 K, respectively.

189 Influences of ionic strength on  $R_1$  were not considered because of the high values

190 predicted by the ISORROPIA-II model during the sampling periods (Cheng et al.,

191 2016). To evaluate the effects of mass transport, the formulation of a standard resistance

192 model was adopted:

$$193 \quad \frac{1}{R_{H, \text{aq}}} = \frac{1}{R_{\text{aq}}} + \frac{1}{J_{\text{aq}, \text{lim}}} \quad (13)$$

194 where  $R_{H, \text{aq}}$  is the sulfate production rate,  $R_{\text{aq}}$  is the aqueous-phase reaction rate and  
195  $J_{\text{aq}, \text{lim}}$  is the limiting mass transfer rate. which could be calculated by the formulas as  
196 follows:

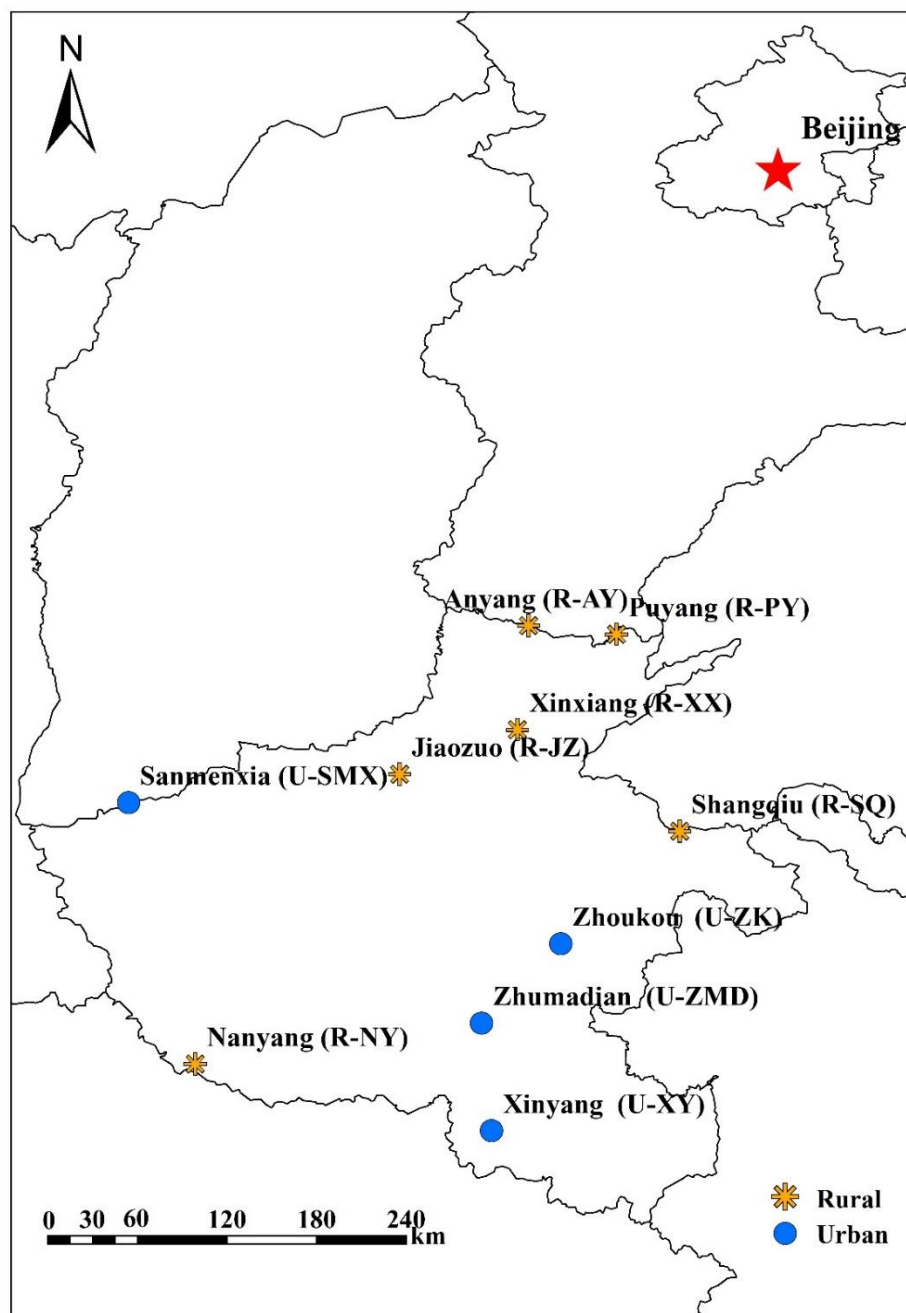
$$197 \quad J_{\text{aq}, \text{lim}} = \min\{J_{\text{aq}}(\text{SO}_2), J_{\text{aq}}(\text{X})\} \quad (14)$$

$$198 \quad J_{\text{aq}}(\text{X}) = k_{\text{MT}}(\text{X}) \cdot [\text{X}] \quad (15)$$

199 where  $[\text{X}]$  refers to the aqueous-phase concentrations of  $\text{SO}_2$  or the oxidants  $\text{O}_{\text{xi}}$   
200 calculated by the equation in Table S4. The mass transfer rate coefficient  $k_{\text{MT}}(\text{X})$  ( $\text{s}^{-1}$ )  
201 can be calculated by:

$$202 \quad k_{\text{MT}} = \left[ \frac{R_{\text{p}}^2}{3D_{\text{g}}} + \frac{4R_{\text{p}}}{3\alpha v} \right]^{-1} \quad (16)$$

203 where  $R_{\text{p}}$  is the aerosol radius,  $D_{\text{g}}$  is the gas-phase molecular diffusion coefficient ( $0.2$   
204  $\text{cm}^2 \text{ s}^{-1}$  at 293K),  $v$  is the mean molecular speed of  $\text{X}$  ( $3 \times 10^4 \text{ cm s}^{-1}$ ), and  $\alpha$  is the mass  
205 accommodation of  $\text{X}$  on the droplet surface, and we adopted values of 0.11 and  $2\text{E}^{-4}$  for  
206  $\text{SO}_2$  and  $\text{NO}_2$ , respectively referring to Cheng et al. (Cheng, 2016).



208

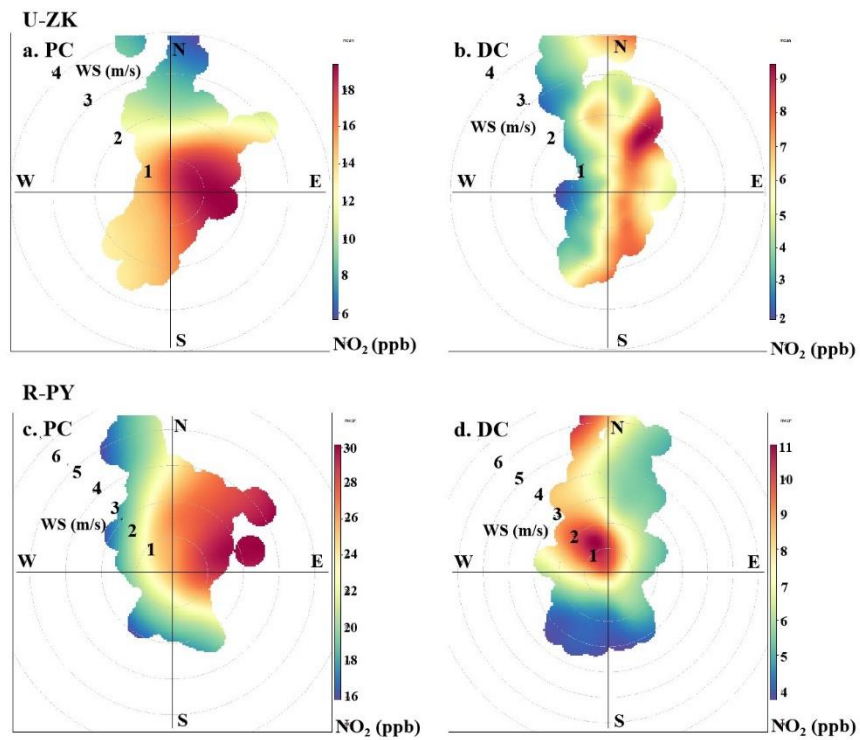
209 Figure S1. Sampling point map in Henan Province, China. © 2019 National Geomatics

210 Center of China. i.e., urban sites at Sanmenxia (U-SMX), Zhoukou (U-ZK), Zhuamdian

211 (U-ZMD) and Xinyang (U-XY), rural sites at Anyang (R-AY), Xinxiang (R-XX),

212 Puyang (R-PY), Jiaozuo(R-JZ), Shangqiu (R-SQ) and Nanyang (R-NY). All rights

213 reserved.

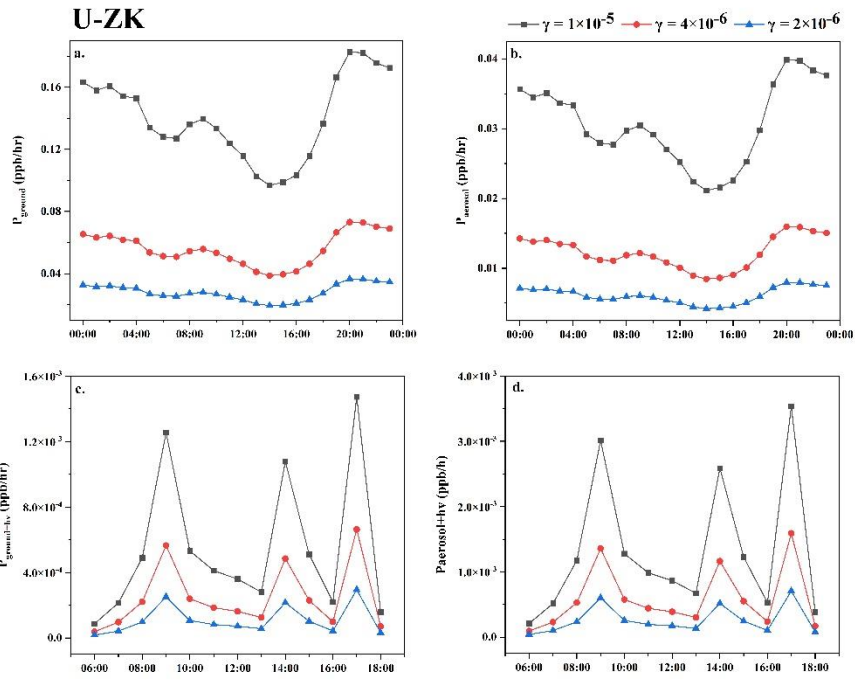


215

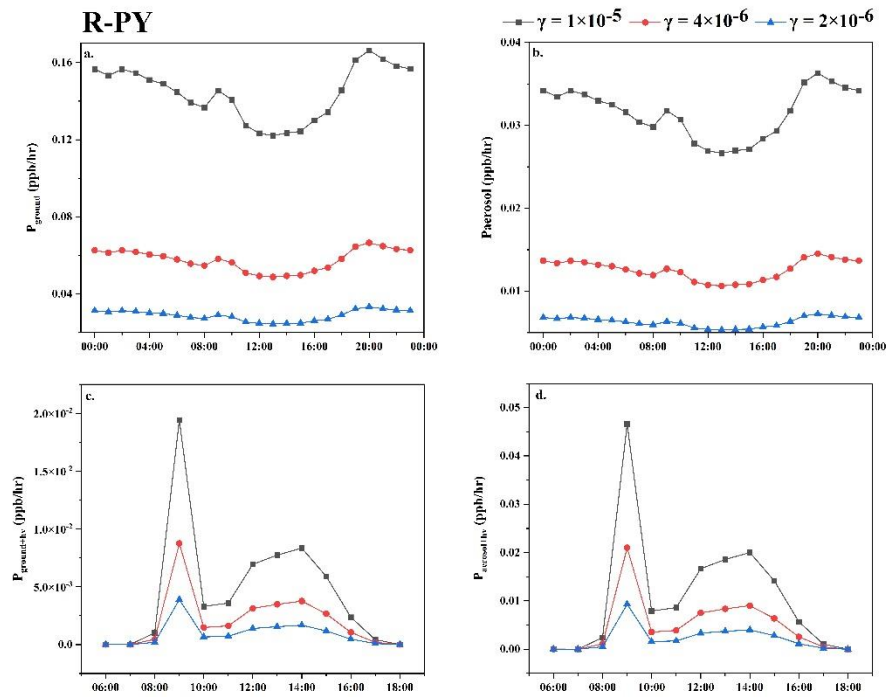
216 Figure S2. Result of conditional bivariate probability function plots: NO<sub>2</sub> at U-ZK and

217 R-PY sites before (PC) and during (DC) the COVID-19 outbreak. The color scale bar

218 represents NO<sub>2</sub> concentration.



219



220

221 **Figure S3. HONO production rate using different uptake rates of NO<sub>2</sub> at the U-ZK**

222 **and R-PY sites before (PC) and during (DC) the COVID-19 outbreak. (a)  $P_{ground}$ , (b)**

223  **$P_{aerosol}$ , (c)  $P_{ground+hv}$ , and (d)  $P_{aerosol+hv}$**

224

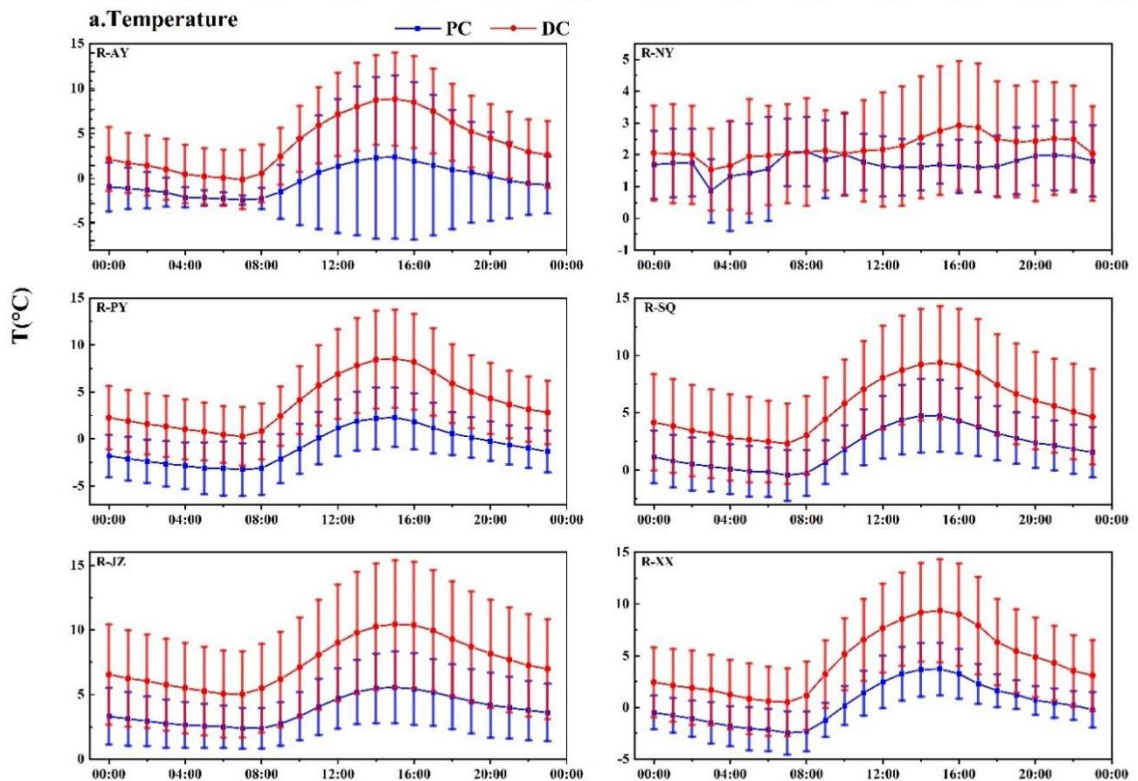
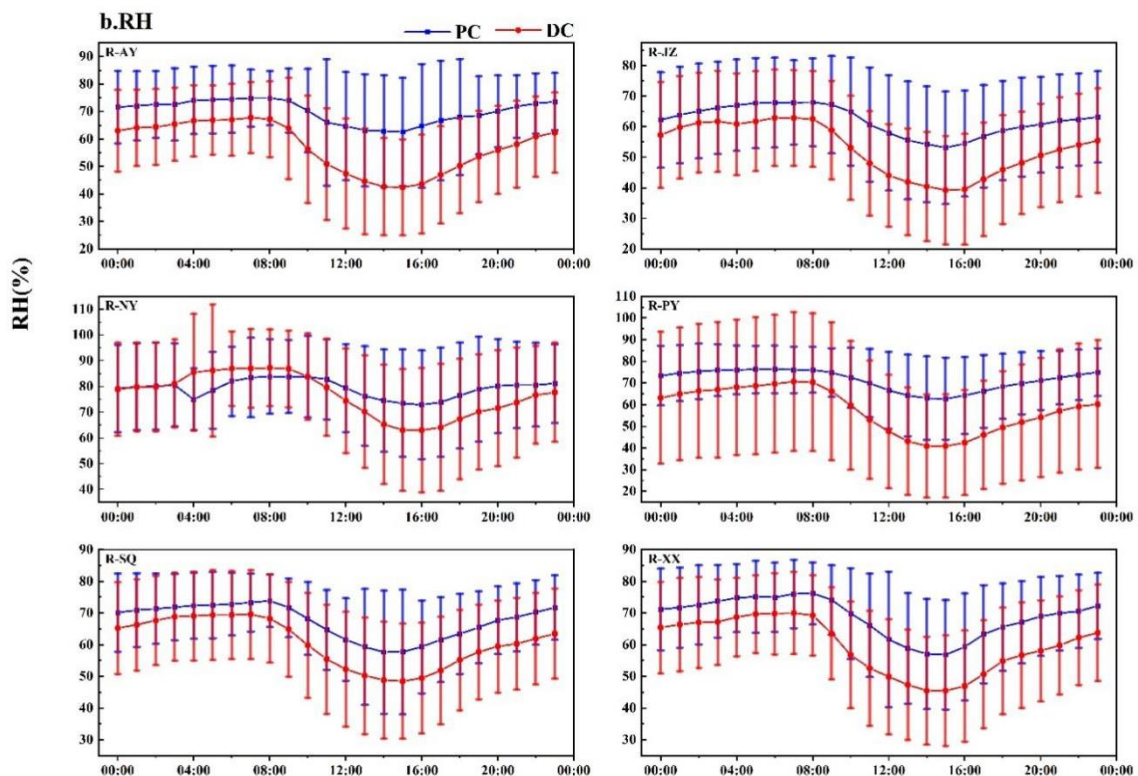
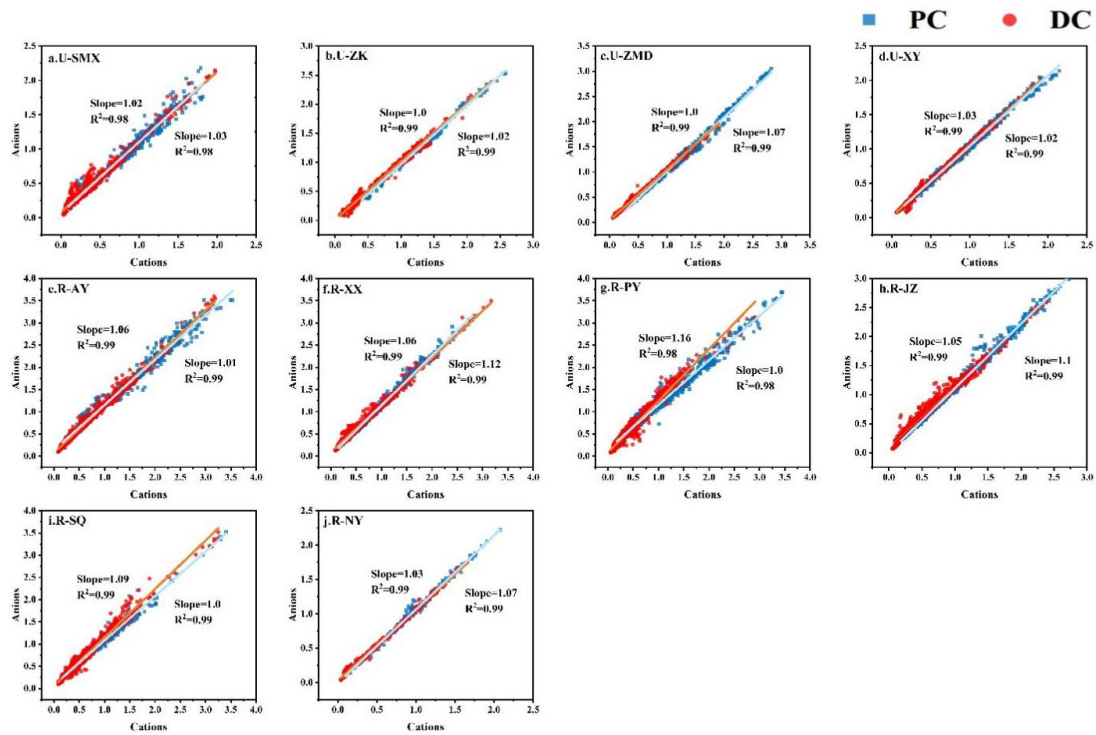


Figure S4. Daily changes in temperature and relative humidity (RH) in rural sites before (PC) and during (DC) the COVID-19 outbreak, the error bar represents the standard deviation. The upper and lower whiskers represent the standard deviation.

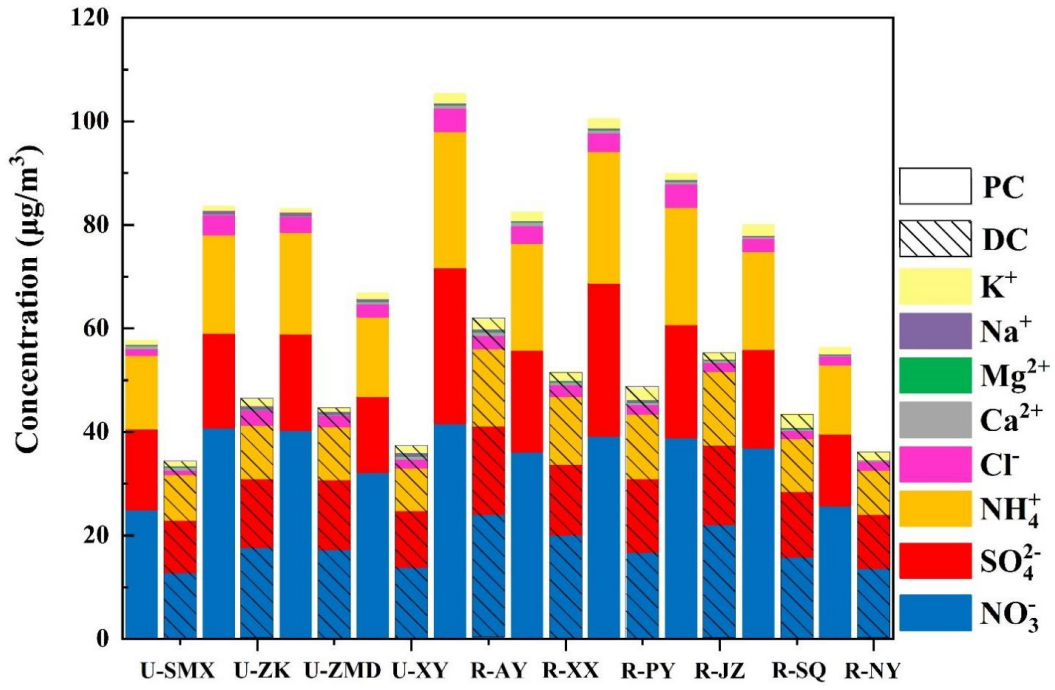




231

232 Figure S5. The equilibrium state of anions and cations at ten sites before (PC) and

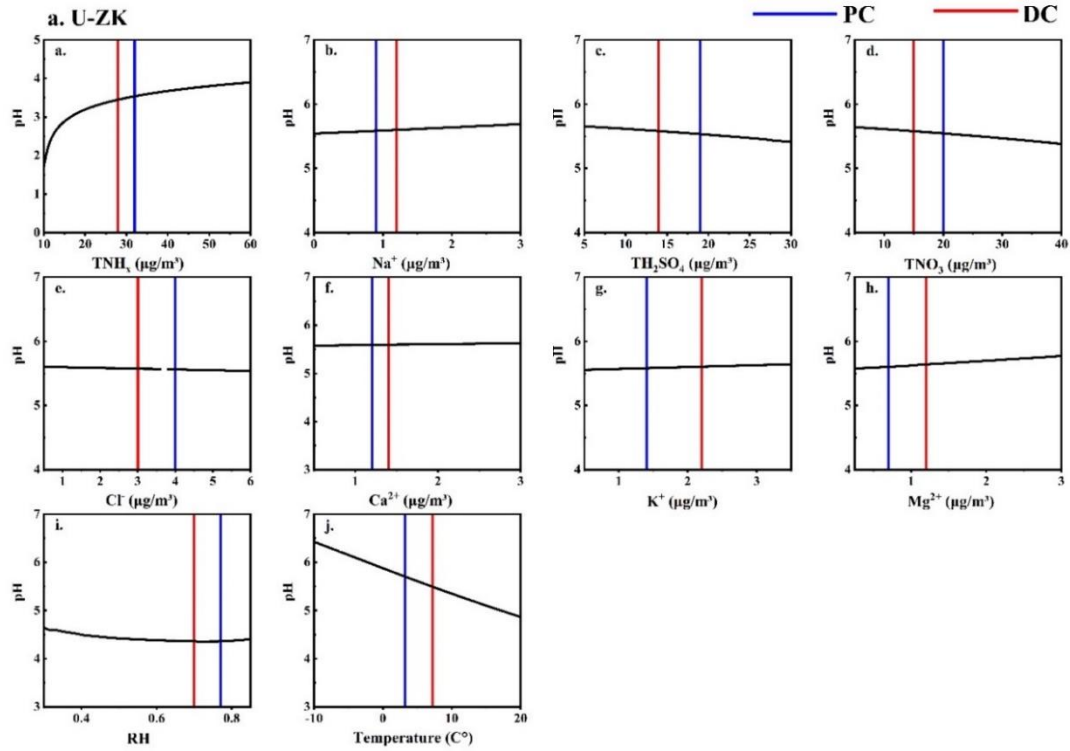
233 during (DC) the COVID-19 outbreak.



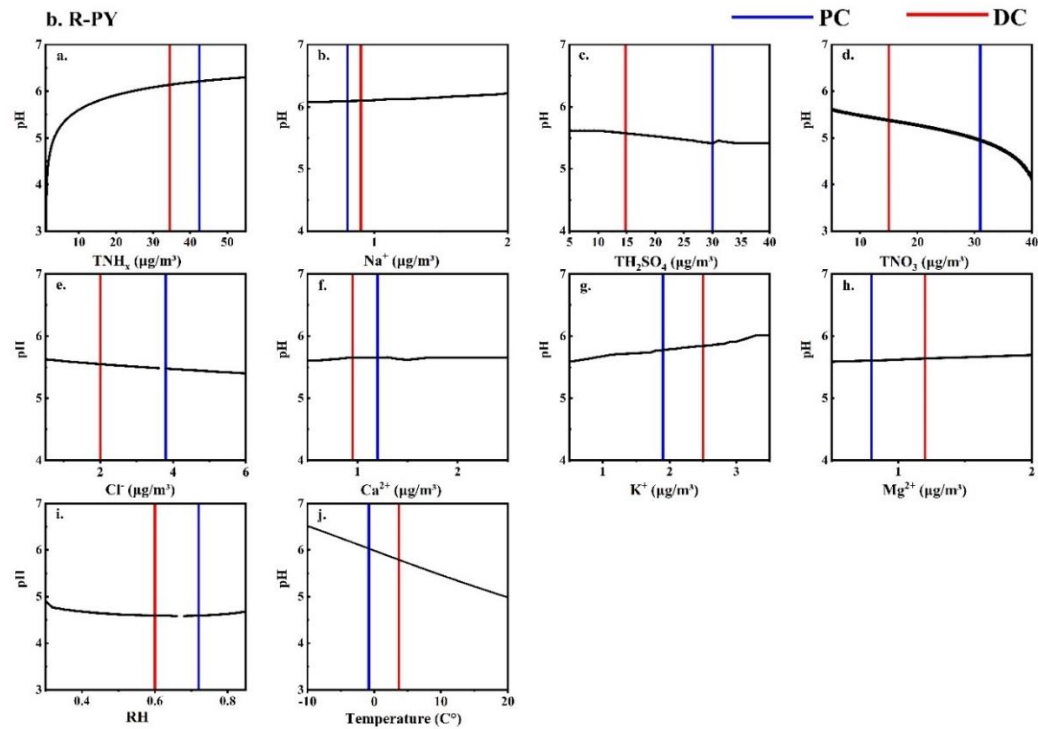
234

235 Figure S6. Concentrations of the water-soluble ions at the ten sites before (PC) and

236 during (DC) the COVID-19 outbreak.

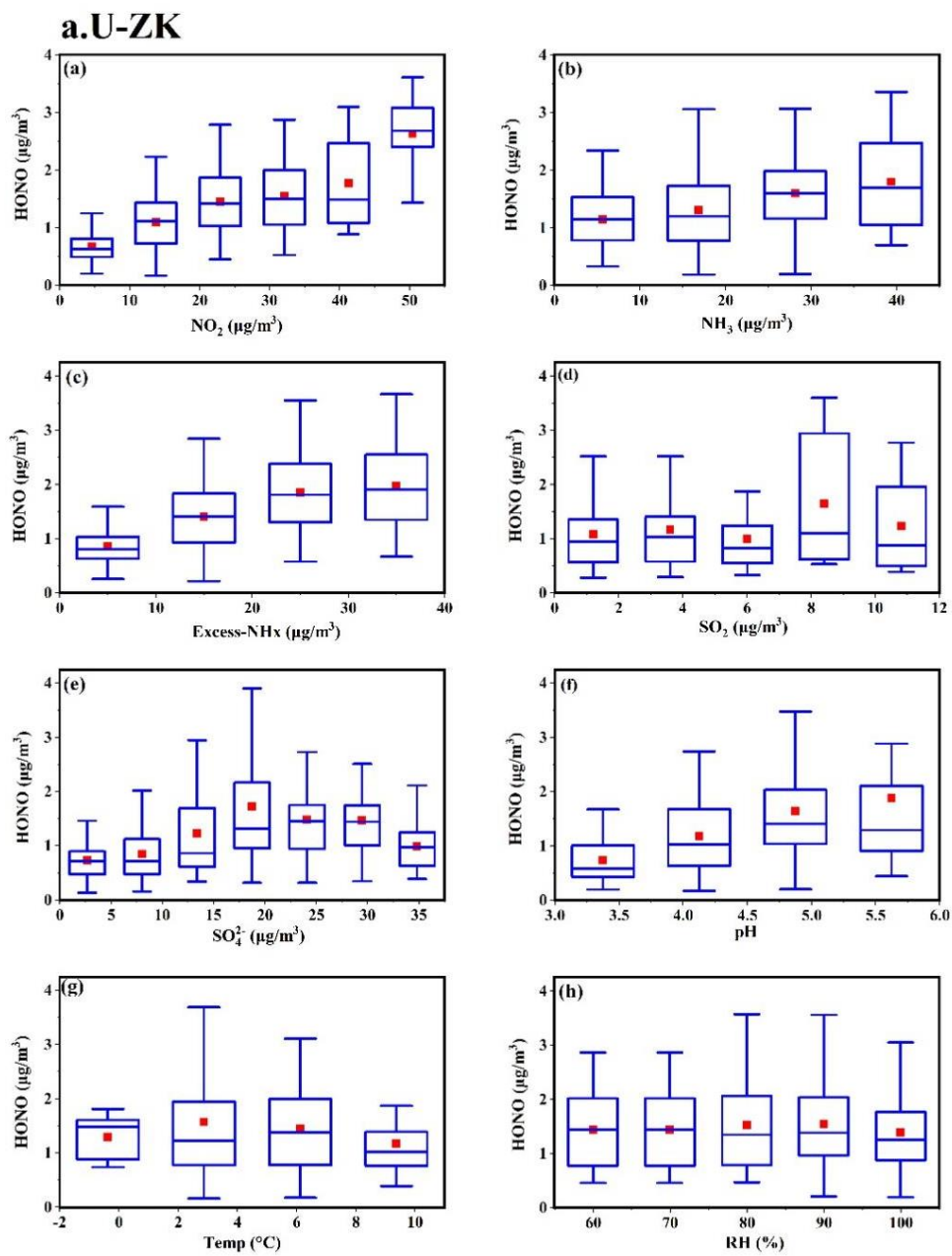


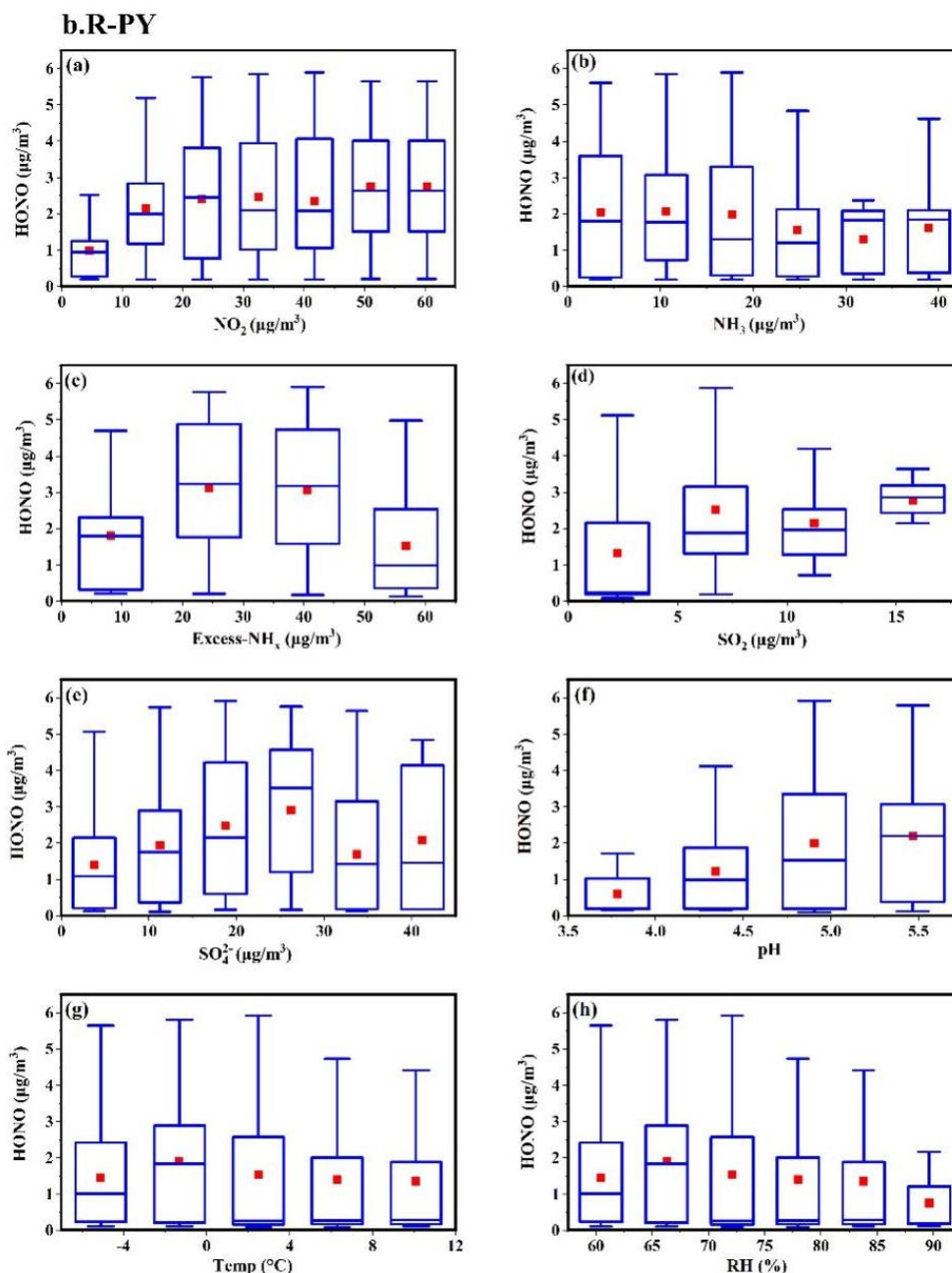
237



238

239 Figure S7. Sensitivity tests of pH to each factor. The vertical bar represents the mean  
 240 values before (PC) and during (DC) the COVID-19 outbreak. A given range for a  
 241 variable (i.e.,  $TNH_x$ ) with corresponding average values of other parameters (i.e.,  
 242  $TH_2SO_4$ ,  $TNO_3$ ,  $TCl$ ,  $TNa$ ,  $K^+$ ,  $Ca^{2+}$ ,  $Mg^{2+}$ ,  $T$ , and  $RH$ ) was simulated to compare its  
 243 effects on pH.





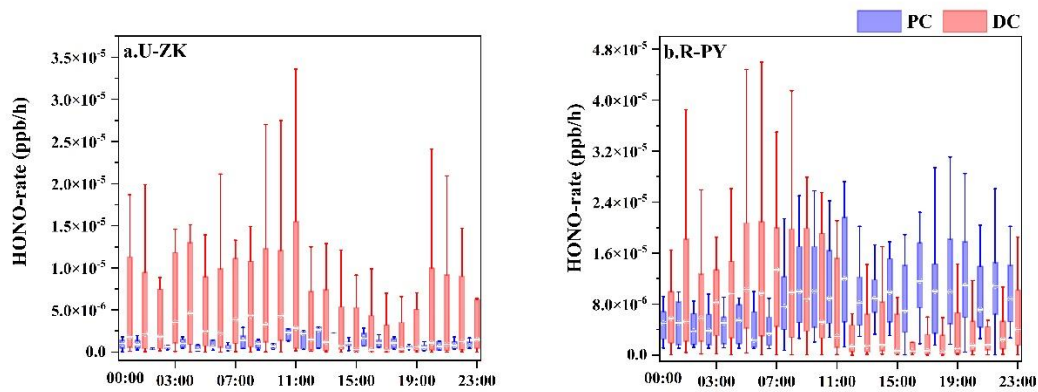
246

247 Figure S8. Relationship between HONO and main influencing factors during (DC) the

248 COVID-19 outbreak at U-ZK and R-PY sites. In each box, the top, middle, and bottom

249 lines represent the 75, 50, and 25 percentiles of statistical data, respectively; the upper

250 and lower whiskers represent the 90 and 10 percentiles of statistical data, respectively.



251

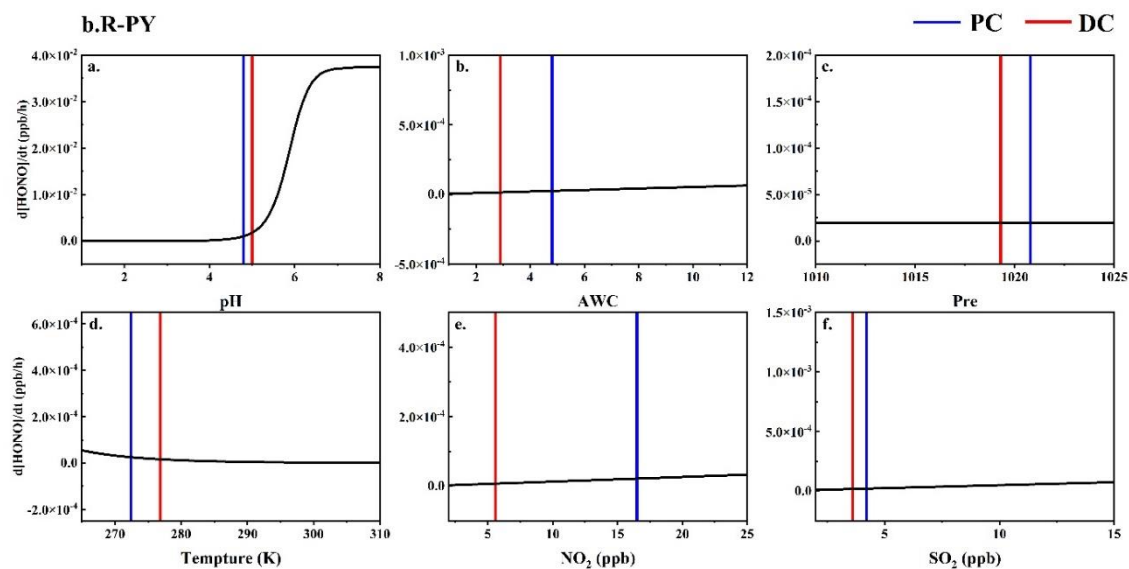
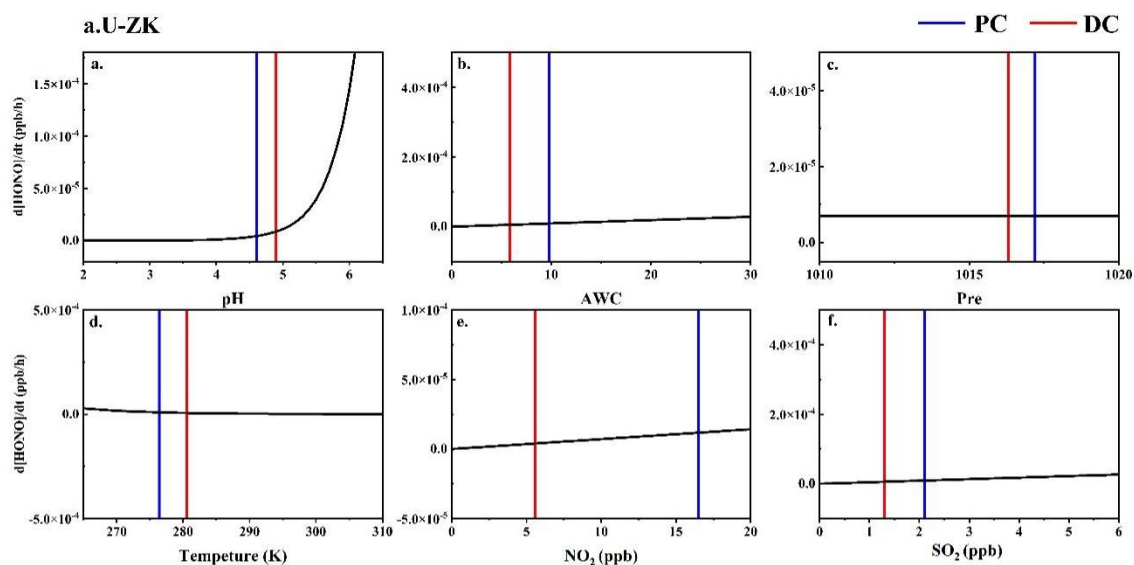
252 Figure. S9. HONO production rate through  $R_1$  at U-ZK and R-PY sites before (PC) and

253 during (DC) the COVID-19 outbreak. In each box, the top, middle, and bottom lines

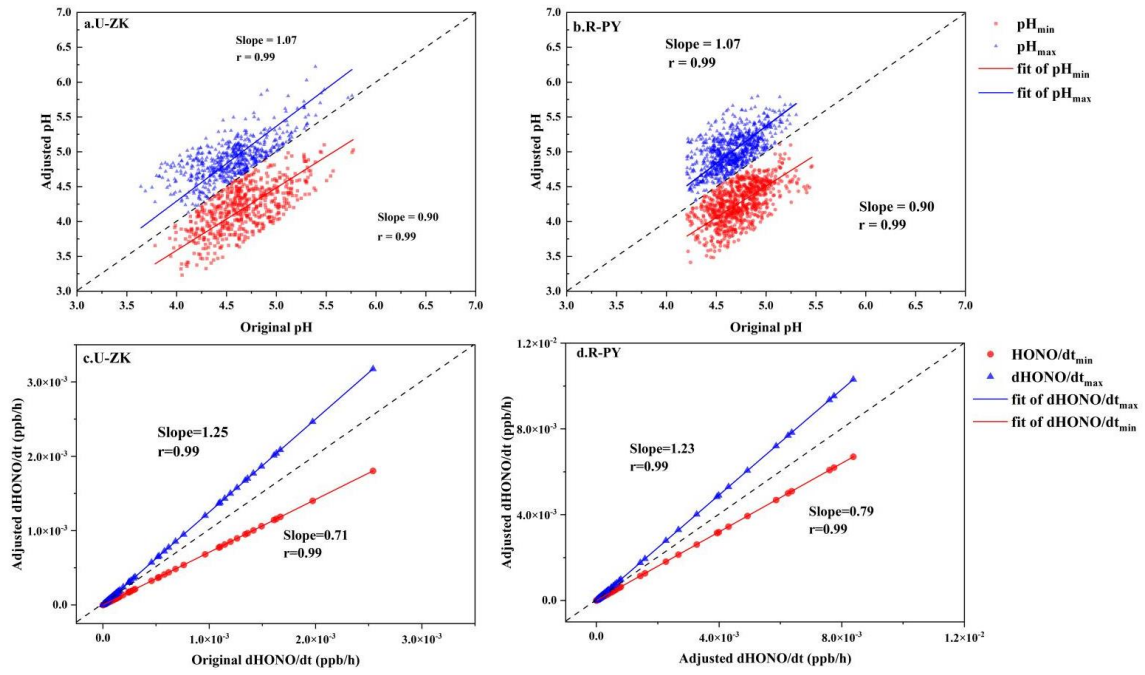
254 represent the 75, 50, and 25 percentiles of statistical data, respectively; the upper and

255 lower whiskers represent the 90 and 10 percentiles of statistical data, respectively.

256



260 Figure S10. Sensitivity of HONO product rate to each factor. The vertical bar represents  
 261 the mean values before (PC) and during (DC) the COVID-19 outbreak. The real-time  
 262 measured values of a variable and the average values of other parameters were input  
 263 into the production rate of the  $R_1$  reaction.



264

265 Figure S11. pH and  $R_1$  uncertainties at the U-ZK and R-PY sites are based on two  
 266 extreme scenarios of sensitivity to measurement uncertainty.

267



268 **Tables**

269

270

271

272

Table S1. Descriptions of the ten sampling sites in Henan Province, China.

Observation sites	Classifications	Abbreviations	Coordinates	Locations	Surrounding environment
Sanmenxia	Urban site	U-SMX	34.79 °N, 111.16 °E	Sanmenxia Environmental Protection Bureau	Roads, residential areas
Zhoukou	Urban site	U-ZK	33.65° N, 114.65° E	Chuanhui District People's Government	Roads, residential areas
Zhumadian	Urban site	U-ZMD	33.01° N, 114.01° E	Huanghuai College	Roads, residential areas, shopping malls
Xinyang	Urban site	U-XY	32.14° N, 114.09° E	Xinyang Museum	Roads, residential areas, shopping malls
Anyang	Rural site	R-AY	36.22°N, 114.39° E	Baizhuang Town Xindian North Street China Resources Gas (Andan Station)	Highways, villages, farmland
Xinxiang	Rural site	R-XX	35.38° N, 114.30° E	Banzao Township Central School in Yanjin County	Villages, farmland
Puyang	Rural site	R-PY	36.15° N, 115.10° E	Nanle County Longwang Temple Station	Villages, farmland
Jiaozuo	Rural site	R-JZ	35.02° N, 113.35° E	The Second River Bureau of Jiefeng Village, Beiguo Township, Wuxi County	Villages, farmland
Shangqiu	Rural site	R-SQ	34.56° N, 115.61° E	Liangyuan Huanghe Gudao National Forest Park	Highways, villages, farmland
Nanyang	Rural site	R-NY	32.68° N, 111.70° E	Nanyang Tangshan Park	Villages, farmland

273

274

Table S2. The value of  $\rho_s$  in other studies.

Observation site	Period	$\rho_s$ (g/cm <sup>3</sup> )	Reference
Beijing	Dec 2016	1.4	(Liu et al., 2017)
Tianjin	Dec-Jun 2015	1.3	(Shi et al., 2017)
Xi'an	Nov-Dec 2012	1.4	(Guo et al., 2017)
Hohhot	Winter 2015	1.35	(Wang et al., 2019)
Northeastern USA	Feb-Mar 2015	1.4	(Guo et al., 2016)
Crete, Greece	Aug-Nov 2012	1.35	(Bougiatioti et al., 2016)
Alabama, USA	Jun-Jul 2013	1.4	(Guo et al., 2015)
Georgia, USA	Aug-Oct 2016	1.4	(Nah et al., 2018)

275

276

Table S3. Summary of vehicle emission factors.

Observation site	Period	Emission factor (%)	Reference
Beijing	2020	0.79	(Meng et al., 2020)
Hong Kong	2015	0.4–1.8	(Yun et al., 2017)
Hong Kong	2011	0.5–1.6	(Xu et al., 2015)
Kiesberg Tunnel	2001	0.8	(Kleffmann et al., 2003)
Kiesberg Tunnel	1997	0.3–0.8	(Kurtenbach and Wiesen, 2001)
Guangzhou	2019	1.31	(Li et al., 2021b)

277

278

Table S4. Constants for calculating the apparent Henry's constant ( $H^*$ ).

Equilibrium	H (M atm <sup>-1</sup> ) at 298K	$-\Delta H_{298K}/R$ (K)
SO <sub>2</sub> (g) ↔ SO <sub>2</sub> (aq)	1.23	3145.3
NO <sub>2</sub> (g) ↔ NO <sub>2</sub> (aq)	1.00E-02	2516.2

279

280

Table S5. Constants for calculating the ionization constants (K).

Equilibrium	K (M) at 298K	$-\Delta H_{298K}/R$ (K)
SO <sub>2</sub> ·H <sub>2</sub> O ↔ H <sup>+</sup> + HSO <sub>3</sub> <sup>-</sup>	1.30E-02	1960
HSO <sub>3</sub> <sup>-</sup> ↔ H <sup>+</sup> + SO <sub>3</sub> <sup>2-</sup>	6.60E-08	1500

281

282 Table S6. Comparisons of NH<sub>3</sub> concentrations (mean ± standard deviation) (µg/m<sup>3</sup>)  
 283 from studies in other cities.

Sampling sites	Seasons	Years	NH <sub>3</sub> (µg/m <sup>3</sup> )	Sites	References
Delhi, India	Winter	2013– 2015	19.2 ± 3.5	Urban	(Saraswati et al., 2019)
Osaka, Japan	Winter	2015	1.5 ± 0.7	Urban	(Huy et al., 2017)
Toronto, Canada	Winter	2007	0.8 ± 0.5	Urban	(Hu et al., 2014)
Kanpur, India	Winter	2007	21.7 ± 5.8	Urban	(Behera and Sharma, 2010)
Nanjing	Winter	2014	6.7	Urban	(Wang et al., 2016b)
Yangtze River Delta	Winter	2019	9.3 ± 4.0	Urban	(Wang et al., 2021)
Shanghai	Winter	2014	2.8 ± 1.0	Urban	(Wang et al., 2018b)
Tianjin	Winter	2015	12.0	Urban	(Shi et al., 2019)
Xi'an	Winter	2012	17.5 ± 9.1	Urban	(Wang et al., 2016a)
Fujian	Winter	2016	12.8 ± 4.8	Urban	(Wu et al., 2017)
Beijing	Winter	2015	15.1 ± 2.9	Urban	(Wang et al., 2016a)
Beijing	Winter	2017	13.1 ± 1.6	Urban	(Zhang et al., 2020b)
Beijing	Winter	2020	19.9 ± 3.8	Urban	(Zhang et al., 2020b)
Taoyuan	Winter	2017– 2018	1.7 ± 1.9	Urban	(Duan et al., 2021)
Zhengzhou	Winter	2018	19.0 ± 4.0	Rural	(Wang et al., 2020)
Quzhou	Winter	2019	29.5 ± 2.2	Rural	(Feng et al., 2022)
Gucheng	Winter	2016	9.3	Rural	(Xu et al., 2019)
Chongming	Winter	2019– 2020	9.3 ± 4.0	Rural	(Lv et al., 2022)
Shanglan	Winter	2017– 2018	2.5 ± 2.6	Rural	(Duan et al., 2021)

284

285

286 Table S7. The concentration (mean  $\pm$  standard deviation) of relative humidity (RH),  
 287 temperature (T),  $\epsilon(\text{NH}_4^+)$  at the ten sites before (PC) and during (DC) the COVID-19  
 288 outbreak.

Sites	Substances	Total	PC	DC
U-SMX	RH (%)	54.8 $\pm$ 18.0	60.6 $\pm$ 16.5	51.2 $\pm$ 18.0
	T ( $^{\circ}\text{C}$ )	5.6 $\pm$ 4.2	3.1 $\pm$ 2.1	7.0 $\pm$ 4.4
	$\epsilon(\text{NH}_4^+)$	0.43 $\pm$ 0.20	0.54 $\pm$ 0.18	0.36 $\pm$ 0.18
U-ZK	RH (%)	70.1 $\pm$ 21.9	73.6 $\pm$ 14.5	69.4 $\pm$ 22.4
	T ( $^{\circ}\text{C}$ )	6.4 $\pm$ 4.3	3.8 $\pm$ 2.3	7.0 $\pm$ 4.5
	$\epsilon(\text{NH}_4^+)$	0.43 $\pm$ 0.20	0.59 $\pm$ 0.14	0.32 $\pm$ 0.17
U-ZMD	RH (%)	74.9 $\pm$ 23.3	84.4 $\pm$ 17.8	68.9 $\pm$ 24.4
	T ( $^{\circ}\text{C}$ )	5.6 $\pm$ 4.6	2.9 $\pm$ 2.7	7.4 $\pm$ 4.8
	$\epsilon(\text{NH}_4^+)$	0.48 $\pm$ 0.21	0.62 $\pm$ 0.17	0.38 $\pm$ 0.18
U-XY	RH (%)	77.0 $\pm$ 22.1	86.7 $\pm$ 13.3	74.3 $\pm$ 23.3
	T ( $^{\circ}\text{C}$ )	7.7 $\pm$ 4.5	4.7 $\pm$ 2.2	8.5 $\pm$ 4.6
	$\epsilon(\text{NH}_4^+)$	0.55 $\pm$ 0.21	0.71 $\pm$ 0.14	0.45 $\pm$ 0.18
R-AY	RH (%)	62.2 $\pm$ 17.9	70.1 $\pm$ 14.9	57.2 $\pm$ 17.8
	T ( $^{\circ}\text{C}$ )	2.6 $\pm$ 0.9	-0.2 $\pm$ 2.5	4.4 $\pm$ 4.7
	$\epsilon(\text{NH}_4^+)$	0.46 $\pm$ 0.17	0.57 $\pm$ 0.15	0.39 $\pm$ 0.14
R-XX	RH (%)	63.0 $\pm$ 17.0	68.7 $\pm$ 14.6	59.5 $\pm$ 17.5
	T ( $^{\circ}\text{C}$ )	2.9 $\pm$ 4.6	0.3 $\pm$ 2.8	4.4 $\pm$ 4.8
	$\epsilon(\text{NH}_4^+)$	0.40 $\pm$ 0.17	0.52 $\pm$ 0.16	0.35 $\pm$ 0.14
R-PY	RH (%)	63.6 $\pm$ 18.0	71.5 $\pm$ 14.6	57.6 $\pm$ 18.0
	T ( $^{\circ}\text{C}$ )	1.7 $\pm$ 4.8	-0.8 $\pm$ 3.2	3.6 $\pm$ 4.9
	$\epsilon(\text{NH}_4^+)$	0.43 $\pm$ 0.17	0.58 $\pm$ 0.13	0.34 $\pm$ 0.13
R-JZ	RH (%)	56.3 $\pm$ 18.5	62.0 $\pm$ 16.7	52.8 $\pm$ 18.7
	T ( $^{\circ}\text{C}$ )	4.1 $\pm$ 4.4	1.7 $\pm$ 2.6	5.6 $\pm$ 4.7
	$\epsilon(\text{NH}_4^+)$	0.37 $\pm$ 0.14	0.46 $\pm$ 0.13	0.32 $\pm$ 0.13
R-SQ	RH (%)	63.2 $\pm$ 15.6	67.5 $\pm$ 12.6	60.5 $\pm$ 17.0
	T ( $^{\circ}\text{C}$ )	4.2 $\pm$ 4.5	2.0 $\pm$ 2.9	5.6 $\pm$ 4.7
	$\epsilon(\text{NH}_4^+)$	0.45 $\pm$ 0.19	0.63 $\pm$ 0.12	0.35 $\pm$ 0.14
R-NY	RH (%)	75.9 $\pm$ 19.1	79.3 $\pm$ 17.7	73.9 $\pm$ 19.6
	T ( $^{\circ}\text{C}$ )	5.7 $\pm$ 3.8	3.6 $\pm$ 2.6	6.9 $\pm$ 3.9
	$\epsilon(\text{NH}_4^+)$	0.59 $\pm$ 0.19	0.73 $\pm$ 0.12	0.52 $\pm$ 0.18

289

290 Table S8. The concentration (mean  $\pm$  standard deviation) of required ammonia  
 291 (Required-NH<sub>x</sub>) and excess ammonia (Excess-NH<sub>x</sub>) at the ten sites before (PC) and  
 292 during (DC) the COVID-19 outbreak.

Sites	Substances	Total ( $\mu\text{g}/\text{m}^3$ )	PC ( $\mu\text{g}/\text{m}^3$ )	DC ( $\mu\text{g}/\text{m}^3$ )
U-SMX	Required-NH <sub>4</sub> <sup>+</sup>	9.1 $\pm$ 7.1	12.7 $\pm$ 7.1	7.0 $\pm$ 6.2
	Excess-NH <sub>4</sub> <sup>+</sup>	14.7 $\pm$ 11.2	13.6 $\pm$ 10.4	15.3 $\pm$ 11.6
U-ZK	Required-NH <sub>4</sub> <sup>+</sup>	15.2 $\pm$ 9.6	21.4 $\pm$ 8.6	11.6 $\pm$ 8.4
	Excess-NH <sub>4</sub> <sup>+</sup>	14.6 $\pm$ 8.3	11.9 $\pm$ 6.0	16.1 $\pm$ 9.0
U-ZMD	Required-NH <sub>4</sub> <sup>+</sup>	13.9 $\pm$ 9.8	19.4 $\pm$ 9.8	10.4 $\pm$ 8.0
	Excess-NH <sub>4</sub> <sup>+</sup>	12.8 $\pm$ 8.7	11.6 $\pm$ 8.2	13.6 $\pm$ 8.8
U-XY	Required-NH <sub>4</sub> <sup>+</sup>	10.2 $\pm$ 7.5	14.6 $\pm$ 7.3	7.4 $\pm$ 6.2
	Excess-NH <sub>4</sub> <sup>+</sup>	7.8 $\pm$ 4.6	6.5 $\pm$ 4.4	8.7 $\pm$ 4.5
R-AY	Required-NH <sub>4</sub> <sup>+</sup>	17.1 $\pm$ 12.4	23.9 $\pm$ 13.4	12.8 $\pm$ 9.5
	Excess-NH <sub>4</sub> <sup>+</sup>	21.2 $\pm$ 9.4	20.2 $\pm$ 9.2	21.9 $\pm$ 9.4
R-XX	Required-NH <sub>4</sub> <sup>+</sup>	13.5 $\pm$ 9.6	18.0 $\pm$ 9.8	10.7 $\pm$ 8.2
	Excess-NH <sub>4</sub> <sup>+</sup>	23.3 $\pm$ 11.4	19.6 $\pm$ 10.8	25.6 $\pm$ 11.2
R-PY	Required-NH <sub>4</sub> <sup>+</sup>	13.8 $\pm$ 11.0	22.1 $\pm$ 12.5	9.3 $\pm$ 6.6
	Excess-NH <sub>4</sub> <sup>+</sup>	22.3 $\pm$ 10.8	17.5 $\pm$ 8.6	25.0 $\pm$ 11.0
R-JZ	Required-NH <sub>4</sub> <sup>+</sup>	15.4 $\pm$ 10.4	20.3 $\pm$ 10.6	12.5 $\pm$ 9.1
	Excess-NH <sub>4</sub> <sup>+</sup>	27.5 $\pm$ 12.9	26.0 $\pm$ 13.1	28.4 $\pm$ 12.7
R-SQ	Required-NH <sub>4</sub> <sup>+</sup>	13.2 $\pm$ 9.1	19.1 $\pm$ 8.9	9.9 $\pm$ 7.3
	Excess-NH <sub>4</sub> <sup>+</sup>	15.1 $\pm$ 8.6	10.1 $\pm$ 5.4	17.9 $\pm$ 8.7
R-NY	Required-NH <sub>4</sub> <sup>+</sup>	9.9 $\pm$ 6.6	13.0 $\pm$ 6.9	8.1 $\pm$ 5.8
	Excess-NH <sub>4</sub> <sup>+</sup>	6.0 $\pm$ 3.6	4.4 $\pm$ 3.3	6.9 $\pm$ 3.4

293

294  
295

Table S9. Comparison of the particle pH values in this study (PC/DC) and other sites (mean or mean  $\pm$  standard).

	Sites	Periods	pH	References
Urban	Sanmenxia	Jan–Feb 2020	4.6 $\pm$ 0.5/4.8 $\pm$ 0.9	This study
	Zhoukou	Jan–Feb 2020	4.6 $\pm$ 0.6/5.1 $\pm$ 0.4	
	Zhumadian	Jan–Feb 2020	4.6 $\pm$ 0.3/4.8 $\pm$ 1.2	
	Xinyang	Jan–Feb 2020	4.2 $\pm$ 0.3/4.6 $\pm$ 1.3	
Rural	Anyang	Jan–Feb 2020	4.5 $\pm$ 0.4/4.6 $\pm$ 0.8	
	Xinxiang	Jan–Feb 2020	4.8 $\pm$ 0.5/4.9 $\pm$ 0.9	
	Puyang	Jan–Feb 2020	4.8 $\pm$ 0.3/5.1 $\pm$ 0.9	
	Jiaozuo	Jan–Feb 2020	4.9 $\pm$ 0.5/5.1 $\pm$ 0.8	
	Shangqiu	Jan–Feb 2020	4.5 $\pm$ 0.3/4.7 $\pm$ 0.8	
	Nanyang	Jan–Feb 2020	4.2 $\pm$ 0.5/4.4 $\pm$ 0.7	
Urban	Beijing	Jan–Feb 2015	4.5	(Guo et al., 2017)
	Beijing	Dec 2016	4.3 $\pm$ 0.4	(Liu et al., 2017)
	Beijing	Feb 2017	4.5 $\pm$ 0.7	(Ding et al., 2019)
	Tianjin	Dec–Jun 2015	4.9 $\pm$ 1.4	(Shi et al., 2017)
	Tianjin	Aug 2015	3.4 $\pm$ 0.5	(Shi et al., 2019)
	Hohhot	Winter	5.7	(Wang et al., 2019)
	Mt. Tai	Summer	2.9 $\pm$ 0.5	(Liu et al., 2021b)
	Taoyuan	Nov 2017–Jan 2018	5.1 $\pm$ 1.0	(Duan et al., 2021)
	Zhengzhou	Jan 2018	4.5	(Wang et al., 2020)
	Anyang	Jan 2018	4.8	(Wang et al., 2020)
Mountain	Mt. Tai	Summer	3.6 $\pm$ 0.7	(Liu et al., 2021b)
Rural	Shanglan	Nov 2017–Jan 2018	5.5 $\pm$ 1.1	(Duan et al., 2021)

296

297 **References**

- 298 Behera, S. N., and Sharma, M.: Investigating the potential role of ammonia in ion  
299 chemistry of fine particulate matter formation for an urban environment, *Sci. Total*  
300 *Environ.*, 408, 3569–3575, <https://doi.org/10.1016/j.scitotenv.2010.04.017>, 2010.
- 301 Bougiatioti, A., Nikolaou, P., Stavroulas, I., Kouvarakis, G., Weber, R., Nenes, A.,  
302 Kanakidou, M., and Mihalopoulos, N.: Particle water and pH in the eastern  
303 Mediterranean: source variability and implications for nutrient availability, *Atmos.*  
304 *Chem. Phys.*, 16, 4579–4591, <https://doi.org/10.5194/acp-16-4579-2016>, 2016.
- 305 Burling, I. R., Yokelson, R. J., Griffith, D. W. T., Johnson, T. J., Veres, P., Roberts, J.  
306 M., Warneke, C., Urbanski, S. P., Reardon, J., Weise, D. R., Hao, W. M., and de  
307 Gouw, J.: Laboratory measurements of trace gas emissions from biomass burning  
308 of fuel types from the southeastern and southwestern United States, *Atmos. Chem.*  
309 *Phys.*, 10, 11115–11130, <https://doi.org/10.5194/acp-10-11115-2010>, 2010.
- 310 Chen, D., Zhou, L., Liu, S., Lian, C., Wang, W., Liu, H., Li, C., Liu, Y., Luo, L., Xiao,  
311 K., Chen, Y., Qiu, Y., Tan, Q., Ge, M., and Yang, F.: Primary sources of HONO  
312 vary during the daytime: Insights based on a field campaign, *Sci. Total Environ.*,  
313 903, <https://doi.org/10.1016/j.scitotenv.2023.166605>, 2023.
- 314 Cheng, Y., Zheng, G., Wei, C., Mu, Q., Zheng, B., Wang, Z., Gao, M., Z., Q., He, K.,  
315 Carmichael, G., Pöschl, U., and Su, and H.: Reactive nitrogen chemistry in aerosol  
316 water as a source of sulfate during haze events in China, *Sci. Adv.* 2, e1601530.,  
317 <https://doi.org/10.1126/sciadv.1601530>, 2019.
- 318 Ding, J., Zhao, P., Su, J., Dong, Q., Du, X., and Zhang, Y.: Aerosol pH and its driving  
319 factors in Beijing, *Atmos. Chem. Phys.* 19, 7939–7954,  
320 <https://doi.org/10.5194/acp-19-7939-2019>, 2019.
- 321 Duan, X., Yan, Y., Peng, L., Xie, K., Hu, D., Li, R., and Wang, C.: Role of ammonia in

322 secondary inorganic aerosols formation at an ammonia-rich city in winter in North  
323 China: A comparative study among industry, urban, and rural sites, *Environ.*  
324 *Pollut.*, 291, 118151, <https://doi.org/10.1016/j.envpol.2021.118151>, 2021.

325 Feng, S., Xu, W., Cheng, M., Ma, Y., Wu, L., Kang, J., Wang, K., Tang, A., Collett, J.  
326 L., Fang, Y., Goulding, K., Liu, X., and Zhang, F.: Overlooked nonagricultural and  
327 wintertime agricultural NH<sub>3</sub> emissions in Quzhou county, North China Plain:  
328 evidence from <sup>15</sup>N-Stable Isotopes. *Environ. Sci. Technol. Lett.* 9, 127–133,  
329 <https://doi.org/10.1021/acs.estlett.1c00935>, 2022.

330 Fuchs, H., Tan, Z., Lu, K., Bohn, B., Broch, S., Brown, S. S., Dong, H., Gomm, S.,  
331 Häsel, R., He, L., Hofzumahaus, A., Holland, F., Li, X., Liu, Y., Lu, S., Min, K.-  
332 E., Rohrer, F., Shao, M., Wang, B., Wang, M., Wu, Y., Zeng, L., Zhang, Y., Wahner,  
333 A., and Zhang, Y.: OH reactivity at a rural site (Wangdu) in the North China Plain:  
334 contributions from OH reactants and experimental OH budget, *Atmos. Chem.*  
335 *Phys.*, 17, 645–661, <https://doi.org/10.5194/acp-17-645-2017>, 2017.

336 Guo, H., Xu, L., Bougiatioti, A., Cerully, K. M., Capps, S. L., Hite, J. R., Carlton, A.  
337 G., Lee, S. H., Bergin, M. H., Ng, N. L., Nenes, A., and Weber, R. J.: Fine-particle  
338 water and pH in the southeastern United States, *Atmos. Chem. Phys.*, 15, 5211–  
339 5228, <https://doi.org/10.5194/acp-15-5211-2015>, 2015.

340 Guo, H., Sullivan, A. P., Campuzano-Jost, P., Schroder, J. C., Lopez-Hilfiker, F. D.,  
341 Dibb, J. E., Jimenez, J. L., Thornton, J. A., Brown, S. S., Nenes, A., and Weber, R.  
342 J.: Fine particle pH and the partitioning of nitric acid during winter in the  
343 northeastern United States, *J. Geophys. Res.: Atmos.*, 121,  
344 <https://doi.org/10.1002/2016jd025311>, 2016.

345 Guo, H., Weber, R. J., and Nenes, A.: High levels of ammonia do not raise fine particle  
346 pH sufficiently to yield nitrogen oxide-dominated sulfate production, *Sci. Rep.*, 7,  
347 12109, <https://doi.org/10.1038/s41598-017-11704-0>, 2017.

348 Hao, Q., Jiang, N., Zhang, R., Yang, L., and Li, S.: Characteristics, sources, and



349 reactions of nitrous acid during winter at an urban site in the Central Plains  
350 Economic Region in China, *Atmos. Chem. Phys.* 20, 7087–7102,  
351 <https://doi.org/10.5194/acp-20-7087-2020>, 2020.

352 Hu, B., Duan, J., Hong, Y., Xu, L., Li, M., Bian, Y., Qin, M., Fang, W., Xie, P., and  
353 Chen, J.: Exploration of the atmospheric chemistry of nitrous acid in a coastal city  
354 of southeastern China: results from measurements across four seasons, *Atmos.*  
355 *Chem. Phys.*, 22, 371–393, <https://doi.org/10.5194/acp-22-371-2022>, 2022.

356 Hu, Q., Zhang, L., Evans, G. J., and Yao, X.: Variability of atmospheric ammonia  
357 related to potential emission sources in downtown Toronto, Canada, *Atmos.*  
358 *Environ.* 99, 365–373, <https://doi.org/10.1016/j.atmosenv.2014.10.006>, 2014.

359 Huang, R., Yang, L., Cao, J., Wang, Q., Tie, X., Ho, K., Shen, Z., Zhang, R., Li, G.,  
360 Zhu, C., Zhang, N., Dai, W., Zhou, J., Liu, S., Chen, Y., Chen, J., and O'Dowd, C.  
361 D.: Concentration and sources of atmospheric nitrous acid (HONO) at an urban  
362 site in Western China, *Sci. Total. Environ.* 02, 165–172.  
363 <https://doi.org/10.1016/j.scitotenv.2017.02.166>, 2017.

364 Huy, D. H., Thanh, L. T., Hien, T. T., Noro, K., and Takenaka, N.: Characteristics of  
365 ammonia gas and fine particulate ammonium from two distinct urban areas: Osaka,  
366 Japan, and Ho Chi Minh City, Vietnam, *Environ Environ. Sci. Pollut. Res. Int.* 24,  
367 8147–8163, <https://doi.org/10.1007/s11356-017-8496-5>, 2017.

368 Kleffmann, J., Kurtenbach, R., Lörzer, J., Wiesen, P., Kalthoff, N., Vogel, B., and Vogel,  
369 H.: Measured and simulated vertical profiles of nitrous acid—Part I: Field  
370 measurements, *Atmos. Environ.*, 37, 2949–2955, [https://doi.org/10.1016/s1352-](https://doi.org/10.1016/s1352-2310(03)00242-5)  
371 [2310\(03\)00242-5](https://doi.org/10.1016/s1352-2310(03)00242-5), 2003.

372 Kramer, L. J., Crilley, L. R., Adams, T. J., Ball, S. M., Pope, F. D., and Bloss, W. J.:  
373 Nitrous acid (HONO) emissions under real-world driving conditions from vehicles  
374 in a UK road tunnel, *Atmos. Chem. Phys.* 20, 5231–5248,  
375 <https://doi.org/10.5194/acp-20-5231-2020>, 2020.

376 Kurtenbach, R., Becker, K.H., Gomes, J.A.G., Kleffmann, J., Lorzer, J.C., Spittler, M.,  
377 510, and Wiesen, P., Ackermann, R., Geyer, A., Platt, U.: Investigations of  
378 emissions and heterogeneous formation of HONO in a road traffic tunnel, *Atmos.*  
379 *Environ.*, 35, 3385-3394, [https://doi.org/10.1016/S1352-2310\(01\)00138-8](https://doi.org/10.1016/S1352-2310(01)00138-8), 2001.

380 Li, D., Xue, L., Wen, L., Wang, X., Chen, T., Mellouki, A., Chen, J., and Wang, W.:  
381 Characteristics and sources of nitrous acid in an urban atmosphere of northern  
382 China: Results from 1-yr continuous observations, *Atmos. Environ.*, 182, 296–306,  
383 <https://doi.org/10.1016/j.atmosenv.2018.03.033>, 2018.

384 Li, S., Song, W., Zhan, H., Zhang, Y., Zhang, X., Li, W., Tong, S., Pei, C., Wang, Y.,  
385 Chen, Y., Huang, Z., Zhang, R., Zhu, M., Fang, H., Wu, Z., Wang, J., Luo, S., Fu,  
386 X., Xiao, S., Huang, X., Zeng, J., Zhang, H., Chen, D., Gligorovski, S., Ge, M.,  
387 George, C., and Wang, X.: Contribution of vehicle emission and NO<sub>2</sub> surface  
388 conversion to nitrous acid (HONO) in urban environments: Implications from tests  
389 in a tunnel, *Environ Sci Technol*, 55, 15616–15624,  
390 <https://doi.org/10.1021/acs.est.1c00405>, 2021.

391 Li, X., Brauers, T., Haseler, R., Bohn, B., Fuchs, H., Hofzumahaus, A., Holland, F., Lou,  
392 S., Lu, K.D., Rohrer, F., Hu, M., Zeng, L.M., Zhang, Y.H., Garland, R.M., Su, H.,  
393 Nowak, A., Wiedensohler, A., Takegawa, N., Shao, M., and Wahner, A.: Exploring  
394 the atmospheric chemistry of nitrous acid (HONO) at a rural site in Southern China.  
395 *Atmos. Chem. Phys.* 12, 1497–1513, 2012.

396 Liu, J., Liu, Z., Ma, Z., Yang, S., Yao, D., Zhao, S., Hu, B., Tang, G., Sun, J., Cheng,  
397 M., Xu, Z., and Wang, Y.: Detailed budget analysis of HONO in Beijing, China:  
398 Implication on atmosphere oxidation capacity in polluted megacity, *Atmos.*  
399 *Environ.*, 244, <https://doi.org/10.1016/j.atmosenv.2020.117957>, 2021a.

400 Liu, M., Song, Y., Zhou, T., Xu, Z., Yan, C., Zheng, M., Wu, Z., Hu, M., Wu, Y., and  
401 Zhu, T.: Fine particle pH during severe haze episodes in northern China, *Geophys.*  
402 *Res. Lett.* 44, 5213–5221, <https://doi.org/10.1002/2017gl073210>, 2017.

403 Liu, P., Zhao, X., Zhang, C., Chen, H., Wang, J., Xue, L., Chen, J., and Mu, Y.: Fine  
404 particle pH and its influencing factors during summer at Mt. Tai: Comparison  
405 between mountain and urban sites, *Atmos. Environ.*, 261,  
406 <https://doi.org/10.1016/j.atmosenv.2021.118607>, 2021.

407 Liu, Y., Ni, S., Jiang, T., Xing, S., Zhang, Y., Bao, X., Feng, Z., Fan, X., Zhang, L., and  
408 Feng, H.: Influence of Chinese New Year overlapping COVID-19 lockdown on  
409 HONO sources in Shijiazhuang, *Sci Total Environ*, 745, 141025,  
410 <https://doi.org/10.1016/j.scitotenv.2020.141025>, 2020.

411 Lv, S., Wang, F., Wu, C., Chen, Y., Liu, S., Zhang, S., Li, D., Du, W., Zhang, F., Wang,  
412 H., Huang, C., Fu, Q., Duan, Y., and Wang, G.: Gas-to-aerosol phase partitioning  
413 of atmospheric water-soluble organic compounds at a rural site in China: an  
414 enhancing effect of NH<sub>3</sub> on SOA formation. *Environ. Sci. Technol.* 56, 3915–3924,  
415 <https://doi.org/10.1021/acs.est.1c06855>, 2022.

416 Lyu, X., Wang, N., Guo, H., Xue, L., Jiang, F., Zeren, Y., Cheng, H., Cai, Z., Han, L.,  
417 and Zhou, Y.: Causes of a continuous summertime O<sub>3</sub> pollution event in Jinan, a  
418 central city in the North China Plain, *Atmos. Chem. Phys.*, 19, 3025–3042,  
419 <https://doi.org/10.5194/acp-19-3025-2019>, 2019.

420 Meng, F., Qin, M., Tang, K., Duan, J., Fang, W., Liang, S., Ye, K., Xie, P., Sun, Y., Xie,  
421 C., Ye, C., Fu, P., Liu, J., and Liu, W.: High-resolution vertical distribution and  
422 sources of HONO and NO<sub>2</sub> in the nocturnal boundary layer in urban Beijing, China,  
423 *Atmos. Chem. Phys.*, 20, 5071–5092, <https://doi.org/10.5194/acp-20-5071-2020>,  
424 2020.

425 Mikuska, P., Motyka, K., and Vecera, Z.: Determination of nitrous acid in air using wet  
426 effluent diffusion denuder–FIA technique, *Talanta*; 77, 635–641,  
427 <https://doi.org/10.1016/j.talanta.2008.07.008>, 2008.

428 Nah, T., Guo, H., Sullivan, A. P., Chen, Y., Tanner, D. J., Nenes, A., Russell, A., Ng, N.  
429 L., Huey, L. G., and Weber, R. J.: Characterization of aerosol composition, aerosol

430 acidity, and organic acid partitioning at an agriculturally intensive rural  
431 southeastern US site, *Atmos. Chem. Phys.*, 18, 11471–11491,  
432 <https://doi.org/10.5194/acp-18-11471-2018>, 2018.

433 Rumsey, I. C., Cowen, K. A., Walker, J. T., Kelly, T. J., Hanft, E. A., Mishoe, K., Rogers,  
434 C., Proost, R., Beachley, G. M., Lear, G., Frelink, T., and Otjes, R. P.: An  
435 assessment of the performance of the Monitor for aerosols and gases in ambient  
436 air (MARGA): a semi-continuous method for soluble compounds. *Atmos. Chem.  
437 and Phys.* 14, 5639–5658, <https://doi.org/10.5194/acp-14-5639-2014>, 2014.

438 Saraswati, Sharma, S. K., Saxena, M., and Mandal, T. K.: Characteristics of gaseous  
439 and particulate ammonia and their role in the formation of secondary inorganic  
440 particulate matter at Delhi, India, *Atmos. Res.* 218, 34–49,  
441 <https://doi.org/10.1016/j.atmosres.2018.11.010>, 2019.

442 Seinfeld, J. H., Pandis, S. N., and Noone, K. J.: Atmospheric chemistry and physics:  
443 from air pollution to climate change. *Phys. Today* 51, 88–90,  
444 <https://doi.org/10.1063/1.882420>, 1998.

445 Shi, G., Xu, J., Peng, X., Xiao, Z., Chen, K., Tian, Y., Guan, X., Feng, Y., Yu, H., Nenes,  
446 A., and Russell, A. G.: pH of pH of aerosols in a polluted atmosphere: source  
447 contributions to highly acidic aerosol. *Environ. Sci. Technol.* 51, 4289–4296,  
448 <https://doi.org/10.1021/acs.est.6b05736>, 2017.

449 Shi, G., Xu, J., Peng, X., Xiao, Z., Chen, K., Tian, Y., Guan, X., Feng, Y., Yu, H., Nenes,  
450 A., and Russell, A. G.: pH of pH of aerosols in a polluted atmosphere: source  
451 contributions to highly acidic aerosol. *Environ. Sci. Technol.* 51, 4289–4296,  
452 <https://doi.org/10.1021/acs.est.6b05736>, 2017.

453 Shi, G., Xu, J., Shi, X., Liu, B., Bi, X., Xiao, Z., Chen, K., Wen, J., Dong, S., Tian, Y.,  
454 Feng, Y., Yu, H., Song, S., Zhao, Q., Gao, J., and Russell, A. G.: Aerosol pH  
455 dynamics during haze periods in an urban environment in China: use of detailed,  
456 hourly, speciated observations to study the role of ammonia availability and

457 secondary aerosol formation and urban environment. *J. Geophys. Res. Atmos.* 124,  
458 9730–9742, <https://doi.org/10.1029/2018jd029976>, 2019.

459 Song, S., Gao, M., Xu, W., Shao, J., Shi, G., Wang, S., Wang, Y., Sun, Y., and McElroy,  
460 M. B.: Fine-particle pH for Beijing winter haze as inferred from different  
461 thermodynamic equilibrium models, *Atmos. Chem. Phys.* 18, 7423–7438,  
462 <https://doi.org/10.5194/acp-18-7423-2018>, 2018.

463 Su, H., Cheng, Y. F., Cheng, P., Zhang, Y. H., Dong, S., Zeng, L. M., Wang, X., Slanina,  
464 J., Shao, M., and Wiedensohler, A.: Observation of nighttime nitrous acid (HONO)  
465 formation at a non-urban site during PRIDE-PRD2004 in China, *Atmos. Environ.*,  
466 42, 6219–6232, <https://doi.org/10.1016/j.atmosenv.2008.04.006>, 2008.

467 Takeuchi M, M. Y., Tsunoda H, Tanaka H.: Atmospheric acid gases in tokushima, Japan,  
468 monitored with parallel plate wet denuder coupled ion chromatograph. *Anal. Sci.*  
469 29, 165–168, <https://doi.org/10.2116/analsci.29.165>, 2013.

470 VandenBoer, T. C., Brown, S. S., Murphy, J. G., Keene, W. C., Young, C. J., Pszenny,  
471 A. A. P., Kim, S., Warneke, C., de Gouw, J. A., Maben, J. R., Wagner, N. L., Riedel,  
472 T. P., Thornton, J. A., Wolfe, D. E., Dubé, W. P., Öztürk, F., Brock, C. A., Grossberg,  
473 N., Lefer, B., Lerner, B., Middlebrook, A. M., and Roberts, J. M.: Understanding  
474 the role of the ground surface in HONO vertical structure: High resolution vertical  
475 profiles during NACHTT-11, *J. Geophys. Res.: Atmos.*, [https://doi.org/](https://doi.org/10.1002/jgrd.50721)  
476 [10.1002/jgrd.50721](https://doi.org/10.1002/jgrd.50721), 2013.

477 VandenBoer, T. C., Markovic, M. Z., Sanders, J. E., Ren, X., Pusede, S. E., Browne, E.  
478 C., Cohen, R. C., Zhang, L., Thomas, J., Brune, W. H., and Murphy, J. G.:  
479 Evidence for a nitrous acid (HONO) reservoir at the ground surface in Bakersfield,  
480 CA, during CalNex 2010. *J. Geophys. Res.: Atmos.* 119, 9093–9106,  
481 <https://doi.org/10.1002/2013jd020971>, 2014.

482 Veres, P., Roberts, J. M., Burling, I. R., Warneke, C., de Gouw, J., and Yokelson, R. J.:  
483 Measurements of gas-phase inorganic and organic acids from biomass fires by

484 negative-ion proton-transfer chemical-ionization mass spectrometry., *J. Geophys.*  
485 *Res.: Atmos.*, 115, D23302, <https://doi.org/10.1029/2010jd014033>, 2010.

486 Wang, G., Zhang, R., Gomez, M. E., Yang, L., Levy Zamora, M., Hu, M., Lin, Y., Peng,  
487 J., Guo, S., Meng, J., Li, J., Cheng, C., Hu, T., Ren, Y., Wang, Y., Gao, J., Cao, J.,  
488 An, Z., Zhou, W., Li, G., Wang, J., Tian, P., Marrero-Ortiz, W., Secret, J., Du, Z.,  
489 Zheng, J., Shang, D., Zeng, L., Shao, M., Wang, W., Huang, Y., Wang, Y., Zhu, Y.,  
490 Li, Y., Hu, J., Pan, B., Cai, L., Cheng, Y., Ji, Y., Zhang, F., Rosenfeld, D., Liss, P.  
491 S., Duce, R. A., Kolb, C. E., and Molina, M. J.: Persistent sulfate formation from  
492 London Fog to Chinese haze. *Proc. Natl. Acad. of Sci. U. S. A.* 113, 13630–13635,  
493 <https://doi.org/10.1073/pnas.1616540113>, 2016a.

494 Wang, H., Ding, J., Xu, J., Wen, J., Han, J., Wang, K., Shi, G., Feng, Y., Ivey, C. E.,  
495 Wang, Y., Nenes, A., Zhao, Q., and Russell, A. G.: Aerosols in an arid environment:  
496 the role of aerosol water content, particulate acidity, precursors, and relative  
497 humidity on secondary inorganic aerosols. *Sci. Total Environ.* 646, 564–572,  
498 <https://doi.org/10.1016/j.scitotenv.2018.07.321>, 2019.

499 Wang, M., Wang, S., Zhang, R., Yuan, M., Xu, Y., Shang, L., Song, X., Zhang, X., and  
500 Zhang, Y.: Exploring the HONO source during the COVID-19 pandemic in a  
501 megacity in China, *J. Environ. Sci.*, 149, 616–627,  
502 <https://doi.org/10.1016/j.jes.2023.12.021>, 2025.

503 Wang, R., Ye, X., Liu, Y., Li, H., Yang, X., Chen, J., Gao, W., and Yin, Z.:  
504 Characteristics of atmospheric ammonia and its relationship with vehicle  
505 emissions in a megacity in China, *Atmos. Environ.* 182, 97–104,  
506 <https://doi.org/10.1016/j.atmosenv.2018.03.047>, 2018.

507 Wang, S., Wang, L., Li, Y., Wang, C., Wang, W., Yin, S., and Zhang, R.: Effect of  
508 ammonia on fine-particle pH in agricultural regions of China: comparison between  
509 urban and rural sites, *Atmos. Chem. Phys.* 20, 2719–2734,  
510 <https://doi.org/10.5194/acp-20-2719-2020>, 2020.

511 Wang, W., Wang, S., Xu, J., Zhou, R., Shi, C., and Zhou, B.: Gas-phase ammonia and  
512 PM<sub>2.5</sub> ammonium in a busy traffic area of Nanjing, China, *Environ. Sci. Pollut.*  
513 *Res. Int.*, 23, 1691–1702, <https://doi.org/10.1007/s11356-015-5397-3>, 2016b.

514 Wang, X., Yin, S., Zhang, R., Yuan, M., and Ying, Q.: Assessment of summertime O<sub>3</sub>  
515 formation and the O<sub>3</sub>-NO<sub>x</sub>-VOC sensitivity in Zhengzhou, China using an  
516 observation-based model. *Sci. Total Environ.* 813, 152449,  
517 <https://doi.org/10.1016/j.scitotenv.2021.152449>, 2022.

518 Wang, Y., Zhu, S., Ma, J., Shen, J., Wang, P., Wang, P., and Zhang, H.: Enhanced  
519 atmospheric oxidation capacity and associated ozone increases during COVID-19  
520 lockdown in the Yangtze River Delta, *Sci. Total Environ.*, 768, 144796,  
521 <https://doi.org/10.1016/j.scitotenv.2020.144796>, 2021.

522 Wong, K. W., Oh, H. J., Lefer, B. L., Rappenglück, B., and Stutz, J.: Vertical profiles  
523 of nitrous acid in the nocturnal urban atmosphere of Houston, TX, *Atmos. Chem.*  
524 *Phys.*, 11, 3595–3609, <https://doi.org/10.5194/acp-11-3595-2011>, 2011.

525 Wu, S., Zhang, Y., Schwab, J., Li, Y., Liu, Y., and Yuan, C.: High-resolution ammonia  
526 emissions inventories in Fujian, China, 2009–2015, *Atmos. Environ.*, 162, 100–  
527 114, <https://doi.org/10.1016/j.atmosenv.2017.04.027>, 2017.

528 Xu, W., Kuang, Y., Zhao, C., Tao, J., Zhao, G., Bian, Y., Yang, W., Yu, Y., Shen, C.,  
529 Liang, L., Zhang, G., Lin, W., and Xu, X.: NH<sub>3</sub>-promoted hydrolysis of NO<sub>2</sub>  
530 induces explosive growth in HONO, *Atmos. Chem. Phys.* 19, 10557–10570,  
531 <https://doi.org/10.5194/acp-19-10557-2019>, 2019.

532 Xu, Z., Wang, T., Wu, J., Xue, L., Chan, J., Zha, Q., Zhou, S., Louie, P. K. K., and Luk,  
533 C. W. Y.: Nitrous acid (HONO) in a polluted subtropical atmosphere: Seasonal  
534 variability, direct vehicle emissions and heterogeneous production at ground  
535 surface, *Atmos. Environ.*, 106, 100–109,  
536 <https://doi.org/10.1016/j.atmosenv.2015.01.061>, 2015.

537 Yang, Y., Shao, M., Keßel, S., Li, Y., Lu, K., Lu, S., Williams, J., Zhang, Y., Zeng, L.,

538 Nölscher, A. C., Wu, Y., Wang, X., and Zheng, J.: How the OH reactivity affects  
539 the ozone production efficiency: case studies in Beijing and Heshan, China, *Atmos.*  
540 *Chem. Phys.*, 17, 7127–7142, <https://doi.org/10.5194/acp-17-7127-2017>, 2017.

541 Yu, Y., Cheng, P., Li, H., Yang, W., Han, B., Song, W., Hu, W., Wang, X., Yuan, B.,  
542 Shao, M., Huang, Z., Li, Z., Zheng, J., Wang, H., and Yu, X.: Budget of nitrous  
543 acid (HONO) at an urban site in the fall season of Guangzhou, China, *Atmos.*  
544 *Chem. Phys.*, 22, 8951–8971, <https://doi.org/10.5194/acp-22-8951-2022>, 2022.

545 Yun, H., Wang, Z., Zha, Q., Wang, W., Xue, L., Zhang, L., Li, Q., Cui, L., Lee, S., Poon,  
546 S. C. N., and Wang, T.: Nitrous acid in a street canyon environment: Sources and  
547 contributions to local oxidation capacity, *Atmos. Environ.*, 167, 223–234,  
548 <https://doi.org/10.1016/j.atmosenv.2017.08.018>, 2017.

549 Zellweger, M. A., P.Hofer,U.Baltensperger.: NO<sub>y</sub> speciation with a combined wet  
550 effluent diffusion denuder–aerosol collector coupled to ion chromatography,  
551 *Atmos. Environ.*, 33, 1131–1140, [https://doi.org/10.1016/s1352-2310\(98\)00295-7](https://doi.org/10.1016/s1352-2310(98)00295-7),  
552 1999.

553 Zhang, S., Sarwar, G., Xing, J., Chu, B., Xue, C., Sarav, A., Ding, D., Zheng, H., Mu,  
554 Y., Duan, F., Ma, T., and He, H.: Improving the representation of HONO chemistry  
555 in CMAQ and examining its impact on haze over China, *Atmos. Chem. Phys.*, 21,  
556 15809–15826, <https://doi.org/10.5194/acp-21-15809-2021>, 2021.

557 Zhang, W., Tong, S., Jia, C., Wang, L., Liu, B., Tang, G., Ji, D., Hu, B., Liu, Z., Li, W.,  
558 Wang, Z., Liu, Y., Wang, Y., and Ge, M.: Different HONO sources for three layers  
559 at the urban area of Beijing. *Environ. Sci. Technol.* 54, 12870–12880,  
560 <https://doi.org/10.1021/acs.est.0c02146>, 2020a.

561 Zhang, Y., Liu, X., Fang, Y., Liu, D., Tang, A., and Collett, J. L.: Atmospheric ammonia  
562 in Beijing during the COVID-19 outbreak: concentrations, sources, and  
563 implications. *Environ. Sci. Technol. Lett.* 8, 32–38,  
564 <https://doi.org/10.1021/acs.estlett.0c00756>, 2020b.



565 Zhao, Y., Zhang, N., Wei, Q., Han, Y., Mao, K., Cai, Y., and Li, R.: Flow injection  
566 chemiluminescence method in analytical chemistry., *Spectrosc. Spectra. Anal.*, 30,  
567 2512–2517., <https://doi.org/11-2200/O4WCNKI>, 2010.